SHEAR-INDUCED SELF-DIFFUSION IN CONCENTRATED SUSPENSIONS

Breedveld, V.
Shear-Induced Self-Diffusion in Concentrated Suspensions
Thesis, University of Twente, Enschede
- with references - summary in Dutch
ISBN 90-365-14991

The work described in this thesis was supported financially by the Foundation for Fundamental Research on Matter (FOM) and was part of the research program of the Twente Institute of Mechanics and the J.M. Burgers Centre for Fluid Dynamics.

Cover design: Jiska de Wit
Printed by: Universal Press, Veenendaal

SHEAR-INDUCED SELF-DIFFUSION IN CONCENTRATED SUSPENSIONS

PROEFSCHRIFT

ter verkrijging van
de graad van doctor aan de Universiteit Twente,
op gezag van de rector magnificus,
prof.dr. F.A. van Vught,
volgens besluit van het College voor Promoties
in het openbaar te verdedigen
op vrijdag 20 oktober 2000 te 15:00 uur.

door

Laurens Victor Adriaan Breedveld

geboren op 15 April 1973
te Domburg

Dit proefschrift is goedgekeurd door
de promotor

prof. dr. J. Mellema

en de assistent-promotor

dr. H.T.M. van den Ende

Contents

Chapter 1

Introduction

1.1 General background

The importance of suspensions for industrial applications has generated a long standing interest in understanding their flow behaviour, in particular transport properties. Suspensions are used for transportation of large quantities of solid particulate materials, for example sand slurries, drilling fluids in the oil industry and pulp handling in paper manufacturing. Furthermore, suspensions are of importance in manufacturing processes of many products, like ceramics, paints and food. In the past, applications rested heavily on engineering experience to predict the flow behaviour. For increasingly complex systems it is advantageous to understand the properties on a more fundamental level in order to effectively control suspension properties during the process.

Research on hard sphere suspensions has long concentrated on macroscopic rheological quantities. Viscosity, yield stresses and normal forces have been the key issues. On the particle level these quantities can be related to forces, like hydrodynamic, Brownian and interparticle forces. To find relations between these microscopic quantities and the macroscopic suspension rheology is the challenge for the rheologist.

On the particle level one can also analyze the particle motion instead of forces. For colloidal suspensions Brownian diffusion then comes to the surface as an important transport property. With the diffusion a Brownian force is associated, which can be used to calculate particle motion. These thermal effects decrease strongly with increasing particle size and for large, non-colloidal particles (roughly $> 10\ \mu$m) Brownian diffusion is negligible. It was found however (Eckstein *et al.*, 1977) that another kind of diffusion becomes more and more important for increasing particle size. The mechanism is flow-induced, i.e. after cessation of flow the diffusive process stops instantly, and has been named shear-induced or hydrodynamic diffusion.

The nature of the phenomenon is different from the more familiar concepts of

Brownian diffusion, which is caused by thermal fluctuations, and turbulent diffusion, which is driven by inertial effects and therefore only of importance at high Reynolds numbers. Shear-induced diffusion of hard spheres is the result of the spatial hindrance that particles experience in a concentrated suspension when it is macroscopically forced to flow. Its origin is depicted in figure 1.1.

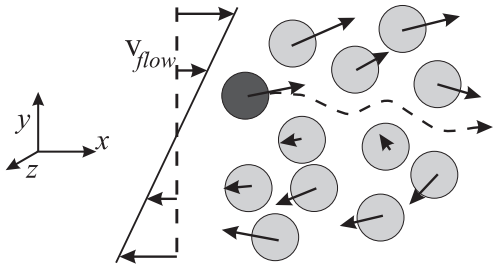

Figure 1.1: Schematic picture of a concentrated suspension under shear; the velocity profile of the macroscopic shear flow is drawn on the left.

The figure represents a concentrated suspension in simple shear flow. On the left, the macroscopic flow field is drawn. Individual particles tend to follow the flow, but on their way they encounter slower or faster particles on neighbouring streamlines with different velocities. The presence of these neighbours prevents the marked particle from moving along the original streamline. Instead, the tracer particle will exhibit a fluctuating motion when it tumbles around its neighbors. Thus also the velocities of these neighbours have a fluctuating component. When viewed on the proper timescale, the displacements of individual particles have been shown to be of diffusive nature. The diffusion is usually referred to as shear-induced self-diffusion. Note that inertial or thermal effects do not enter this picture. The presence of many neighbours in concentrated suspensions is sufficient. In principle, the velocity fluctuations should be deterministic if the particle configuration is known. As a result of the complex nature of the suspension hydrodynamics it can be described as a diffusive process.

Simple scaling arguments suffice to explain why shear-induced diffusion is only notable for non-colloidal particles. If the particle motion is diffusive, the following relation applies:

$$\langle \Delta\mathbf{x}\Delta\mathbf{x} \rangle = 2\,\mathbf{D}\,\Delta t \tag{1.1}$$

where $\Delta\mathbf{x}$ is the particle displacement vector, Δt the time step and $\mathbf{D}$ the associated diffusion tensor. A tensor is needed since the motion of particles is anisotropic due to the anisotropy of shear flow. $\mathbf{D}$ has the dimension $\left[\text{length}^2/\text{time}\right]$. The only relevant length scale in a concentrated suspension of hard spheres is the particle size (radius a). The only other length scale could be formed by the dimensions of the

flow geometry (gap width), but a fundamental transport property like shear-induced diffusion should be geometry independent. Considering the shear-induced character of the process, the relevant timescale must be $\dot{\gamma}^{-1}$. Using these scaling arguments, the diffusion tensor can be made dimensionless in the following way:

$$\mathbf{D} = \dot{\gamma}\, a^2\, \hat{\mathbf{D}} \tag{1.2}$$

where the dimensionless quantity $\hat{\mathbf{D}}$ can still depend on dimensionless parameters like the particle volume fraction ϕ. Combining the two equations shows that the dimensionless timescale of shear-induced diffusion is the strain $\dot{\gamma}\Delta t$:

$$\langle \Delta\mathbf{x}\Delta\mathbf{x} \rangle = 2\, a^2\, \hat{\mathbf{D}}\, \dot{\gamma}\Delta t \tag{1.3}$$

Shear-induced diffusion thus grows with the square of the particle size. Since Brownian diffusion decreases with particle size, two regimes can be specified: the colloidal regime where Brownian effects dominate and the non-colloidal regime where shear-induced diffusion prevails. The border between the two is not very sharp, but a particle diameter of roughly 10 μm is often used to mark the point where Brownian motion becomes insignificant.

Historically, shear-induced diffusion has been studied on two different levels: self-diffusion of individual particles and the collective process of gradient diffusion, which can lead to net migration of particles on the macroscopic level. In this thesis I concentrate on self-diffusion. By studying the results of the hydrodynamic interactions on the particle level, I have aimed for improving the understanding of the microscopic processes behind shear-induced diffusion.

1.2 Previous work

This section contains an overview of the available literature in the field. Although my thesis is focused on self-diffusion, research on gradient diffusion is included in order to construct a complete picture of current knowledge of shear-induced diffusion.

1.2.1 Experiments

Direct experimental observations of shear-induced diffusion date back to Eckstein *et al.* (1977) who studied the fluctuating motion of individual tracer particles. In concentrated suspensions the authors measured the time and radial position of a radioactive tracer particles after each full rotation in the Couette flow. This information suffices for the calculation of self-diffusion in the velocity gradient direction.

In the second half of the 1980's shear-induced diffusion received renewed attention under the impulses of Acrivos and coworkers, who observed a steady decrease of

the viscosity of concentrated suspensions during measurements in a Couette viscometer. Later, they were able to explain this effect in terms of shear-induced migration of particles from the annular Couette gap into the stagnant fluid reservoir at the bottom of the geometry, where the shear rate is considerably lower (Gadala-Maria & Acrivos, 1980; Leighton & Acrivos, 1987b). Values for the diffusion coefficient could be calculated in an indirect way by interpreting the viscosity data with a model for the viscosity as a function of particle volume fraction. In our own research group Wolthers *et al.* (1996) discovered that even for colloidal suspensions shear-induced diffusion can be of importance. In their depletion flocculated suspensions the colloidal primary particles (diameter 76 nm) formed large aggregates of non-colloidal dimensions and these aggregates exhibited the same migratory effects as non-colloidal particles during rheological experiments.

The same mechanism was also found to be responsible for particles fluxes against gravity in sedimented layers, referred to as viscous resuspension. Since visual observation of resuspension is relatively simple, experiments have been performed in different flow geometries: Couette (Leighton & Acrivos, 1986; Acrivos *et al.*, 1993), parallel plate (Chapman & Leighton, 1991) and plane channel flow (Schaflinger *et al.*, 1990, 1995). The main disadvantage of the experimental technique is that the motion of diffusing particles can not be measured, only macroscopic concentration profiles are detected. Again, viscosity model must be used to relate resuspension heights to diffusion coefficients. An elegant addition to resuspension experiments was carried out by Tripathi & Acrivos (1999), who showed that in a mixture of neutrally buoyant and heavy particles, the latter exhibit enhanced resuspension due to the presence of the neutrally buoyant particles that increased the frequency of interactions.

Another approach has been to directly measure concentration profiles by means of NMR. This non-invasive technique enables direct monitoring of the evolution of particle distributions. For large particles (600 μm) even individual particles can be located. The technique was developed by Abbott *et al.* (1991) (see also Graham *et al.*, 1991) and originally applied to wide-gap Couette flow. Later on the method has also been used to study parallel-plate (Chow *et al.*, 1994) and pipe flow (Hampton *et al.*, 1997). Although the technique has provided interesting images of the particle distribution and thus revealed many intriguing phenomena, the microscopic processes behind the diffusive process could not be investigated due to the low frequency of image acquisition, typically 10 minutes per NMR image.

To obtain information about the microscopic mechanism of shear-induced diffusion it is preferable to directly measure the motion of individual particles. Then information about *self-diffusion* is generated, which must be strongly related to the collective *gradient diffusion* as determined in the experiments described above. The technique of the already mentioned self-diffusion measurements of Eckstein *et al.* (1977) was improved successively by Leighton & Acrivos (1987a) and Phan & Leighton

(1993), who visually observed opaque tracers in a transparent suspension of density and refractive index matched particles and fluid. The most recent measurements included results for diffusion in the vorticity direction by monitoring the axial position. The experimental technique has proven extremely valuable for understanding the scaling behaviour of shear-induced diffusion. The main limitation is that the timescale of the observations is governed by the Couette flow and can not be controlled externally for any given piece of equipment. The passage time of the tracer particle depends on its radial position: near the stationary outer cylinder particles have a lower velocity than near the rotating inner cylinder. As a result, the experiments were all performed for relatively large strain values ($\dot{\gamma}\Delta t \sim O(10)$, as explained in section 1.1 this is the relevant timescale). In order to collect detailed information about the nature of microscopic interaction it would be highly desirable to be able to monitor particles over a wide range of strain values $\dot{\gamma}\Delta t$. This thesis addresses the problem by developing a novel technique, which includes the flexibility of timescales.

For sedimentation of non-colloidal suspensions interesting experimental work has been done by Nicolai and co-workers (Nicolai *et al.*, 1995; Nicolai & Guazelli, 1995). They visualized the paths of individual tracer particles in transparent suspensions by means of a CCD camera. The particle paths were then used to extract information about the average sedimentation velocity and about velocity fluctuations, which are the result of hydrodynamic interactions. The diffusion coefficients from these experiments differ from the other self-diffusion experiments, because of the nature of the flow. First of all, the in sedimentation the shear rate is ill-defined. Secondly, for increasing volume fractions self-diffusion under sedimentation strongly decreases, because particles are trapped by their neighbours. In steady shear experiments, on the other hand, the macroscopic flow forces relative motion of particles and the scaling at high volume fractions is less obvious, as will be shown in the rest of this thesis (e.g. figure 2.1).

1.2.2 Theory

Theoretical work on shear-induced migration has been strongly focused on gradient diffusion. One of the reasons is that most experimental studies have been directed at measuring this quantity as well, as was shown in section 1.2.1, so that data is available for comparison. Although our own work is concentrated on self-diffusion, an overview of migration theories is presented first, to show the current state of theory. In the remainder of the section the theoretical work on self-diffusion will be addressed.

In order to interpret their experimental results Leighton & Acrivos (1987b) tried to gain physical insight into the mechanisms that cause shear-induced diffusion. Their analysis concentrates on gradient diffusion which was observed to induce changes in

viscosity during steady shear measurements in a Couette rheometer. The model they proposed is based on a mechanistic picture: irreversible particle interactions in concentrated suspensions give rise to displacements both in the vorticity direction –i.e. normal to the plane of shear– and in the velocity gradient direction. Simple considerations about the nature of such interactions, e.g. frequency and size of displacements, lead to correct scaling predictions of the evolution of particle distributions in inhomogeneous shear flow, like Couette and channel flow. An additional term of diffusion is introduced in relation to variations in suspension viscosity with volume fraction. The idea is that during a "collision" the particle displacements will be largest towards the regions with lowest suspension viscosity. Qualitatively the model of Leighton & Acrivos (1987b) predicts net particle migration towards regions of low shear rate, because such an inhomogeneous particle distribution balances the migratory fluxes.

These concepts were worked out by Phillips *et al.* (1992) who captured the ideas in an evolution equation for the particle concentration ϕ, based on balancing the various diffusive fluxes. The model, often referred to as "diffusive flux model", was solved numerically and the free model parameters were determined by comparing the calculations with particle distributions that were determined experimentally by means of NMR (Abbott *et al.*, 1991). Good agreement was found between model predictions and experiments both for transient and steady state flow in wide gap Couette and Poiseuille flow.

The main shortcoming of the diffusive flux model is that for regions where the shear rate $\dot{\gamma} = 0$ the particle concentration at the center will by definition increase to the maximum packing limit. In Poiseuille flow this leads to a predicted cusp in particle concentration at the center line, since $\dot{\gamma} = 0$ at this position. However, real particles with finite size will in general be so large that they experience a locally averaged shear rate $\dot{\gamma}_{ave} \neq 0$. Averaging over distances comparable to the particle diameter could provide a physical solution for this model artefact. In pipe flow experiments of Hampton *et al.* (1997) it was indeed found that the quality of the model predictions at the center of the pipe strongly depends on the ratio of particle to pipe radius, a/R. For small a/R the continuum model of Phillips *et al.* (1992) provides more accurate predictions than for large values of a/R, when the particle size is significant compared to the dimensions of the flow geometry and averaging of the shear rate over at least the particle dimensions seems appropriate.

In other geometries the diffusive flux model also fails to accurately predict experimental findings, in particular for cone-plate and parallel plate torsional flow. According to the model particles will always migrate towards regions of lowest shear rate. Consequently, the steady state solution for the particle concentration is homogeneous in cone-plate geometry (constant $\dot{\gamma}$) and inhomogeneous for parallel plate flow, with migration towards the axis of rotation. However, experimental results suggest that in plate-plate geometry hardly any migration is observed, while slight outward

migration is found in truncated cone-plate flow (Chapman, 1990; Chow *et al.*, 1994). To resolve the discrepancy, Krishnan *et al.* (1996) have suggested modifications of the diffusive flux model by including curvature effects. The idea behind the adaptations is that two "colliding" particles will experience a joint outward displacement due to curvature of the velocity field.

A different approach to the problem was initiated by Nott & Brady (1994) with the so-called "suspension balance model", which was recently extended by Morris & Boulay (1999). The essential feature in their work is that migration is related to rheological properties of the suspension, including normal stresses and anisotropy which are neglected in the mechanistic diffusive flux model. Especially in curvilinear flows, like cone-plate and parallel plate, normal stress differences come into play. It is demonstrated that all experimental results listed above for various flow geometries can be described successfully –at least qualitatively– with a single set of parameters. For quantitative predictions, accurate rheological data is needed, which is non-trivial for non-colloidal suspensions since normal stress differences are small and difficult to measure. An extensive experimental study of Zarraga *et al.* (2000) has shown very recently that the predictions of Morris & Boulay (1999) are in good agreement with rheological data for suspensions of non-colloidal spherical particles.

The studies mentioned above all address the problem of gradient diffusion. Theoretical work on self-diffusion in the concentrated regime is scarce. For dilute suspension where the interactions between particles essentially only involve two (or three) particles, several researchers have studied the nature of hydrodynamic interactions. In infinite Stokes flow a two-particle collision is symmetrical and no displacements are observed after the interaction is completed. Asymmetry can be introduced in various ways: Da Cunha & Hinch (1996) have used the idea of particle roughness to force particles to stay separated at a certain minimum distance during the interaction, Wang *et al.* (1996) calculate the influence of a third particle as symmetry breaker and Pesche (1998) investigated the effect of a short-range repulsive force. All studies have shown that breaking the symmetry leads to displacements in the velocity gradient and vorticity direction, thus explaining the presence of $\hat{D}_{yy}$ and $\hat{D}_{zz}$. However, the anisotropy $\hat{D}_{yy}/\hat{D}_{zz}$ in these dilute calculations is far larger ($O(10)$) than in experiments (ca. 2). Apparently additional mechanisms come into play for concentrated suspensions.

Brady & Morris (1997) have tried to extrapolate a scaling theory, which is valid for dilute systems, to describe shear-induced self-diffusion the concentrated regime. Although the theory predicts the correct level of anisotropy, it fails in describing the dependency of diffusion on volume fraction. The theory predicts a monotonous growth, while experiments (Phan & Leighton, 1993) have shown that at high concentrations diffusion levels off. In spite of this discrepancy, until now the work of Brady & Morris (1997) is the most promising theoretical attempt to explain self-diffusion.

More detailed studies are needed, but the efforts would be greatly supported by collecting more reliable experimental information to create an unambiguous picture of the dependencies of self-diffusion on important physical quantities like volume fraction.

1.2.3 Numerical work

In recent years computer techniques have improved to the level where computations on complicated systems are within reach. Although various research groups have worked in the field, numerical work on concentrated suspensions is strongly associated with the Stokesian Dynamics technique that was developed by Brady and coworkers (e.g. Bossis & Brady, 1987; Phung *et al.*, 1996). Originally, the computations were focused on colloidal systems, where Brownian diffusion plays an important role. Only recently, the numerical work has extended to the non-colloidal regime, where shear-induced diffusion becomes important. Non-colloidal calculations require shorter time steps and therefore computational costs are high and the system size is limited. For most published work (Yurkovetsky, 1998; Foss & Brady, 1999; Marchioro & Acrivos, 2000) systems of only 27 particles were used with periodic boundary conditions. Since the system size is small compared to any realistic system, the results have to be treated with caution when comparing them to experimental data. Moreover, the computations deal with perfectly smooth spheres, whereas experimental systems will always have finite roughness and non-sphericity.

In spite of these marginal notes, Stokesian Dynamics computations provide coefficients of self-diffusion that are slightly smaller than experimental results, but of the same order of magnitude. Anisotropy is also comparable with $\hat{D}_{yy}/\hat{D}_{zz} \sim 2$. The main discrepancy is the shape of the diffusion curve, when plotted against volume fraction ϕ. Like the theoretical work of Brady & Morris (1997), numerical results exhibit a monotonous growth. Recent work suggests the existence of plateau values at high volume fractions for $\hat{D}_{yy}$ (Foss & Brady, 1999; Marchioro & Acrivos, 2000), but both studies distinctly show that $\hat{D}_{zz}$ increases with ϕ. All in all, numerical work has made significant progress in studying shear-induced diffusion in concentrated suspensions, but the current discrepancies with experiments must be addressed.

1.3 Thesis outline

From the overview in the preceding sections it becomes clear that many fundamental questions about shear-induced diffusion remain unanswered. In this thesis new experimental work on self-diffusion will be presented with the aim to increase the understanding of the underlying processes. Thus I hope to contribute to the development of a framework of well-defined experimental results, which can provide the fundament

for understanding the microscopic processes that give rise to shear-induced diffusion. The backbone of my work is formed by a novel technique that has been developed to collect more detailed information on the particle motion.

The thesis is organized as follows. The principles of the measuring technique are described in chapter 2, which also deals with the experimental realization and the first results for the diffusion coefficients in the velocity gradient ($\hat{D}_{yy}$) and vorticity direction ($\hat{D}_{zz}$), obtained in a Couette geometry. The technique is based on visual analysis of the motion of a large ensemble of coloured tracer particles in an otherwise refractive index matched suspension. The main advantage over other methods is that the particle motion can be monitored over a wide range of well-controlled strain values. It it also shown that the method is applicable for determining fluid diffusivity by introducing tiny tracer particles into a suspension of much larger particles.

The experiments of chapter 2 were not carried out under ideal conditions. The accessible range of timescales was limited by the geometry with a rotating inner and stagnant outer cylinder, because the tracer particles are shifted out of the observation window. For comparison with literature data it is preferable to increase the range of parameters. Therefore a new set-up has been designed with a counter-rotating flow geometry. Experiments in the sophisticated geometry are reported in chapter 3.

In chapter 4 the results of the diffusion measurements are placed in a broader perspective by comparing the results with particle trajectories, which were determined by means of particle tracking, and rheological measurements. The combined experiments reveal a complete and coherent picture of the relevant timescales and microstructure in concentrated suspensions under shear.

The experimental technique was developed further to extract the full diffusion tensor, including the diffusivity in the velocity direction, $\hat{D}_{xx}$, and the off-diagonal term, $\hat{D}_{xy}$. These diffusion coefficients have never been determined experimentally before, only limited numerical results are available. The advanced data analysis is described in detail in chapter 5.

The final chapter is devoted to some theoretical considerations. In an attempt to gain physical insight a simple collision model has been developed, that captures a number of the most important experimental characteristics of shear-induced self-diffusion.

Finally, it should be noted that most chapters are self-contained and have been (or will be) published as papers in scientific journals. Only minor changes –mostly typographic– have been made to turn the thesis into a coherent structure.

References

ABBOTT, J.R. , TETLOW, N. , GRAHAM, A.L. , ALTOBELLI, S.A. , FUKUSHIMA, E. , MONDY, L.A. & STEPHENS, T.S. 1991 Experimental observations of parti-

cle migration in concentrated suspensions: Couette flow. *J. Rheol.* **35** (5), 773–795.

ACRIVOS, A. , MAURI, R. & FAN, X. 1993 Shear-induced resuspension in a Couette device. *Int. J. Multiphase Flow* **19** (5), 797–802.

BOSSIS, G. & BRADY, J.F. 1987 Self-diffusion of Brownian particles in concentrated suspensions under shear. *J. Chem. Phys.* **87**, 5437–5448.

BRADY, J.F. & MORRIS, J.F. 1997 Microstructure of strongly sheared suspensions and its impact on rheology and diffusion. *J. Fluid Mech.* **348**, 103–139.

CHAPMAN, B.K. 1990 Shear induced migration in concentrated suspensions. PhD thesis, University of Notre Dame.

CHAPMAN, B.K. & LEIGHTON, D.T. 1991 Dynamic viscous resuspension. *Int. J. Multiphase Flow* **17** (4), 469–483.

CHOW, A.W. , SINTON, S.W. , IWAMIYA, J.H. & STEPHENS, T.S. 1994 Shear-induced particle migration in Couette and parallel-plate viscometers: NMR imaging and stress-measurements. *Phys. Fluids* **6** (8), 2561–2576.

DA CUNHA, F.R. & HINCH, E.J. 1996 Shear-induced dispersion in a dilute suspension of rough spheres. *J. Fluid Mech.* **309**, 211–223.

ECKSTEIN, E.C. , BAILEY, D.G. & SHAPIRO, A.H. 1977 Self-diffusion of particles in shear flow of a suspension. *J. Fluid Mech.* **79**, 191–208.

FOSS, D.R. & BRADY, J.F. 1999 Self-diffusion in sheared suspensions by dynamic simulation. *J. Fluid Mech.* **401**, 243–274.

GADALA-MARIA, F. & ACRIVOS, A. 1980 Shear-induced structure in a concentrated suspension of solid spheres. *J. Rheol.* **24** (6), 799–814.

GRAHAM, A.L. , ALTOBELLI, S.A. , FUKUSHIMA, EIICHI , MONDY, L.A. & STEPHENS, T.S. 1991 Note: NMR imaging of shear-induced diffusion and structure in concentrated suspensions undergoing Couette flow. *J. Rheol.* **35** (1), 191–201.

HAMPTON, R.E. , MAMMOLI, A.A. , GRAHAM, A.L. , TETLOW, N. & ALTOBELLI, S.A. 1997 Migration of particles undergoing pressure driven flow in a circular conduit. *J. Rheol.* **41** (3), 621–640.

KRISHNAN, G.P. , BEIMFOHR, S. & LEIGHTON, D.T. 1996 Shear-induced radial segregation in bidisperse suspensions. *J. Fluid Mech.* **321**, 371–393.

LEIGHTON, D. & ACRIVOS, A. 1986 Viscous resuspension. *Chem. Engng Sci.* **41** (6), 1377–1384.

LEIGHTON, D. & ACRIVOS, A. 1987a Measurement of shear-induced self-diffusion in concentrated suspensions of spheres. *J. Fluid Mech.* **177**, 109–131.

LEIGHTON, D. & ACRIVOS, A. 1987b The shear-induced migration of particles in concentrated suspensions. *J. Fluid Mech.* **181**, 415–439.

MARCHIORO, M. & ACRIVOS, A. 2000 Shear-induced particle diffusivities from numerical simulations. *J. Fluid Mech.* **submitted**.

MORRIS, J.F. & BOULAY, F. 1999 Curvilinear flows of noncolloidal suspensions: the role of normal stresses. *J. Rheol.* **43** (5), 1213–1237.

NICOLAI, H. & GUAZELLI, E. 1995 Effect of the vessel size on the hydrodynamic diffusion of sedimenting spheres. *Phys. Fluids* **7** (1), 3–5.

NICOLAI, H. , HERZHAFT, B. , HINCH, E.J. , OGER, L. & GUAZELLI, E. 1995 Particle velocity fluctuations and hydrodynamic self-diffusion of sedimenting non-Brownian spheres. *Phys. Fluids* **7** (1), 12–23.

NOTT, P.R. & BRADY, J.F. 1994 Pressure-driven flow of suspensions: simulation and theory. *J. Fluid Mech.* **275**, 157–199.

PESCHE, R. 1998 Etude par simulation numerique de la segregation de particules dans une suspension bidisperse. PhD thesis, Universite de Nice-Sophia Antipolis, France.

PHAN, S.E. & LEIGHTON, D.T. 1993 Measurement of the shear-induced tracer diffusivity in concentrated suspensions. *J. Fluid Mech.* **submitted**.

PHILLIPS, R.J. , ARMSTRONG, R.C. & BROWN, R.A. 1992 A constitutive equation for concentrated suspensions that accounts for shear-induced particle migration. *Phys. Fluids* **4** (1), 30–40.

PHUNG, T.N. , BRADY, J.F. & BOSSIS, G. 1996 Stokesian Dynamics simulation of Brownian suspensions. *J. Fluid Mech.* **313**, 181–207.

SCHAFLINGER, U. , ACRIVOS, A. & STIBI, H. 1995 An experimental study of viscous resuspension in a pressure-driven plane channel flow. *Int. J. Multiphase Flow* **21** (4), 693–704.

SCHAFLINGER, U. , ACRIVOS, A. & ZHANG, K. 1990 Viscous resuspension of a sediment within a laminar and stratified flow. *Int. J. Multiphase Flow* **16** (4), 567–578.

TRIPATHI, A. & ACRIVOS, A. 1999 Viscous resuspension in a bidensity suspension. *Int. J. Multiphase Flow* **25** (1), 1–14.

WANG, Y. , MAURI, R. & ACRIVOS, A. 1996 The transverse shear-induced liquid and particle tracer diffusivities of a dilute suspension of spheres undergoing a simple shear flow. *J. Fluid Mech.* **327**, 255–272.

WOLTHERS, W. , VAN DEN ENDE, D. , DUITS, M.H.G. & MELLEMA, J. 1996 The viscosity and sedimentation of aggregating colloidal dispersions in a Couette flow. *J. Rheol.* **40** (1), 55–67.

YURKOVETSKY, Y. 1998 I. Statistical mechanics of bubbly liquids; II. Behavior of sheared suspensions of non-Brownian particles. PhD thesis, Californian Institute of Technology.

ZARRAGA, I.E. , HILL, D.A. & LEIGHTON, D.T. 2000 The characterisation of the total stress of concentrated suspensions of noncolloidal spheres in Newtonian fluids. *J. Rheol.* **44** (2), 185–220.

Chapter 2

Novel Technique for Measuring Shear-Induced Tracer-Diffusion in Concentrated Suspensions *

Abstract

The shear-induced particle self-diffusivity in a concentrated suspension (20% - 50% solids volume fraction) of non-colloidal spheres (90 μm average diameter) was measured using a new correlation technique. This method is based on the correlation between the positions of tracer particles in successive images and can be used to determine the self-diffusivity in non-colloidal suspensions for different timescales. These self-diffusivities were measured in the velocity gradient and vorticity directions in a narrow gap Couette device for values of the strain $\dot{\gamma}\Delta t$ ranging from 0.05 to 0.5, where $\dot{\gamma}$ is the applied shear rate and Δt is the correlation time. In both directions, the diffusive displacements scaled linearly with $\dot{\gamma}\Delta t$ over the range given above and the corresponding diffusivities were found to be in good agreement with the experimental results of Leighton & Acrivos (1987a) and of Phan & Leighton (1993), even though these earlier studies were performed at much larger values of $\dot{\gamma}\Delta t$. The self-diffusivity in the velocity gradient direction was found to be about 1.7 times larger than in the vorticity direction. The technique was also used to determine the shear-induced fluid tracer diffusivity by measuring the mean square displacement of 31.5 μm diameter tracer particles dispersed in concentrated suspensions (30% - 50% solids volume fraction) of non-colloidal spheres (325 μm average diameter). These fluid diffusivities were found to be 0.7 times the corresponding particle diffusivities when both were scaled with $\dot{\gamma}a^2$ ($2a = 325\,\mu$m).

*This chapter was published as *'The Measurement of the Shear Induced Particle and Fluid Tracer-Diffusivities in Concentrated Suspensions by a Novel Method*, V. Breedveld, D. van den Ende, A. Tripathi, A. Acrivos, J. Fluid Mech. **375**, pp. 297-318 (1998)'

2.1 Introduction

The self-diffusion of tracer particles in non-colloidal, as well as non-Brownian, suspensions has attracted a great deal of attention in recent years. Even at low Reynolds numbers, where inertial effects play a negligible role, particles in such suspensions exhibit diffusion-like motions due to hydrodynamic interactions with their neighbours whose positions have a random component. These interparticle interactions induce a net particle migration in the presence of inhomogeneities in the bulk shear rate or in the particle concentration.

In order to understand this type of self-diffusivity, consider a neutrally buoyant test sphere in a viscous suspension of otherwise identical spheres. When the suspension is subjected to an external shear flow, the test particle interacts with the other particles surrounding it and, consequently, experiences a series of displacements away from its original streamline. Such displacements, when taken together, will have zero mean but a finite mean square displacement which can be characterized by a shear-induced coefficient of self-diffusion. Since the rate of such interactions is proportional to the shear rate $\dot{\gamma}$, and the length scale of each displacement is comparable to the particle radius a, the diffusion coefficient has a dimensional scaling $\dot{\gamma}a^2$ (Eckstein *et al.*, 1977). It is important to note that the coefficient of self-diffusion associated with this mechanism is quite different from the shear-induced gradient diffusivity (Leighton & Acrivos, 1987b), the latter being the coefficient in the linear relation between the particle flux resulting a non-uniformity in the particle concentration and the concentration gradient. According to the arguments by Leighton & Acrivos (1987b), such a flux down a concentration gradient arises because a given particle in a sheared suspension experiences a greater number of interactions from the high concentration side than from the other. On the other hand, the mixing of marked spheres in a suspension of uniform concentration is entirely a self-diffusion process.

Although the latter is one of the most basic transport processes occurring in sheared suspensions, only a few theoretical and experimental studies of the self-diffusivity have been reported to-date. These include the experimental measurements of the shear-induced self-diffusivity of non-Brownian particles by Eckstein *et al.* (1977), Leighton & Acrivos (1987a) and Phan & Leighton (1993), the computations via Stokesian Dynamics simulations by Bossis & Brady (1987), Phung *et al.* (1996), Phung (1993) and the theoretical work by Brady & Morris (1997). The results of all these studies are summarized in figure 2.1 (Brady, 1997) where the dimensionless self-diffusivities along the velocity gradient and vorticity directions are plotted as a function of the particle concentration ϕ. Clearly, owing to the large scatter in the experimental observations it is difficult to compare directly the experimental and computational results. In addition, in order to understand the nature of the microscopic interactions between the particles, measurements of the self-diffusivity over

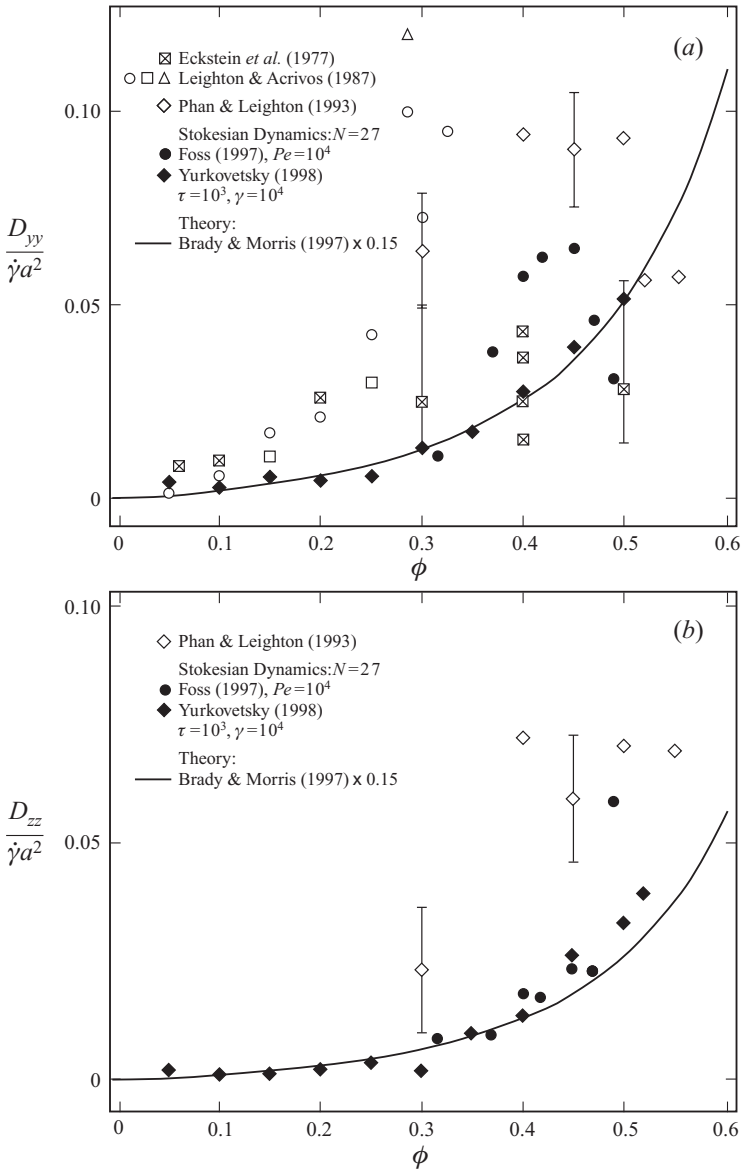

Figure 2.1: Data for the shear-induced self-diffusivity in a simple shear flow collected by Brady (1997) and plotted against the particle volume fraction in the suspension. *(a)* The self-diffusivity along the direction of shear; *(b)* the self-diffusivity along the vorticity axis. (Adapted with the permission of Professor J.F. Brady)

a wide range of values of the strain $\dot{\gamma}\Delta t$, where Δt is the time step over which the particle displacement is observed, would be highly desirable. To our knowledge such measurements have not been attempted thus far.

Similarly, the self-diffusivity of a fluid tracer in non-colloidal concentrated suspensions has not been measured thus far in spite of its importance in many industrial and clinical processes. For example, a great deal of literature is available concerning liquid phase mass transport in red blood cell suspensions and on the gas and heat transport in suspensions of particles. Zidney & Colton (1988) list about 50 publications on this topic. Although considerable evidence exists that both heat and mass transport in concentrated suspensions can be substantially augmented in shear flow, existing models are not completely adequate for predicting the experimental observations. We believe that the results of this study can be used to estimate the importance of augmented solute transport in the flow of concentrated suspensions, and also that they can provide a basis for a more detailed experimental and theoretical study of this phenomenon.

In this chapter we present a new method for measuring the self-diffusion coefficient in concentrated suspensions of non-colloidal and non-Brownian particles. This technique is based on the application of spatial correlation procedures to consecutive images of tracer particles in a fixed imaging volume. In the next section, the general idea of the method will be explained, followed by the development of a theoretical framework for analyzing the data. Then, in subsection 2.2.3 the theory will be applied to the case of a simple shear flow, applicable to the Couette geometry in which we performed our experiments. The third section contains a description of our experimental procedure and the final section is devoted to the results and discussion.

2.2 The new approach

In this section we shall present the salient features of a simple and accurate experimental technique for measuring the self-diffusion coefficient in concentrated sheared suspensions.

2.2.1 Basic concepts

We examine the phenomenon of diffusion by investigating the positions of tracer neutrally buoyant spherical particles immersed in a suspension of otherwise identical spheres undergoing shear. The tracers are colored black in order to distinguish them from the surrounding particles, which are refractive index matched with the suspending fluid. The images are taken at a fixed position in the geometry, but, because the suspension is being sheared, the tracers move with the general flow and will stay in the image window only for a limited time. Figure 2.2 shows an example

of two successive images taken at a time interval Δt with the bulk flow as indicated so that all the particles move from left to right. The imaging window occupies a two-dimensional rectangular area. In an experimental set-up, the window will always be the two-dimensional projection of a three-dimensional fluid volume, because of the finite depth of focus of the optics (This effect will be dealt with in the next subsection and does not change the general considerations to be described below). The black particles in figure 2.2 represent the tracers, while the white ones refer to the refractive index matched particles, which are invisible if the matching is perfect. Particles intersecting the border of the image window are not drawn.

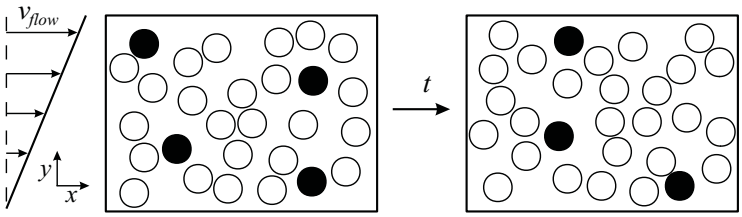

Figure 2.2: Schematic diagrams of two successive images of a fluid element in a sheared suspension.

The motion of the non-colloidal particles consists of two parts: a convective motion along the streamlines of the bulk fluid flow and fluctuations due to their hydrodynamic interactions with other particles. The latter give rise to the shear-induced diffusion, both the self-diffusion and, if present, the gradient diffusion. An essential step in the technique consists of locating all the M tracers in the second image as well as all the N tracers in the first image and then calculating the two-dimensional vectors:

$$\Delta\tilde{\mathbf{x}}_{nm} = (x_m - x_n, y_m - y_n) \qquad n = 1,2,..,N; m = 1,2,..,M$$

where $(x_n y_n)$ and (x_m, y_m) refer to the positions of the particle centers in the first and second image, respectively. This results into $N \cdot M$ different two-dimensional displacement vectors $\Delta\tilde{\mathbf{x}}_{nm}$, generally a number too small for performing a meaningful statistical analysis. Figure 2.2, for example, yields 12 vectors. But if the procedure is repeated for a large number of image combinations with the same time-interval, the number of vectors increases rapidly. These data can be used to define the function $C_{2D}(\Delta\tilde{\mathbf{x}};\Delta t)$, which denotes the number of times a two-dimensional displacement vector $\Delta\tilde{\mathbf{x}}$ appears in the ensemble of images. The function $C_{2D}(\Delta\tilde{\mathbf{x}};\Delta t)$ thus represents the experimental probability density of finding a vector $\Delta\tilde{\mathbf{x}}$ in the ensemble of images.

The vectors $\Delta\tilde{\mathbf{x}}_{nm}$ can be divided into two different categories. The first contains all the vectors $\Delta\tilde{\mathbf{x}}_{nm}^{auto}$ for which tracer m is the same as n. On these occasions, the

particle has not left the image window during the time interval. The second category contains all the cross-correlation vectors $\Delta\tilde{\mathbf{x}}_{nm}^{cross}$, between different tracer particles in consecutive images. For example, assume that N' $(N' \leq N)$ particles in the first image of figure 2.2 are present in the second image as well. Then, the total number of $N \cdot M$ correlation vectors $\Delta\tilde{\mathbf{x}}_{nm}$ consists of N' auto-correlation vectors $\Delta\tilde{\mathbf{x}}_{nm}^{auto}$ and $N \cdot M - N'$ cross-correlation vectors $\Delta\tilde{\mathbf{x}}_{nm}^{cross}$. For the analysis of the particle motion, the auto-correlation vectors $\Delta\tilde{\mathbf{x}}_{nm}^{auto}$ are of interest because they contain information about the displacements of individual particles during the time interval Δt. The cross-correlation vectors are of less interest, although they contain information on the spatial distribution of the tracer particles in the fluid.

Unfortunately, it is impossible to tell a priori whether a vector $\Delta\tilde{\mathbf{x}}_{nm}$ belongs to the first or to the second category. This would only be possible if the time interval was very small, so that one could easily detect where the individual particles have gone. In the general case of larger time intervals, however, this would be very difficult and thus complicate the interpretation of the images. Fortunately, our technique does not need this information in evaluating the self-diffusivity. Specifically, we shall show in the next section that the auto-correlation and cross-correlation contributions to $C_{2D}(\Delta\tilde{\mathbf{x}};\Delta t)$ are of a different nature, and therefore can be separated statistically. Then, once the auto-correlation part has been extracted from the correlation vectors, the diffusive motion of individual particles can be analyzed. Before proceeding though, let us first generalize the concept to the full three-dimensional formulation.

2.2.2 Theoretical formulation in three-dimensions

In the experimental system, the two-dimensional images are the projection of a three-dimensional fluid volume. The effects of this projection onto a finite-sized two-dimensional image window have not been taken into account so far and will be analyzed in this section. As will be shown, this slightly complicates the interpretation of the experimentally determined function $C_{2D}(\Delta\tilde{\mathbf{x}};\Delta t)$ mentioned in the previous section, but, after carefully considering these effects, $C_{2D}(\Delta\tilde{\mathbf{x}};\Delta t)$ can be directly related to the actual three-dimensional probability density of the particles which is the quantity of primary interest. No a priori assumptions on the nature of the particle motion have to be made.

The effect of the projection is that the three-dimensional displacement vectors $\Delta\mathbf{x} \equiv (\Delta x, \Delta y, \Delta z)$ in the fluid volume become two-dimensional vectors on the image, $\Delta\tilde{\mathbf{x}} \equiv (\Delta x, \Delta y)$. Thus, determining the correlation function $C_{2D}(\Delta x, \Delta y; \Delta t)$ we are, in essence, counting the number of two-dimensional vectors $(\Delta x, \Delta y)$ appearing in the images by adding all the three-dimensional vectors $(\Delta x, \Delta y, \Delta z)$, regardless of the value of the out of plane distance Δz. This can be formulated mathematically as

$$C_{2D}(\Delta x, \Delta y; \Delta t) = \int C_{3D}(\Delta x, \Delta y, \Delta z; \Delta t) d\Delta z \tag{2.1}$$

where $C_{3D}(\Delta x, \Delta y, \Delta z; \Delta t)$ is the three-dimensional spatial correlation probability of the image ensemble, representing the chance of finding a displacement $(\Delta x, \Delta y, \Delta z)$. Off hand, it might appear that $C_{3D}(\Delta x, \Delta y, \Delta z; \Delta t)$ should equal $P(\Delta \mathbf{x}; \Delta t)$, where $P(\Delta \mathbf{x}; \Delta t)$ is defined as the theoretical probability density of finding two particles with center to center vector $\Delta \mathbf{x}$ after a given time interval Δt. However, owing to experimental limitations, the two functions are related by

$$C_{3D}(\Delta \mathbf{x}; \Delta t) = \iiint_V S(\mathbf{x}, \mathbf{x}+\Delta \mathbf{x}) P(\Delta \mathbf{x}; \Delta t) dV \tag{2.2}$$

where $S(\mathbf{x}, \mathbf{x}+\Delta \mathbf{x})$ to be discussed further on in this section, is the experimental probability of detecting the particles referred to above.

The function $C_{3D}(\Delta x, \Delta y, \Delta z; \Delta t)$ thus represents the ensemble averaged experimental sampling of the probability density $P(\Delta \mathbf{x}; \Delta t)$ and will be analyzed in terms of $P(\Delta \mathbf{x}; \Delta t)$. Next, following the same arguments as in section 2.2.1, we split the probability density function $P(\Delta \mathbf{x}; \Delta t)$ into two parts. The first, termed the spatial auto-correlation in section 2.2.1, refers to the probability that the same particle has been displaced by $\Delta \mathbf{x}$. In terms of the probability distribution, it is equivalent to the transition probability density $P^{trans}(\Delta \mathbf{x}; \Delta t, \mathbf{x})$ of a particle being displaced by $\Delta \mathbf{x}$ during the time Δt, starting from position $\mathbf{x}$. The function $P^{trans}(\Delta \mathbf{x}; \Delta t, \mathbf{x})$ contains fundamental information on the particle motions.

The second contribution to the total probability density $P(\Delta \mathbf{x}; \Delta t)$ refers to the probability density of finding two different tracer particles at relative positions $\Delta \mathbf{x}$ after the time-interval Δt. This part of the distribution probability density will be denoted by $P^{distr}(\Delta \mathbf{x}; \Delta t)$, since it is linked to the distribution of different tracer particles over the image window. $P^{distr}(\Delta \mathbf{x}; \Delta t)$ can then be expressed as:

$$P^{distr}(\Delta \mathbf{x}; \Delta t) = \iiint P_1(\mathbf{x}; t) P_2(\mathbf{x}+\Delta \mathbf{x}; t+\Delta t) d\mathbf{x} \tag{2.3}$$

where $P_1(\mathbf{x}; t)$ is the probability density of finding a tracer at $\mathbf{x}$ and $P_2(\mathbf{x}+\Delta \mathbf{x}; t+\Delta t)$ is the conditional probability density of another tracer being on the position $\mathbf{x}+\Delta \mathbf{x}$ after a time-interval Δt given that the first tracer was at $\mathbf{x}$. Also, the domain of integration is the whole image volume. Of course, if the tracers are distributed homogeneously over the window, P_1 is constant and can be taken out of the integration. Having thus defined the probability density functions $P^{trans}(\Delta \mathbf{x}; \Delta t, \mathbf{x})$ and $P^{distr}(\Delta \mathbf{x}; \Delta t)$, we proceed with the derivation of their relations with the spatial correlation function $C_{3D}(\Delta \mathbf{x}; \Delta t)$ (equation (2.2)), which in turn can be used to determine $C_{2D}(\Delta \tilde{\mathbf{x}}; \Delta t)$ via equation (2.1). The main effect to consider is the fact that the observed fluid volume is of limited size in all three directions and that the image analysis introduces some errors in detecting the particles in the images. Both factors influence the sampling function $C_{3D}(\Delta \mathbf{x}; \Delta t)$.

First, let us investigate the effect of the window boundaries in the x- and y-direction. Note that if the image window has width W and height H, the two-dimensional displacement vector $\Delta\tilde{\mathbf{x}}$ can never exceed the limits

$$-W < \Delta x < W$$
$$-H < \Delta y < H$$

As an extra complication, due to the limited size of the window, the chances of finding a large vector $(\Delta x, \Delta y)$ are lower than finding small ones. When both Δx and Δy are positive, this windowing effect is illustrated in figure 2.3 which shows that, within the fixed image window, the vector $(\Delta x, \Delta y)$ can only be realized starting from the shaded fraction of the window area, otherwise the end of the vector would point out of the window.

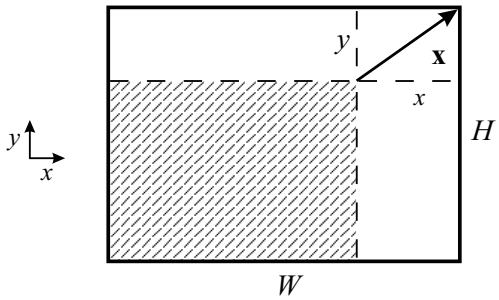

Figure 2.3: Schematic of the windowing effect on the correlation function for positive values of Δx and Δy.

Thus, the starting two-dimensional vector $\tilde{\mathbf{x}}$ must lie inside the region bounded by

$$\frac{1}{2}(|\Delta x| - \Delta x) < x < W - \frac{1}{2}(|\Delta x| + \Delta x)$$
$$\frac{1}{2}(|\Delta y| - \Delta y) < y < H - \frac{1}{2}(|\Delta y| + \Delta y)$$

for the two-dimensional vector $\tilde{\mathbf{x}} + \Delta\tilde{\mathbf{x}}$ to be observed. The absolute values have to be used, because the windowing effect limits the effective size of the image window also for two-dimensional displacement vectors $\Delta\tilde{\mathbf{x}}$ with negative components.

In addition, it is not obvious that all the tracers within the fluid volume will be detected under all circumstances, as occurs, for example, when the lighting is inhomogeneous or when the tracers are too closely together to be separated by both the human eye and sophisticated image analysis software. Therefore, it is reasonable to introduce the detection probability $S_{xy}(x,y)$ which varies over the image window. Ideally, when all the tracers can be detected, S_{xy} equals unity at all positions within

the image window. Although this can not be realized in practice, it is still possible to make S_{xy} almost a constant by carefully manipulating the lighting arrangement. But even so, its value will generally be slightly smaller than unity because, in any large collection of acquired images some of them will contain tracers that appear to be overlapping and cannot be located accurately.

The third dimension of the fluid volume is the z-direction, perpendicular to the object plane. Here, a finite volume around the focal plane of the optics will be observed due to the finite depth of focus ($d.o.f.$). Specifically, if $z = 0$ denotes the location of the focal plane, the depth of focus is usually defined so that the z-values at which tracer particles can be distinguished range from $-\frac{1}{2}d.o.f.$ to $+\frac{1}{2}d.o.f.$. As a result, the detection probability S_z will always be a very strong function of z. Even if we assume that S_z does not depend on the x- and y- positions (which is reasonable if the $d.o.f.$ is small compared to the window size), it will, by definition, have its maximum in the focal plane and vanish at $z = \pm d.o.f.$ where the tracers can no longer be distinguished from their surroundings.

Using the arguments presented in the preceding paragraphs, equation (2.2) can be written in the following way:

$$
\begin{aligned}
&C_{3D}(\Delta x, \Delta y, \Delta z; \Delta t) = \\
&\quad \int_{z_{\min}}^{z_{\max}} \int_{y_{\min}}^{y_{\max}} \int_{x_{\min}}^{x_{\max}} \left[\hat{n} S_{xy}(x,y) S_z(z) P_1(\mathbf{x})\right] \cdot \\
&\qquad\qquad \left[\hat{n} S_{xy}(x+\Delta x, y+\Delta y) S_z(z+\Delta z) P^{trans}(\Delta \mathbf{x}; \Delta t, \mathbf{x})\right] \, dx\, dy\, dz \\
&\quad + \int_{z_{\min}}^{z_{\max}} \int_{y_{\min}}^{y_{\max}} \int_{x_{\min}}^{x_{\max}} \left[\hat{n} S_{xy}(x,y) S_z(z) P_1(\mathbf{x})\right] \cdot \\
&\qquad\qquad \left[\hat{n} S_{xy}(x+\Delta x, y+\Delta y) S_z(z+\Delta z) P_2(\mathbf{x}+\Delta \mathbf{x}; \Delta t)\right] \, dx\, dy\, dz
\end{aligned}
\tag{2.4}
$$

where

$$
\begin{aligned}
x_{\min} &= x_0 - \frac{1}{2}W + \frac{1}{2}(|\Delta x| - \Delta x), \;\; x_{\max} = x_0 + \frac{1}{2}W - \frac{1}{2}(|\Delta x| + \Delta x), \\
y_{\min} &= y_0 - \frac{1}{2}H + \frac{1}{2}(|\Delta y| - \Delta y), \;\; y_{\max} = y_0 + \frac{1}{2}H - \frac{1}{2}(|\Delta y| + \Delta y), \\
z_{\min} &= z_0 - \frac{1}{2}dof + \frac{1}{2}(|\Delta z| - \Delta z), \; z_{\max} = z_0 + \frac{1}{2}dof - \frac{1}{2}(|\Delta z| + \Delta z)
\end{aligned}
$$

and $\hat{n}$ is the average number of tracers in the fluid volume which is introduced in order to normalize the probability density functions. In addition, (x_0, y_0, z_0) denotes the center of the object volume within which the measurements are being made. Both integrands in equation (2.4) involve a product of two terms: the first contains the probability that a tracer is observed at position $\mathbf{x}$ and the second the probability that a tracer –either the same (P^{trans}) or another (P_2)– is observed at position $\mathbf{x} + \Delta \mathbf{x}$ after

the time-interval Δt. The integration over x, y and z originates from the finite size of the object volume, discussed earlier.

The general equation (2.4) can be simplified by letting $P_1(\mathbf{x})$ be constant, which is permissible if the gradients in the concentration of the tracer particles are negligible on the scale of the window size. In addition, as was stated earlier, $S_{xy}(x,y)$ will be constant under appropriate experimental conditions. Consequently, equation (2.4) becomes

$$\begin{aligned} C_{3D}(\Delta\mathbf{x};\Delta t) = \\ K_1\,\hat{n}^2 \int_{z_{\min}}^{z_{\max}} \int_{y_{\min}}^{y_{\max}} \int_{x_{\min}}^{x_{\max}} S_z(z) S_z(z+\Delta z) P^{trans}(\Delta\mathbf{x};\Delta t,\mathbf{x})\; dx\, dy\, dz \\ +\; K_1\,\hat{n}^2 \int_{z_{\min}}^{z_{\max}} \int_{y_{\min}}^{y_{\max}} \int_{x_{\min}}^{x_{\max}} S_z(z) S_z(z+\Delta z) P_2(\Delta\mathbf{x};\Delta t)\; dx\, dy\, dz \end{aligned} \tag{2.5}$$

where $K_1 = P_1 \cdot S_{xy}^2$ is an $O(1)$ constant. Therefore, on substituting equation (2.5) into equation (2.1) we obtain that

$$\begin{aligned} C_{2D}(\Delta\tilde{\mathbf{x}};\Delta t) = \\ K_1\,\hat{n}^2 \int_{-dof}^{+dof} \int_{z_{\min}}^{z_{\max}} \int_{y_{\min}}^{y_{\max}} \int_{x_{\min}}^{x_{\max}} S_z(z) S_z(z+\Delta z) P^{trans}(\Delta\mathbf{x};\Delta t,\mathbf{x})\; dx\, dy\, dz\, d\Delta z \\ +\; K_1\,\hat{n}^2 \int_{-dof}^{+dof} \int_{z_{\min}}^{z_{\max}} \int_{y_{\min}}^{y_{\max}} \int_{x_{\min}}^{x_{\max}} S_z(z) S_z(z+\Delta z) P_2(\Delta\mathbf{x};\Delta t)\; dx\, dy\, dz\, d\Delta z \end{aligned} \tag{2.6}$$

where the integration over Δz is performed from the minimum ($-d.o.f.$) to the maximum ($+d.o.f.$) possible distance between tracers in the Δz-direction. The second term on the right hand side of equation (2.6) can be simplified further by considering special forms for $P_2(\mathbf{x}+\Delta\mathbf{x};\Delta t)$. Although some comments on this subject will be made at the end of the next subsection, a thorough analysis is beyond the scope of this thesis, which concerns exclusively the first term. Note that, in arriving at equation (2.6), no a priori assumptions on the transition probability density $P^{trans}(\Delta\mathbf{x};\Delta t,\mathbf{x})$ have been made. In the next section, equation (2.6) will be evaluated when the transition probability is that for the diffusive motion of tracers in a simple shear flow, on which our experimental work is focused.

2.2.3 The evaluation of self-diffusion coefficients in simple shear flow

The analysis discussed in the previous section directly links the experimental results to the transition probability density function of the tracers. Different theoretical hypotheses for $P^{trans}(\Delta\mathbf{x};\Delta t,\mathbf{x})$ can be introduced into equation (2.4) to check their validity. In this chapter we concentrate on the topic of self-diffusion in a concentrated suspension undergoing simple shear flow. Previous experiments have shown that, for

sufficiently long time-steps Δt, the motion of the particles can be viewed as a diffusion process with different diffusion coefficients along the characteristic flow axes (flow, velocity gradient and vorticity direction). In such a case, the transition probability density $P^{trans}(\Delta\mathbf{x};\Delta t,\mathbf{x})$ satisfies the general convective diffusion equation:

$$\frac{\partial P^{trans}}{\partial t} = -\nabla\cdot(\mathbf{v}\,P^{trans}) + \nabla\cdot\mathbf{D}\cdot\nabla P^{trans} \tag{2.7}$$

with initial condition $P^{trans}(\Delta\mathbf{x};0,\mathbf{x}_0)=\delta(\Delta\mathbf{x})$, where $\mathbf{v}$ is the convective bulk particle velocity. For a stationary simple shear flow $\mathbf{v}=(\dot\gamma y,0,0)$, with the x-axis in the flow direction and the y-axis in the velocity gradient direction. The diffusion tensor $\mathbf{D}$ is defined by

$$\langle\Delta\mathbf{x}\,\Delta\mathbf{x}\rangle \sim 2\,\mathbf{D}\,\Delta t = 2\begin{bmatrix} D_{xx} & D_{xy} & 0\\ D_{yx} & D_{yy} & 0\\ 0 & 0 & D_{zz}\end{bmatrix}\Delta t \tag{2.8}$$

D_{xx}, D_{yy} and D_{zz} being the diffusion coefficients in the different directions. Due to symmetry, all the off-diagonal elements of $\mathbf{D}$ are zero except for D_{xy} and D_{yx} which are equal (see Brady & Morris, 1997). The solution of equations (2.7) and (2.8) can be written in the form (see Van Kampen, 1992):

$$P^{trans}(\Delta\mathbf{x};\Delta t,\mathbf{x}) = \frac{1}{(2\pi)^{\frac{3}{2}}\sigma_x\sigma_y\sigma_z}\cdot\exp\left(-\frac{(\Delta x-\frac{1}{2}\dot\gamma\Delta t(\Delta y+2y)-\Delta y\frac{D_{xy}}{D_{yy}})^2}{2\sigma_x^2}-\frac{(\Delta y)^2}{2\sigma_y^2}-\frac{(\Delta z)^2}{2\sigma_z^2}\right) \tag{2.9}$$

where

$$\sigma_x^2 = 2D_{xx}\Delta t\left(1+\frac{1}{12}\dot\gamma^2\Delta t^2\frac{D_{yy}}{D_{xx}}-\frac{D_{xy}^2}{D_{xx}D_{yy}}\right),\ \sigma_y^2=2D_{yy}\Delta t\ \text{ and }\ \sigma_z^2=2D_{zz}\Delta t$$

On inserting equation (2.9) into equation (2.6) and integrating with respect to x, y and Δz, we obtain

$$\begin{aligned} C_{2D}(\Delta x,\Delta y;\Delta t) = {} & K_1\,\hat n^2\,\psi(\Delta t)\,\chi(\Delta t;dof)\,(W-|\Delta x|)\cdot\exp\left(-\frac{(\Delta y)^2}{2\sigma_y^2}\right)\cdot \\ & \frac{\sqrt{\pi}\sigma_x}{\sqrt{2}\dot\gamma\Delta t}\cdot\left(\operatorname{erf}\left[\frac{\Xi_1(\Delta x,\Delta y;\Delta t)}{\sqrt{2}\sigma_x}\right]-\operatorname{erf}\left[\frac{\Xi_2(\Delta x,\Delta y;\Delta t)}{\sqrt{2}\sigma_x}\right]\right) \\ & +\ K_1\,\hat n^2\,(W-|\Delta x|)\,(H-|\Delta y|)\int_{-dof}^{+dof}\int_{z_{\min}}^{z_{\max}} S_z(z)S_z(z+\Delta z)P_2(\Delta\mathbf{x};\Delta t)\,dz\,d\Delta z \end{aligned} \tag{2.10}$$

where

$$\chi(\Delta t; dof) = \int_{-dof}^{+dof} \int_{z_{\min}}^{z_{\max}} S_z(z) S_z(z+\Delta z)\ \exp\left(-\frac{(\Delta z)^2}{2\sigma_z^2}\right)\ dz\, d\Delta z \tag{2.11}$$

$$\psi(\Delta t) = \frac{1}{(2\pi)^{\frac{3}{2}}\sigma_x\sigma_y\sigma_z} \tag{2.12}$$

$$\Xi_1(\Delta x, \Delta y; \Delta t) = \Delta x - \frac{1}{2}\dot{\gamma}\Delta t\,(2y_0 - H + |\Delta y|) - \Delta y\frac{D_{xy}}{D_{yy}} \tag{2.13}$$

and

$$\Xi_2(\Delta x, \Delta y; \Delta t) = \Delta x - \frac{1}{2}\dot{\gamma}\Delta t\,(2y_0 + H - |\Delta y|) - \Delta y\frac{D_{xy}}{D_{yy}} \tag{2.14}$$

Equation (2.10) describes the shape of the experimentally determined function $C_{2D}(\Delta x, \Delta y; \Delta t)$ for the case of a diffusive tracer motion in a simple shear flow. As will be shown in the more detailed description of the data analysis in section 3.3, this expression can be simplified further and then used to calculate the diffusion coefficient D_{yy} by analyzing only the width of the auto-correlation peak of $C_{2D}(\Delta x, \Delta y; \Delta t)$ in the Δy-direction. Note that the amplitude of the auto-correlation part (first term) depends on the window size, the time step (through χ and ψ) and on the depth of focus of the optical system (through χ), but not on D_{yy}.

The preceding analysis can also be performed when the image plane is in the Δx-Δz-plane, which is the case when the suspension is viewed from the velocity gradient direction. Here, however, the counterpart of equation (2.10) is simply:

$$\begin{aligned} &C_{2D}(\Delta x, \Delta z; \Delta t) = \\ &K_2\,\hat{n}^2\,\psi(\Delta t)\,\xi(\Delta x, \Delta t; dof)\,(W - |\Delta x|)\,(|H - \Delta z|)\ \exp\left(-\frac{(\Delta z)^2}{2\sigma_z^2}\right) \\ &+\ K_2\,\hat{n}^2\,(W - |\Delta x|)\,(H - |\Delta z|)\int_{-dof}^{+dof}\int_{y_{\min}}^{y_{\max}} S_y(y) S_y(y+\Delta y) P_2(\Delta \mathbf{x}; \Delta t)\ dy\, d\Delta y \end{aligned} \tag{2.15}$$

where

$$\begin{aligned} \xi(\Delta x, \Delta t; dof) = &\int_{-dof}^{+dof}\int_{y_{\min}}^{y_{\max}} S_y(y) S_y(y+\Delta y)\cdot \\ &\exp\left(-\frac{(\Delta x - \frac{1}{2}\dot{\gamma}\Delta t(\Delta y + 2y) - \Delta y\frac{D_{xy}}{D_{yy}})^2}{2\sigma_x^2} - \frac{(\Delta y)^2}{2\sigma_y^2}\right)\ dy\, d\Delta y \end{aligned} \tag{2.16}$$

and $K_2 = P_1 \cdot S_{xz}^2$ is a constant which is slightly different from K_1. The above differs from equation (2.10) in the sense, that the shape of the auto-correlation peak in the

Δz-direction is simply that of a Gaussian peak, with a width that only depends on the diffusion coefficient D_{zz}. Consequently, equation (2.15) enables one to calculate the diffusion coefficient D_{zz} by analyzing the width of the auto-correlation peak of $C_{2D}(\Delta x, \Delta y; \Delta t)$ in the Δz-direction. Equation (2.16) is somewhat more complicated than equation (2.11) because, now ξ depends on both Δx and Δt.

Of course, the cross-correlation parts of equations (2.10) and (2.15) cannot be neglected in calculating the diffusion coefficients from the experimentally obtained functions C_{2D} because this part influences the shape of the correlation function in the region of the auto- correlation peak and must be subtracted out during the fitting procedures. To achieve this we recall that, as was mentioned in section 2.2.2, $P_2(\Delta\mathbf{x}; \Delta t)$ contains information about the distribution of different particles in consecutive images and is therefore closely related to the pair-distribution function. Symmetry arguments, therefore, are sufficient to eliminate the cross-correlation term in a simple shear flow. Specifically, as shown in figure 2.4, the Δx-Δy-plane on which our function is measured can be divided into four quadrants with the original position of the tracer being at the origin so that, in simple shear, the flow in quadrants II and IV is compressive and in quadrants I and III extensional. But, since the flow in quadrants I and III is equivalent and similarly in quadrants II and IV, the pair-distribution function has an obvious symmetry in that each point $A(\Delta x, \Delta y)$ has a counterpart $A'(-\Delta x, -\Delta y)$ where the pair-distribution function is the same. This symmetry should also apply to the function $P_2(\Delta\mathbf{x}; \Delta t)$ and, as will be shown in section 2.3.3, this argument enables one to eliminate the cross-correlation contribution from the measured experimental data in an elegant way.

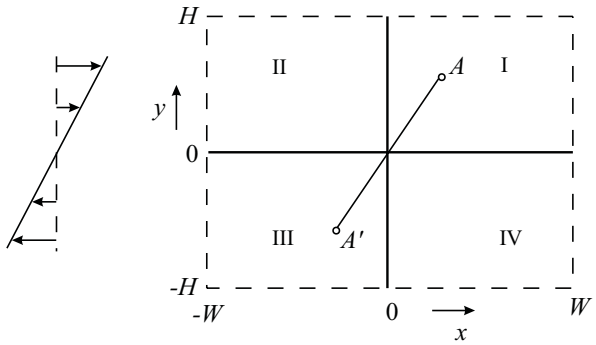

Figure 2.4: Schematic of four quadrants in the Δx-Δy-plane on which the function C_{2D} is measured. The origin refers to the original position of the tracer.

2.2.4 Previous experimental work

The general idea of the technique described above is in some respects similar to other well-known experimental methods, for example Particle Image Velocimetry (PIV), where in order to measure the velocity field in complex flow geometries, the fluid is seeded with small tracers which accurately follow the flow because of their small size. One difference, however, is that, whereas PIV uses very small time intervals Δt between the images to calculate velocity vectors, the time-intervals are considerably larger in the present application so as to maximize the displacements of the tracers.

On the other hand, Eckstein *et al.* (1977) and Leighton & Acrivos (1987a) examined the phenomenon of self-diffusion by investigating the motion of a single labeled sphere immersed in a suspension of otherwise identical spheres being sheared in a Couette device. In their technique, the radial position (the velocity gradient direction) of the labeled sphere was measured after each rotation (Eckstein *et al.*) or inferred from the time taken for the particle to complete a transit of the device (Leighton & Acrivos). These data were then related to the random walk in the radial direction. Recently, Phan & Leighton (1993) also measured the self-diffusivity in the vorticity direction by observing the vertical position of a marked sphere each time it passed an observation window. It is worth remarking at this point that in the experiments of both Leighton & Acrivos (1987a) and Phan & Leighton (1993), the strain $\dot{\gamma}\Delta t$ was at least of $O(10)$, which, as will be shown presently, is more than an order of magnitude larger than in our experiments.

2.3 Experimental work

In this section we present the experimental details of our measurements of the shear-induced coefficient of particle self-diffusion. The basic approach consisted of evaluating the positions of tracer particles, immersed in a suspension of otherwise identical spheres, being sheared in a narrow gap Couette device.

2.3.1 Apparatus and materials

The experiments were performed in a narrow gap cylindrical Couette device, shown in figure 2.5, which consisted of two cylinders made of high quality plexiglass. The inner radius of the outer stationary cylinder (R_O) was 8.224 cm and the outer radius of the inner rotating cylinder (R_I) was 7.542 cm, giving a gap size equal to 0.682 cm. The inner cylinder was mounted on a shaft, which in turn was mounted on a computer controlled feedback motor (ID Corp., California). Also, the shaft was aligned accurately with two bearings separated by O-rings. A great advantage of this design is that its transparency enabled us to provide uniform lighting to the imaging volume.

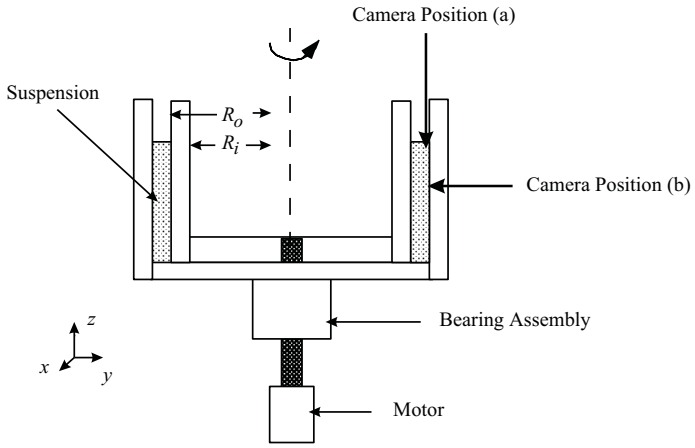

Figure 2.5: Schematic of the Couette device and the camera positions (a) and (b) for observations in, respectively, the velocity gradient and vorticity directions.

The particles used in the experiments were class 4F acrylic spheres obtained from ICI. Their density was measured to be 1.172 g/ml and the spheres containing air bubbles were removed by density segregation. The polydisperse material was sieved many times to obtain the diameter range $90 \pm 15\,\mu m$. Following the recipe of Krishnan *et al.* (1996), a suspension of these particles was made using a mixture of 77.38% Triton X-100, 9.23% water and 13.39% anhydrous zinc chloride (weight percentages) which matched the refractive index and density of the acrylic spheres. The pure suspending fluid had a viscosity of 3.4 Pa·s at the operating temperature of 23°C. Tracer particles were prepared by dyeing part of the acrylic spheres with RIT liquid fabric dye and their density was also found to be close to 1.172 g/ml. A small amount of the tracer particles (typically 0.4 vol.% in our experiments) were then added to the suspension. The suspension was sheared for several hours to achieve a uniform concentration and to drive out any air bubbles. The experiments were carried out at two shear rates (0.78 s^{-1} and 1.8 s^{-1}) for particle volume fractions of 20%, 30%, 40% and 50%.

2.3.2 Image analysis

The motion of the tracer particles was observed by viewing two small volumes of the suspension from positions (a) and (b), shown in figure 2.5, using a high resolution (1008 $\times$ 1018 pixels) CCD camera (Kodak MegaPlus ES1.0) with Infinity Optics (8$\times$ magnification). For lighting we used a Fiber Optic Illuminator (Cole Parmer Instrument Company) that provided an excellent contrast in the image. The camera was mounted on a three-dimensional traversing system, which allowed us to focus the

camera precisely at the desired locations. Images from the CCD camera were passed via an 8-bit digital video signal to a dedicated image acquisition and processing board (Oculus F64 by Coreco Inc.) which operated on a personal computer equipped with a 200 MHz Intel Pentium Processor. We programmed the frame buffer arrays of the F64 board to enable the acquisition of 5 consecutive images at equal time intervals Δt (with $\Delta t_{\min} = 55$ ms) before storing the images into the hard disk of the computer. This program was typically run with 100 loops to acquire and store 500 images automatically. The grabbing times of all the images were stored for further analysis.

We used the positions (a) and (b), shown in figure 2.5, to measure the self-diffusion coefficients in the velocity gradient and in the vorticity directions respectively. When viewing from position (a) the center of the fluid element $W \times H \times d.o.f.$ of the suspension was chosen 1.7 cm above the bottom and 1 mm inside the outer wall of the Couette gap. When viewing from position (b), the center of the imaging volume was kept at 1 mm below the top interface and at 1.5 mm inside the outer wall of the Couette gap. These positions were chosen to reduce the wall effects as far as possible. The cross-sectional area, $W \times H$, was calculated using the known magnification of the camera optics and in our experiments was found to be 1.17 mm$\times$1.18 mm. The depth of focus, $d.o.f.$, was determined by viewing a 45° inclined plane through the camera with the preset optics. The inclined plane had four sets of target columns containing different numbers of line pairs per millimeter. The resolution appropriate for the given magnification was then chosen and the distance up to which the line pairs were distinctly visible was measured. This distance was read from either the computer monitor or the scale on the inclined plane. Using this technique, the depth of focus was found to be 425 ± 25 μm.

The positions of the tracer particles in each digitized image were accurately determined using the imaging software (Visilog 5.1 by Noesis Vision Inc.). This software stretched the pixel-grey value dynamic range (process called equalization) to make the details more visible and then removed the unwanted small scale noise. After running a binarization operation, border particles were eliminated and analysis procedures were performed on the dark objects in the image. These procedures involved the calculation of the areas, sphericities, blackness and positions of the dark objects. If the properties met our pre-set criteria, an object was counted as being a tracer and the position of its center was stored in a file. In this way, all the images were scanned and all the tracers and their locations were identified.

For our self-diffusion measurements, a large number of images were taken for each run in order to ensure good ensemble averaging. Typically, we acquired 500 images. The positions of the tracers, as obtained from the measurements described above, were then used to generate the correlation functions C_{2D} for each set. The method for generating these functions and evaluating the self-diffusion coefficients will now be described.

2.3.3 Data analysis

The data on the positions of all the tracer particles in the images were used to calculate the correlation function $C_{2D}(\Delta x, \Delta y; \Delta t)$ in the following way. For the total ensemble, the two-dimensional displacement vectors $(\Delta x_{nm}, \Delta y_{nm})$ were calculated for all combinations of the tracers in consecutive images, as described in section 2.1. The Δx-Δy-domain ($-W \leq \Delta x \leq W$ and $-H \leq \Delta y \leq H$) was discretized in $N_{\Delta x} \times N_{\Delta y}$ small area elements, usually called numerical bins. All the vectors $(\Delta x_{nm}, \Delta y_{nm})$ were put into the corresponding numerical bin. The number of vectors in each bin was then divided by the number of images, N_{ima}, and by the area covered by each numerical bin, $2W/N_{\Delta x} \cdot 2H/N_{\Delta y}$, to arrive at the normalized value of the correlation function $C_{2D}(\Delta x, \Delta y; \Delta t)$ at the position of the center of the bin. The normalization procedure is necessary to obtain the correct value if numerical integration is performed and to allow comparison with the theoretical predictions of equations (2.10) and (2.15). The number of bins $N_{\Delta x} \times N_{\Delta y}$ must be small enough in order for each bin to contain a sufficient number of vectors for further analysis, but large enough to provide information on the behaviour of the correlation function at small length scales.

From each ensemble of images, the correlation function could be obtained for different time-steps, by not only comparing consecutive images at a time interval Δt, but by also analyzing image combinations at other intervals $(2 \cdot \Delta t, 3 \cdot \Delta t)$ within one grabbing sequence of 5 images.

Using the data analysis procedure described above, three-dimensional plots could be generated of the function $C_{2D}(\Delta x, \Delta y; \Delta t)$ on the Δx-Δy-plane. Because in our experimental set-up the particles moved from left to right due to convection, the auto-correlation peak in equations (2.10) and (2.15) was always located at positive values of Δx. As a result, the values of the correlation function $C_{2D}(\Delta x, \Delta y; \Delta t)$ for $\Delta x > 0$ involve a combination of an auto- and a cross-correlation, whereas the values of $C_{2D}(\Delta x, \Delta y; \Delta t)$ for $\Delta x < 0$ consist only of cross-correlation contributions. Using the symmetry argument presented in section 2.3, the auto-correlation part of $C_{2D}(\Delta x, \Delta y; \Delta t)$ can then be obtained by calculating:

$$C_{2D}^{auto}(\Delta x, \Delta y; \Delta t) = C_{2D}(\Delta x, \Delta y; \Delta t) - C_{2D}(-\Delta x, -\Delta y; \Delta t) \quad \text{for } \Delta x \geq 0 \tag{2.17}$$

In order to evaluate the diffusion coefficients we focused our quantitative analysis on the displacements Δy in the velocity gradient (and Δz in the vorticity direction). Since we are not interested in the Δx-displacements, we used a very small number of bins in Δx, $N_{\Delta x} = 2$, i.e. one for negative and one for positive Δx-values. Then, after performing the subtraction of equation (2.17), we integrated $C_{2D}^{auto}(\Delta x, \Delta y; \Delta t)$ over Δx to obtain (see equation (2.10)):

$$C_{1D}^{auto}(\Delta y; \Delta t) = A \cdot \exp\left(-\frac{(\Delta y)^2}{2\sigma_y^2}\right) \tag{2.18}$$

with

$$A = K_1\,\hat{n}^2\,\psi(\Delta t)\,\chi(\Delta t; dof)\,\frac{\sqrt{\pi}\sigma_x}{\sqrt{2}\dot{\gamma}\Delta t}\cdot \int_{-W}^{W}(W-|\Delta x|)\cdot\left(\operatorname{erf}\left[\frac{\Xi_1(\Delta x,\Delta y;\Delta t)}{\sqrt{2}\sigma_x}\right]-\operatorname{erf}\left[\frac{\Xi_2(\Delta x,\Delta y;\Delta t)}{\sqrt{2}\sigma_x}\right]\right)\,d\Delta x \tag{2.19}$$

In principle, as seen from the above, Δy should also enter into the expression for the amplitude A in view of equations (2.13) and (2.14) thereby complicating the data analysis. But since $|\Delta y|$ is of the order of the particle radius a (and, similarly, for $\Delta y\frac{D_{xy}}{D_{yy}}$ provided that $\frac{D_{xy}}{D_{yy}}$ is $O(1)$ or smaller), while H, y_0 and W are all $O(1\text{ mm})$ and therefore an order of magnitude larger, the amplitude A becomes independent of $|\Delta y|$ with an error of $O(a/H)$. Consequently, the width of the peak of C_{1D}^{auto} determines σ_y^2 which, in view of equation (2.9), equals twice the product of D_{yy} with the time-interval Δt, so that the diffusion coefficient can be determined by fitting the experimental data with equation (2.18).

We followed a similar procedure for analyzing the function $C_{2D}(\Delta x,\Delta z;\Delta t)$ and calculating the diffusivity D_{zz} in the vorticity direction. Again, after subtracting the cross-correlation part, we integrated $C_{2D}^{auto}(\Delta x,\Delta z;\Delta t)$ over Δx to obtain (see equation (2.15)):

$$C_{1D}^{auto}(\Delta z;\Delta t) = B\cdot(H-|\Delta z|)\cdot\exp\left(-\frac{(\Delta z)^2}{2\sigma_z^2}\right) \tag{2.20}$$

with

$$B = K_2\,\hat{n}^2\,\psi(\Delta t)\int_{-W}^{W}\xi(\Delta x,\Delta t;dof)\,(W-|\Delta x|)\,d\Delta x$$

As $H \gg |\Delta z|$, the square of the width σ_z of this peak equals twice the product of the diffusion coefficient D_{zz} and the time interval Δt (see also equation (2.9)). Hence the diffusion coefficient D_{zz} can be determined by fitting the experimental data with equation (2.20).

In summary then, the diffusion coefficients D_{yy} and D_{zz} can be calculated by reducing the two-dimensional functions $C_{2D}(\Delta x,\Delta y;\Delta t)$ and $C_{2D}(\Delta x,\Delta z;\Delta t)$ to their one-dimensional equivalents, resp. $C_{1D}(\Delta y;\Delta t)$ and $C_{1D}(\Delta z;\Delta t)$, and by subsequently fitting the resulting curves with the Gaussian peaks of equation (2.18) and (2.20). The amplitudes A and B of the respective equations (2.18) and (2.20) peaks were not analyzed thoroughly, because they contain a number of unknown functions.

2.4 Results and discussion

2.4.1 Validation of the technique

Using the experimental set-up, images were obtained of sufficiently high quality to carry out the required accurate image analysis procedures. A typical example of our image quality is shown in figure 2.6, which depicts a sample of two consecutive images ($\Delta t = 220$ ms) in a suspension with particle concentration $\phi = 0.30$ being sheared at the rate $\dot{\gamma} = 1.79\ \mathrm{s}^{-1}$.

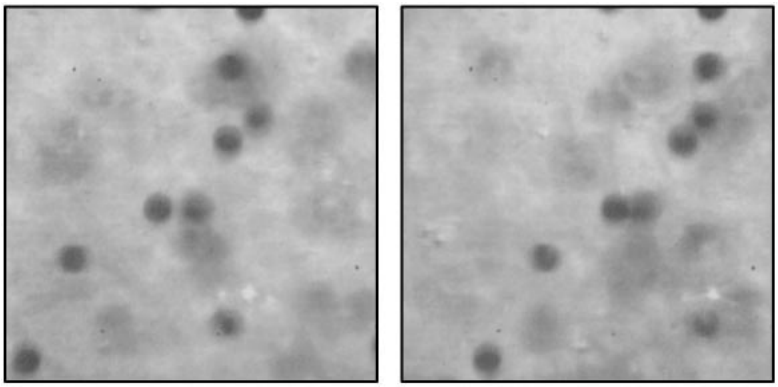

Figure 2.6: Photographs of two successive images taken 220 ms apart in a 30% concentrated suspension sheared at $1.79\ \mathrm{s}^{-1}$. Here, the flow is from left to right.

In order to ensure that any observed self-diffusivity in a concentrated suspension was due only to the diffusive motion of the tracers, it was necessary to rule out the existence of any significant errors in our experimental set-up or in the image analysis procedure. The possible errors in the former included mechanical vibrations, rotation irregularities of the motor, non-uniformities in the Couette gap and misalignment of camera-optics. In addition, we expected some error in the calculation of the particle locations by the image analysis procedure. Although the importance of the image analysis error could not be estimated a priori, the errors originating from this source were minimized by applying homogeneous lighting and optimizing the contrast.

In order to quantify these errors, we performed measurements in a dilute suspension ($\phi = 0.4\%$) of only tracer particles, where the self-diffusivity was expected to be negligible compared to the self-diffusivities reported in the literature for concentrated suspensions. Following the procedures described in section 2.3, the broadening of the correlation peaks in both the velocity gradient and vorticity direction was measured. This broadening is believed to be the result of the systematic errors mentioned above. If it was interpreted as self-diffusion, we found that the value of the associated diffusion coefficient was at most 10% of the values we observed for the concentrated

suspensions at 30% volume fraction. The influence of the image analysis procedures on the diffusivity results was also checked and the results were found to be insensitive to changes in the criteria which we used for the detection of tracer particles in the images. These measurements in the dilute suspension showed that the contributions of the experimental errors were small. Hence, we applied the technique to determine the self- diffusivity in concentrated suspensions.

2.4.2 Particle self-diffusion in concentrated suspensions

The diffusion-coefficient experiments were conducted at solids concentrations ranging from 20 to 50% for values of $\dot{\gamma}\Delta t$ ranging from 0.05 to 0.5.

In figure 2.7 we present three-dimensional correlation plots for the case of $\phi = 0.30$ at $\dot{\gamma}\Delta t = 0.085$ and 0.34, where $C_{2D}(\Delta x, \Delta z; \Delta t)$ is shown as a function on the Δx-Δz-plane according to the analysis procedures described in section 2.3.2. The Δx- and Δz-axis respectively represent the correlation distances in the velocity and vorticity gradient direction. The units of the displacements in the figures are pixels, for direct reference to the images. The auto-correlation peak is clearly distinguishable and is dominant over the cross-correlation contribution, which appears as the scatter in the rest of the plane. The width in the Δx-direction is the result of variations in the convective velocity over the window (see figure 2.2); in the Δz-direction the width is governed by the diffusive process and is much smaller. As the time-step Δt increases –from figure 2.7*a* to *b*–, the convective displacements increase and the peak shifts to the right. Also, the amplitude of the peak decreases, as fewer particles are detected in two consecutive images. These observations are in qualitative agreement with our expectations and figure 2.7 further validated our choice of the number of images acquired per run and the time interval Δt between consecutive images.

For a quantitative analysis, the three-dimensional plots of figure 2.7 were reduced to plots of $C_{1D}(\Delta z; \Delta t)$ as discussed in section 2.3.3. Figure 2.8 shows the graphs of $C_{1D}(\Delta z; \Delta t)$ versus Δz for the same experimental data as presented in figure 2.7, after subtraction of the cross-correlation part. Again, the displacements are expressed in pixels, but this could easily be transformed into SI-units by using the known camera magnification (1 pixel $\cong$ 1.16 μm). The graphs also show the best possible fit with a Gaussian peak. It must be noted, that although the width of the peak is small compared to the particle size, a clear broadening can be observed in going from figure 2.8*a* to *b*, where Δt is increased.

The decrease in the peak height with increasing values of $\dot{\gamma}\Delta t$ also limits the range over which experiments could be performed, because the auto-correlation peak has to be distinguishable from the cross-correlation contribution. In our experimental set-up, measurements could be carried out for $\dot{\gamma}\Delta t$ ranging from 0.05 to 0.5. For larger $\dot{\gamma}\Delta t$ the particles did not remain within the window long enough to be detected in two consecutive images and thus contribute to the peak. This limitation was mainly

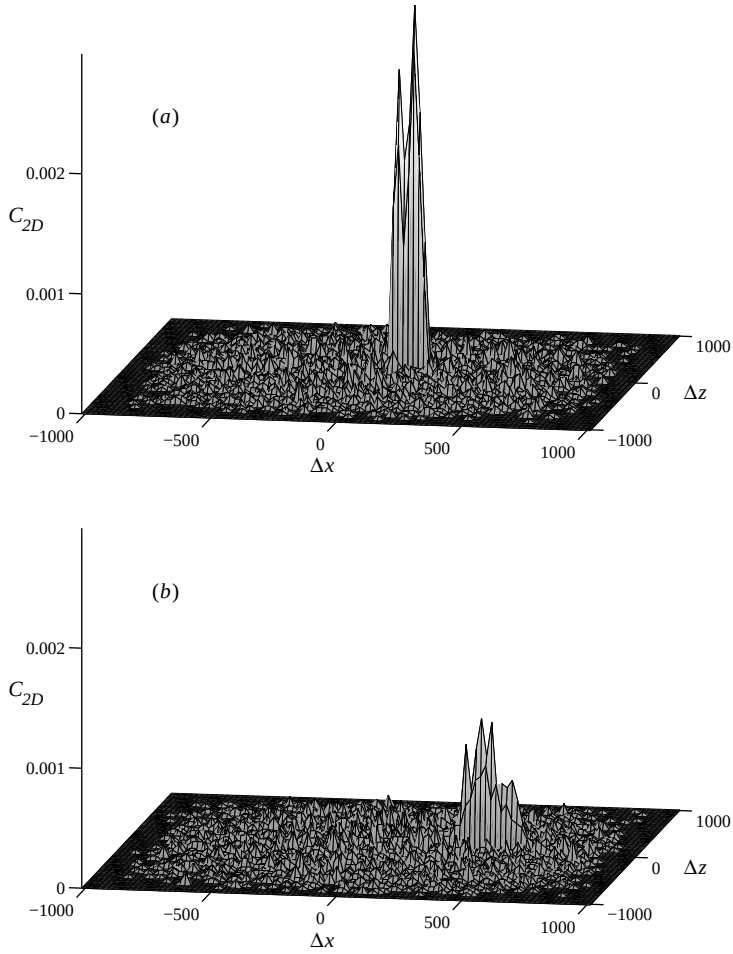

Figure 2.7: Plots of the experimentally determined correlation function C_{2D} in the Δx-Δz-plane for $\phi = 0.30$ and $\dot{\gamma}\Delta t = 0.085$ *(a)* & 0.34 *(b)*.

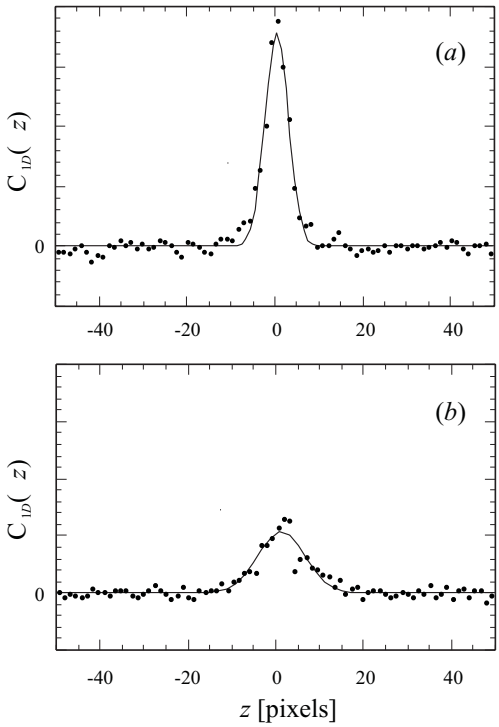

Figure 2.8: Plots of the experimentally determined correlation function C_{1D} vs. the displacement Δz for $\phi = 0.30$ and $\dot{\gamma}\Delta t = 0.085$ *(a)* & 0.34 *(b)*.

caused by the fact that the experiments had to be performed in a region far enough from the wall of the outer cylinder to reduce wall effects as far as possible. The result is of a trade-off between the need of staying away from the wall and maximizing the range of $\dot{\gamma}\Delta t$.

The width of the peaks in figure 2.8 is equal to the parameter σ_z defined in equation (2.9): $\sigma_z^2 = 2\,D_{zz}\,\Delta t$. For further analysis of the diffusion coefficient D_{zz} (and D_{yy}) and comparison with the results of other studies, the dimensionless scaling $\hat{D} = D/\dot{\gamma}a^2$ must be introduced, where a is the particle radius. Using this formulation we therefore introduce the following two dimensionless diffusion coefficients:

$$\frac{\sigma_i^2}{a^2} = 2\,D_{ii}\,\dot{\gamma}\Delta t \qquad i = y, z \tag{2.21}$$

For all experiments, the width of the peak has been determined and the results are presented in figure 2.9*a* to *d* where the dimensionless values σ_y^2/a^2 and σ_z^2/a^2 are plotted versus $\dot{\gamma}\Delta t$ for the different volume fractions. These figures show that the linear scaling of equation (2.21) applies over almost the entire range of $\dot{\gamma}\Delta t$, i.e. from $\dot{\gamma}\Delta t = 0.05$ to 0.5, although for $\phi = 0.20$ the linearity is not as clear as for the other experiments because the width of the auto-correlation peak is small and hence cannot be determined with much accuracy. The particle motion can, therefore, be described as a diffusive process on this timescale and the diffusive character seems to exist over the entire range. This is rather surprising, because it was generally believed thus far that diffusive behaviour could only be attained for experimental timescales $\dot{\gamma}\Delta t > 1$, i.e. when the timescales are larger than the assumed collision time in a simple shear flow and a particle has experienced several interactions.

Following equation (2.21), the dimensionless diffusion coefficients $\hat{D}_{yy}$ and $\hat{D}_{zz}$ can be calculated as one half the slope of the linear fits shown in figures 2.9*a* to *d*. In all these figures, the diffusion coefficient in the velocity gradient direction ($\hat{D}_{yy}$) is considerably larger than in the vorticity direction ($\hat{D}_{yy}$) with the ratio being about 1.7 for all volume fractions.

Our results for the diffusion coefficients are plotted in figure 2.10*a* and *b* together with the results of the previous studies by Eckstein *et al.* (1977), Leighton & Acrivos (1987a) and Phan & Leighton (1993). Although these earlier experiments were performed for $\dot{\gamma}\Delta t \gg 1$ by measuring the transit time and position of single tracer particles, they are in remarkable agreement with our results for which $\dot{\gamma}\Delta t < 1$. The error bars drawn for our data represent the uncertainty in the linear fits of figures 2.9*a* to *d*; this error turned out to be dominant over the systematic errors, which were discussed in the previous section.

The self-diffusion coefficients $\hat{D}_{yy}$ and $\hat{D}_{zz}$ increase rapidly with increasing particle concentration, as was reported in all previous experimental studies, but their values appear to asymptote at $\phi = 50\%$. The same trend was also observed in the experiments by Phan & Leighton (1993).

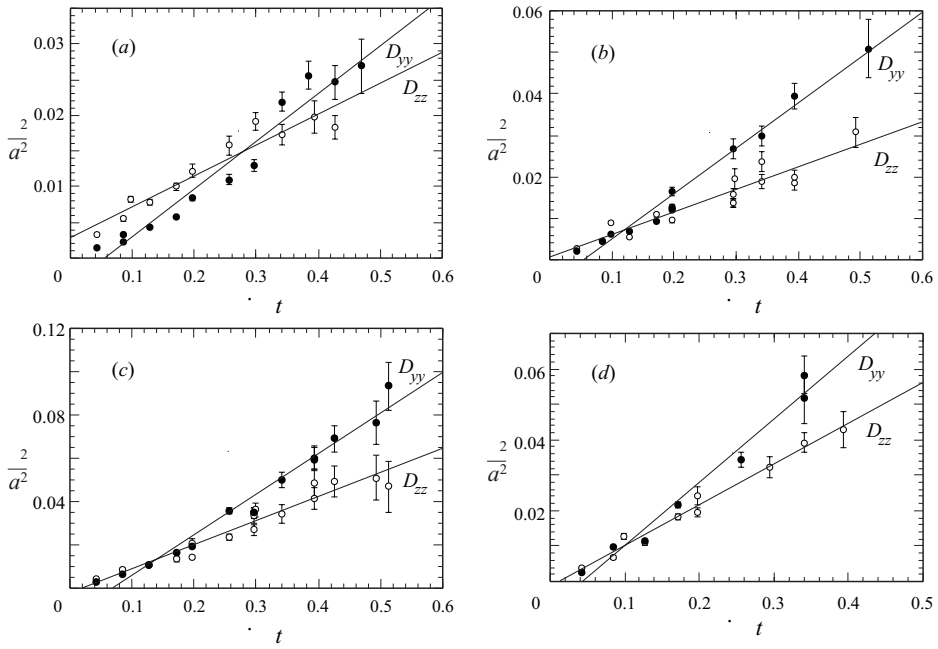

Figure 2.9: Plots of σ^2/a^2, the dimensionless variance of the correlation peak vs. $\dot{\gamma}\Delta t$ for $\phi = 0.20$ *(a)*, 0.30 *(b)*, 0.40 *(c)* and 0.50 *(d)*; the figures show the results for both the velocity gradient (●) and vorticity (○) directions.

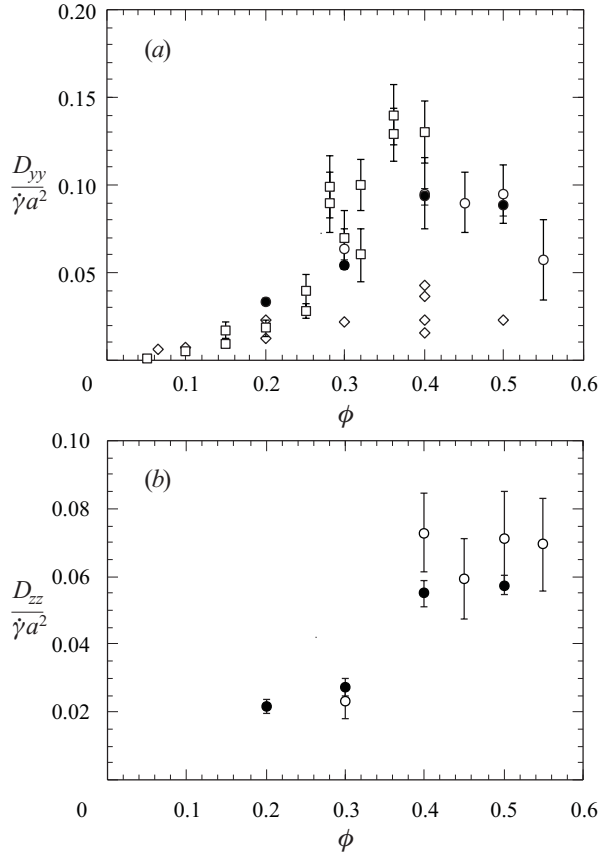

Figure 2.10: Comparison of the present results with previous experimental data for *(a)* the velocity gradient direction and *(b)* the vorticity direction. ○–from Phan & Leighton (1993), □–from Leighton & Acrivos (1987a), ◊–from Eckstein *et al.* (1977), ●–from this study.

2.4.3 Fluid tracer-diffusion in concentrated suspensions

The fluid-diffusion coefficients were estimated by examining the motion of small tracers ($31.5 \pm 6.5\,\mu$m in diameter) within a concentrated suspension of $325 \pm 25\,\mu$m diameter particles having concentrations ranging from 30 to 50% and for values of $\dot{\gamma}\Delta t$ ranging from 0.1 to 0.4. It is assumed that the motion of these tiny tracers represented the true fluid element motion in a suspension of large particles.

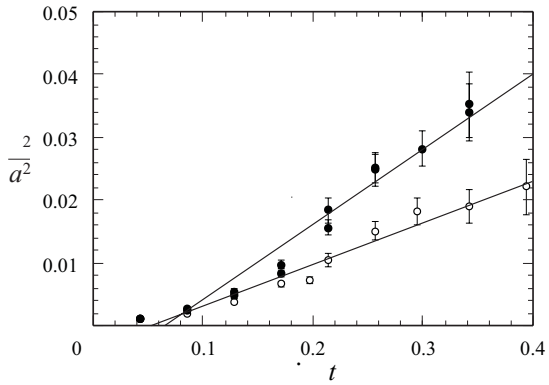

Figure 2.11: Plots of σ^2/a^2, the dimensionless variance of the correlation peak vs. $\dot{\gamma}\Delta t$ for ϕ=0.40; the figure shows the results for both the velocity gradient (●) and vorticity (○) directions.

Following the method described in the subsection 2.4.2, the dimensionless fluid tracer diffusivities D^f_{yy} and D^f_{zz} are calculated as one half the slope of the linear fits in plots of the dimensionless variance of the correlation peak vs. $\dot{\gamma}\Delta t$. In figure 2.11, we present one such plot for ϕ=0.40 in both the velocity gradient and vorticity directions. Our results for the fluid diffusion coefficients are plotted in figures 2.12*a* and *b* together with the results of the particle diffusivities reported earlier in figures 2.10*a* and *b*. Note that the diffusivities are scaled with $\dot{\gamma}a^2$, where a is the radius of particles making up the suspension. Unfortunately, measurements in the velocity gradient direction could not be performed, for the case $\phi = 0.5$ due to existence of a significant curvature in the interface between the suspension and the air above it. Clearly, the fluid tracer-diffusion coefficients are about 0.7 times the corresponding particle diffusion coefficients.

Acknowledgments

The work described in this chapter was supported in part by the US Department of Energy under Grant No. DE-FG02-90ER14139A008. Professor J.F. Brady is thanked for his useful comments and for providing the original of figure 2.1.

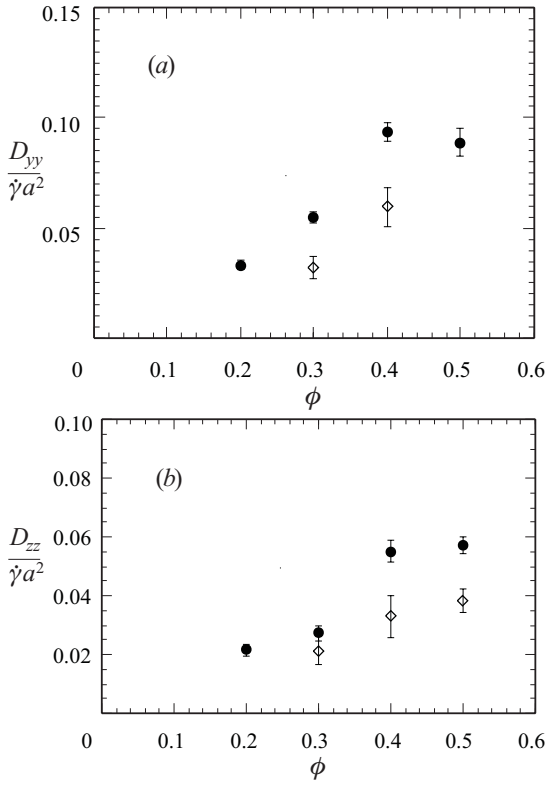

Figure 2.12: Comparison of the fluid and particle tracer-diffusivity experimental data for *(a)* the velocity gradient direction and *(b)* the vorticity direction. ◊–fluid tracer diffusivity, ●–particle self-diffusivity.

References

BOSSIS, G. & BRADY, J.F. 1987 Self-diffusion of Brownian particles in concentrated suspensions under shear. *J. Chem. Phys.* **87**, 5437–5448.

BRADY, J.F. 1997 Shear-induced diffusion and particle migration. Presented at AIChE Annual Meeting 1997, session 29D, Los Angeles.

BRADY, J.F. & MORRIS, J.F. 1997 Microstructure of strongly sheared suspensions and its impact on rheology and diffusion. *J. Fluid Mech.* **348**, 103–139.

ECKSTEIN, E.C. , BAILEY, D.G. & SHAPIRO, A.H. 1977 Self-diffusion of particles in shear flow of a suspension. *J. Fluid Mech.* **79**, 191–208.

VAN KAMPEN, N.G. 1992 *Stochastic processes in physics and chemistry*. Amsterdam, the Netherlands: Elsevier Science Publishers.

KRISHNAN, G.P. , BEIMFOHR, S. & LEIGHTON, D.T. 1996 Shear-induced radial segregation in bidisperse suspensions. *J. Fluid Mech.* **321**, 371–393.

LEIGHTON, D. & ACRIVOS, A. 1987a Measurement of shear-induced self-diffusion in concentrated suspensions of spheres. *J. Fluid Mech.* **177**, 109–131.

LEIGHTON, D. & ACRIVOS, A. 1987b The shear-induced migration of particles in concentrated suspensions. *J. Fluid Mech.* **181**, 415–439.

PHAN, S.E. & LEIGHTON, D.T. 1993 Measurement of the shear-induced tracer diffusivity in concentrated suspensions. *J. Fluid Mech.* **submitted**.

PHUNG, T. 1993 Behavior of concentrated colloidal suspensions by Stokesian Dynamics simulation. PhD thesis, Californian Institute of Technology.

PHUNG, T.N. , BRADY, J.F. & BOSSIS, G. 1996 Stokesian Dynamics simulation of Brownian suspensions. *J. Fluid Mech.* **313**, 181–207.

ZIDNEY, A.L. & COLTON, C.K. 1988 Augmented solute transport in the shear flow of a concentrated suspension. *Physicochem. Hydrodyn.* **10** (1), 77–96.

Chapter 3

Measuring Shear-Induced Self-Diffusion in a Counter-Rotating Geometry*

Abstract

The novel correlation method to measure shear-induced self-diffusion in concentrated suspensions of non-colloidal hard spheres which was developed in chapter 2 has been applied in a dedicated counter-rotating geometry. The counter-rotating nature of the set-up enables experiments over a wider range of well-controlled dimensionless time ($\dot{\gamma}\Delta t$ in the range 0.03-3.5, compared to 0.05-0.6 in previous experiments; here $\dot{\gamma}$ denotes the shear rate and Δt the correlation time). The accessible range of timescales made it possible to study the nature of the particle motion in a more detailed way. The wide radius geometry provides a well-defined flow field and was designed such that there is optical access from different directions. As a result, shear-induced self-diffusion coefficients could be determined as a function of particle volume fraction ϕ (0.20-0.50) in both the vorticity and velocity gradient direction. A transition could be observed to occur for $\dot{\gamma}\Delta t$ of $O(1)$, above which the particle motion is diffusive. The corresponding self-diffusion coefficients do not increase monotonically with particle volume fraction, as has been suggested by numerical calculations and the theoretical model of Brady & Morris (1997). After an exponential growth up to $\phi = 0.35$, the diffusion coefficients level off. The experiments even suggest the existence of a maximum around $\phi = 0.40$. The results are in good agreement with the experimental data of Phan & Leighton (1993), although their measurements were performed for much larger values of the dimensionless time $\dot{\gamma}\Delta t$.

*This chapter has been submitted to *Phys. Rev. E* as "Measuring Shear-Induced Self-Diffusion in a Counter-Rotating Geometry" by V. Breedveld, D. van den Ende, R.J.J. Jongschaap and J. Mellema (2000)'

3.1 Introduction

Shear-induced diffusion of non-colloidal particles is of great importance for understanding the transport processes in concentrated suspensions under flow and has therefore attracted a lot of attention (Davis, 1996).

The nature of the phenomenon is different from the more familiar diffusion concepts of Brownian diffusion in colloidal suspensions, which is caused by thermal fluctuations, and turbulent diffusion, driven by inertial effects. Shear-induced diffusion is the result of hydrodynamic interactions between suspended particles. In principle, this is a deterministic process. Due to the complex nature of the hydrodynamics, however, it can be described as a diffusion process. Shear-induced diffusion has been studied on two different levels: self-diffusion of individual particles and the collective process of gradient diffusion, which is studied by the net migration of particles on the macroscopic level (Acrivos, 1995). In this paper we address self-diffusion. By studying the results of hydrodynamic interactions on the particle level, we want to acquire information about the microscopic processes behind shear-induced diffusion.

Only very few experimental studies on shear-induced self-diffusion have been reported up to now (Eckstein *et al.*, 1977; Leighton & Acrivos, 1987a; Phan & Leighton, 1993). These measurements have all been performed by means of the same technique: a Couette cell is loaded with a concentrated suspension of non-colloidal particles, to which a tagged tracer particle is added and after each full rotation in the Couette cell, the passage time of the tracer particle is detected. Fluctuations in the tracer position and its revolution time can be related to shear-induced self-diffusion coefficients.

The major disadvantage of the technique is the fact that observations are only possible after full revolutions in the Couette cell. Consequently, the effect can only be studied on relatively long times $\dot{\gamma}\Delta t \sim O(10)$ (the process is fully hydrodynamically driven so that the strain $\dot{\gamma}\Delta t$ is the appropriate dimensionless time, where $\dot{\gamma}$ denotes the shear rate and Δt the passage time). Moreover, the values of $\dot{\gamma}\Delta t$ cannot be controlled externally, as is desirable when collecting detailed information about the nature of the particle displacements. The revolution time of the tracer particles in the Couette cell depends on their location at the start of the rotation and on the diffusive motion during the revolution: a particle close to the rotating outer wall of the Couette cell moves considerably faster than a tracer particle at the stagnant inner wall.

To overcome the problem of ill-controlled strain values $\dot{\gamma}\Delta t$ we have recently developed a novel correlation method and applied it successfully in a Couette cell with rotating inner cylinder (chapter 2). The set-up enabled accurate measurements over a controlled strain range from $\dot{\gamma}\Delta t = 0.05$ to circa 0.60.

In this paper, new results are presented, which have been obtained with the same technique, but in a more sophisticated counter-rotating geometry. The new set-up dramatically enlarges the experimentally accessible range of $\dot{\gamma}\Delta t$ (now 0.03 - 3.5),

bridging the gap between our previous experimental results of chapter 2 and the literature data. In the next section the basic equations of the correlation technique are briefly presented. A description of the apparatus and materials follows in section 3.3. We present and discuss results in section 3.4 and finally conclusions are drawn.

3.2 Correlation technique

This section contains a brief review of the basic concepts of the novel correlation technique. For a detailed mathematical description we refer to chapter 2.

The experimental technique is based on spatial correlation of a sequence of video images of the sheared suspension. The refractive index of the majority of particles is matched to the suspending fluid. Only a small fraction of colored tracer particles is used, so that even concentrated suspensions (20-50% volume fraction of particles) are optically accessible and images can be taken with a digital CCD camera at a fixed position in the geometry. Due to the refractive index matching in these images only the tracer particles show up and two consecutive images appear like the pictures in figure 3.1. The macroscopic flow field is drawn on the left. In accordance with common conventions, x denotes the velocity direction, y the velocity gradient direction and z the vorticity direction.

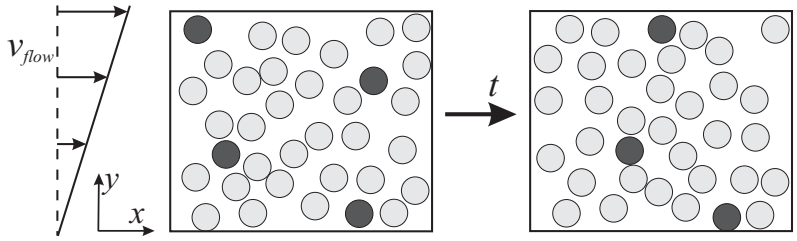

Figure 3.1: Images of tracer particles in concentrated suspension.

The positions of tracer particles in the images can be determined with state-of-the-art image analysis software. Subsequently, the positions of the tracer particles in the second image are correlated with the positions of the tracers in the first image by calculating the displacement vectors $(\Delta x, \Delta y)$.

Figure 3.2 shows the set of correlation vectors for the image pair of figure 3.1. At this point it is important to note that only the auto-correlation vectors (thick lines) contain information about self-diffusion, since they represent displacements of individual particles. The cross-correlation (dashed) vectors have no contribution to self-diffusion and only comprise information about the spatial distribution of tracer particles over the window of observation. The main problem is to discriminate between auto- and cross-correlation vectors with the objective to eliminate the cross-

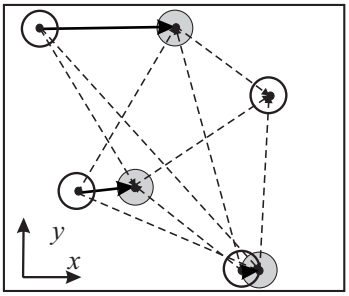

Figure 3.2: Correlation vectors $(\Delta x, \Delta y)$ for the images of figure 3.1.

correlation contributions. As described in chapter 2 this can be achieved statistically by determining the correlation vectors for a large ensemble of image pairs (at constant time interval Δt) and collecting all vectors in a histogram. A characteristic example is given in figure 3.3, representing data from an experiment in our counter-rotating geometry. The camera is looking along the velocity gradient (y) axis, so that the plane of view is the x-z-plane. Projections along the axes of the 3D-plot are included to accentuate the shape of the peak.

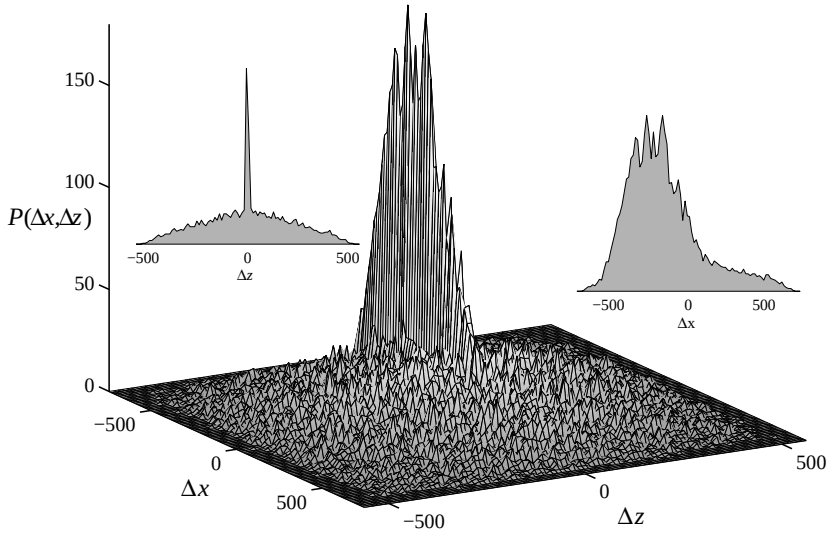

Figure 3.3: Histogram of correlation vectors $(\Delta x, \Delta z)$ for an ensemble of 8000 images ($\dot{\gamma}\Delta t = 0.72$ and $\phi = 0.30$); the units of the displacement axes (Δx and Δz) are pixels and the vertical axis represents the probability P in arbitrary (non-normalized) units. The contours of the projections along both axes are shown as well.

The peak in figure 3.3 consists of all auto-correlation vectors (thick lines in figure 3.2) which are relevant to this study, while the noisy background is due to the cross-correlation vectors (dashed). In other words, the peak contains the desired information about the motion of tracer particles. In particular its position represents the *average* displacement of tracers during the correlation time step Δt. This property is used in Particle Image Velocimetry (PIV), a technique which is nowadays frequently employed in experimental fluid dynamics to measure the velocity profiles of complicated flow fields (see e.g. Westerweel, 1993; Adrian, 1991). In addition to this well-known feature, the width of the correlation peak is a measure for the size of *fluctuations* in the particle displacements during time step Δt, which are the signature of diffusion on the particle level. Hence the width of the correlation peak is the quantity of interest for studying shear-induced self-diffusion. This idea forms the basis of our correlation technique

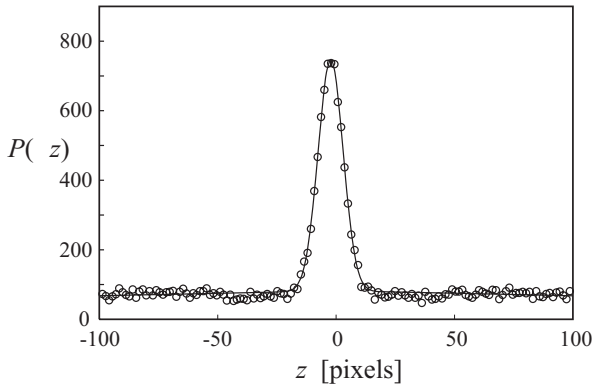

Figure 3.4: Reduced histogram of figure 3.3, revealing the Gaussian nature of the particle displacements in the vorticity direction (Δz) for an ensemble of 8000 images ($\dot{\gamma}\Delta t = 0.72$ and $\phi = 0.30$); the curve shows the non-linear fit of the data with eq. 3.1; units of the displacement axis (Δz) are pixels (particle radius $a = 31$pixels) and the vertical axis represents the probability P in arbitrary (non-normalized) units.

As emphasized by the contours of the projections in figure 3.3, the peak width is strongly amplified in the Δx-direction. This is caused by the convective shear flow, because tracer particles on different stream lines experience different Δx displacements in the shear flow. Such a convective contribution does not exist in the vorticity (z) direction, where particle motion is purely the result of fluctuations. Neglecting the displacements in the Δx-direction, which are obscured by the convection, we can obtain accurate information about the Δz-fluctuations by summing the data along the Δx-axis. Such a summation procedure results in the histogram of figure 3.4 which represents the probability of encountering a certain Δz value in the image ensemble. It was shown in chapter 2 that the peak in figure 3.4 should have a Gaussian shape

in the Δz-direction, if the particle fluctuations behave diffusively (see equations 2.15 and 2.20):

$$P(\Delta z) = \left(1 - \left|\frac{\Delta z}{H}\right|\right) \cdot \left\{C + B \cdot \exp\left(-\frac{\Delta z^2}{2\,\sigma_z^2}\right)\right\} \tag{3.1}$$

with H the size of the image in the z-direction and

$$\sigma_z^2 = 2\,D_{zz}\,\Delta t \tag{3.2}$$

D_{zz} being the diffusion coefficient in the vorticity direction. B and C both are functions that depend on the time step Δt and on experimental parameters like image size, depth of focus, tracer concentration and particle detection efficiency of the image analysis procedure. For fixed experimental conditions, B has a constant value. C on the other hand represents the cross-correlation contribution to the histogram and is a function of the distribution of the tracer particles. To be more specific, C depends on $P_2(\Delta\mathbf{x};\Delta t)$, the chance of finding a particle at a certain position $\mathbf{x}+\Delta\mathbf{x}$, while *another* particle resided at any possible position $\mathbf{x}$ a time Δt earlier. For $\Delta t = 0$, this function matches the well-known pair distribution function $g(\mathbf{r})$.

Because in general $g(\mathbf{r})$ can be expected to be non-uniform –particularly at high volume fractions where particles are not necessarily distributed randomly– the functional shape of $P_2(\Delta\mathbf{x};\Delta t)$ is *a priori* unknown. Therefore the exact theoretical shape of the curve in figure 3.4 is also uncertain.

For the non-counter-rotating Couette set-up this theoretical complication could be evaded. It was shown in chapter 2 that symmetry considerations are sufficient to eliminate the unknown function C. The key feature in the derivation is the fact that, because of the convective shear flow, the auto-correlation peak was always fully located in the half-plane $\Delta x > 0$ of figure 3.3. Therefore the half-plane for $\Delta x < 0$ only contained cross-correlation contributions, which could be subtracted from the points with $\Delta x > 0$, using the flow symmetry. In this case equation 3.1 simplifies to

$$P(\Delta z) = B \cdot \left(1 - \left|\frac{\Delta z}{H}\right|\right) \cdot \exp\left(-\frac{\Delta z^2}{2\,\sigma_z^2}\right) \tag{3.3}$$

When making use of the advantage of counter-rotating flow, however, the plane of focus is located around the plane of zero velocity. Within the depth of focus of the camera optics, some of the tracer particles will experience flow displacements to the left and others will travel to the right. Consequently, the peak of figure 3.3 is located around the origin and symmetry arguments can no longer be used to subtract the cross-correlation contributions, since it would eliminate (part of) the desired auto-correlation peak as well. In this case, a more detailed analysis of the role of $P_2(\Delta\mathbf{x};\Delta t)$ is required.

The influence of $P_2(\Delta\mathbf{x};\Delta t)$ on the shape of function C in equation 3.1 is weakened by an averaging integral (equation 2.15) as result of the finite depth of focus of the camera optics. The two dimensional image is in fact the projection of a three dimensional volume element, its size being defined by the depth of focus. Thus any possible spatial structure in the particle distribution function P_2 is smeared out by the projection.

We have used a robust experimental analysis to clarify the effect of volume averaging on the observed shape of the cross-correlation contribution. To this purpose the functional shape of C was determined for $\Delta t = 0$, i.e. when $P_2(\Delta\mathbf{x};\Delta t)$ matches $g(\Delta\mathbf{x})$. The cross-correlation vectors between different particles in every image were calculated and the collected data were plotted in histograms like figure 3.3 and 3.4. These histograms showed that within experimental errors no spatial structure could be detected. The distribution appeared to be random, most probably due to the volume averaging integral that represents projection. If no structure can be found for $g(\Delta\mathbf{x})$ at $\Delta t = 0$, it is to be expected that this will be even less likely for $P_2(\Delta\mathbf{x};\Delta t)$ at finite values of Δt.

Consequently, in our counter-rotating experiments we could safely apply the assumption of C being constant, so that equation 3.1 could be used directly to fit the experimental data of histograms like figure 3.4 and determine the width of the autocorrelation peak.

The single relevant timescale of the experiment is $\dot\gamma\Delta t$: the process stops when the flow is stopped and Brownian motion is negligible. Furthermore the only important length scale is the particle radius a. Thus, dimensional analysis requires that σ_z in equation 3.2 obeys the following scaling (Eckstein *et al.*, 1977; Leighton & Acrivos, 1987a):

$$\frac{\sigma_z^2}{a^2} = 2\,\hat D_{zz}\,\dot\gamma\Delta t \tag{3.4}$$

where $\hat D_{zz}$ is the dimensionless diffusion coefficient, scaled by $\dot\gamma a^2$. $\hat D_{zz}$ can be expected to depend on the particle volume fraction ϕ. These simple scaling arguments have been confirmed by several experimental studies (chapter 2, Phan & Leighton (1993); Leighton & Acrivos (1987a)). One of the most remarkable differences between shear-induced diffusion and Brownian diffusion is the fact that the former is independent of the viscosity of the suspending fluid.

The correlation technique can be used to investigate the nature of the particle motion over a range of $\dot\gamma\Delta t$ values. In regions where the scaling of equation 3.4 applies, the motion is diffusive and the dimensionless diffusion coefficient $\hat D_{zz}$ can be calculated directly from the slope in a σ^2/a^2-$\dot\gamma\Delta t$-graph. This is a powerful feature of the method, since the self-diffusion can thus be investigated on different timescales

as opposed to the technique employed by Leighton & Acrivos (1987a) and Phan & Leighton (1993) where single points after relatively long times were used to derive a diffusion coefficient without actually checking the diffusive scaling.

When the system is viewed from the vorticity (z) direction, similar graphs are obtained and relations analogous to equations 3.3 and 3.4 can be derived for the width of the auto-correlation peak in the Δy-direction, σ_y, and accordingly $\hat{D}_{yy}$ can be measured.

3.3 Experimental work

The technique described in the preceding section has been successfully applied and tested in a Couette geometry in chapter 2. Due to geometrical restrictions, the range of $\dot{\gamma}\Delta t$ in those experiments was limited from 0.05 to 0.6. For larger strain values, the shear flow moved too many particles out of the viewing window for obtaining reliable statistical information. In order to circumvent this problem and to increase the experimentally accessible range of $\dot{\gamma}\Delta t$, a counter-rotating geometry was built, in which the images could be taken close to the plane of zero velocity. In this was particles were kept within the field of view for much longer times.

3.3.1 Apparatus

Our experimental set-up was designed with a cone-plate geometry, since it is characterized by a constant shear rate even if the fluid is non-Newtonian. The value of the important scaling parameter $\dot{\gamma}$ could thus be controlled more accurately and collective migration as a result of gradient diffusion could be neglected. In literature, the importance of gradient diffusion in cone-plate and plate-plate geometries has been subject of debate for some time (e.g. Chapman & Leighton, 1991; Chow *et al.*, 1994; Krishnan *et al.*, 1996). Conclusive evidence was not available at the moment of designing our apparatus. Presently, the argument seems to develop in favour of the existence of outward particle migration in cone-plate flow due to curvature effects (Krishnan *et al.*, 1996; Morris & Boulay, 1999). However, significant particle migration could not be observed in our cone-plate geometry, possibly due to the small curvature of the wide radius design.

Figure 3.5 shows a sketch of the apparatus, which is an adapted version of the rheoscope developed by de Haas *et al.* (1998) to study the deformation of vesicles in shear flow. The flow cell units were connected to independent drive units (step motors with RS100 control, designed and built by Eltromat) via precision fittings and play-free Oldham couplings. The units were further supported by aerostatic bearings so that extremely high accuracy could be achieved in the alignment of the flow cell.

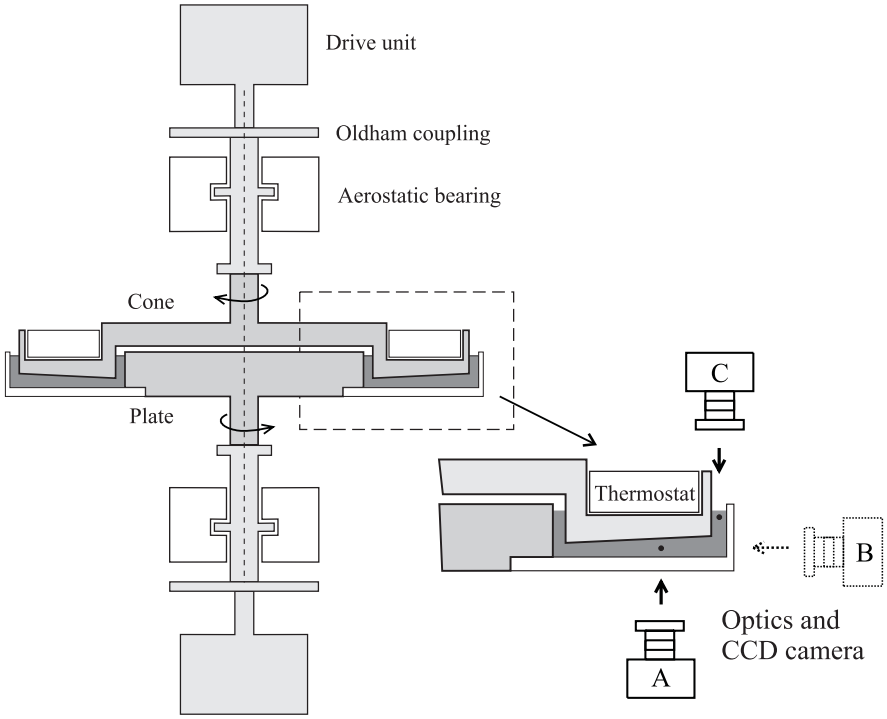

Figure 3.5: Design of counter-rotating cone-plate geometry.

In our experiments we made use of a steel cone and a glass plate for optical access from different directions. The cone-plate configuration (with the extrapolated cone intersecting the plate at the rotational axis) was only present over a limited range of the radius, from 8.5 to 11.5 cm. This geometry was chosen in order to restrict the sample volume, while maintaining a small cone angle $\theta = 2^\circ$ and a sufficiently large gap size to minimize wall effects for non-colloidal particles of $O(100\ \mu\text{m})$ (3.0 mm at the inner edge and 4.0 mm at the outer edge of the truncated cone). The cone and plate were both polished with extreme care, so that vertical variations during a full rotation were only about 5 μm for both cone and plate. The temperature was controlled with a thermostat unit, which was brought into contact with the rotating steel cone through a thin water layer.

Numerical calculations were performed to check the influence of the cone edges on the steady state flow field in the tangential direction. The calculations led to an adaptation in the design: the inner section of the cone unit was made flat in order to minimize the influence of the sharp inner edge. It was shown that with this lay out the flow was not significantly affected for both Newtonian and power-law fluids. The shear rate $\dot{\gamma}$ under the center of the cone deviated no more than a few tenths of a percent from the desired cone-plate value.

The original idea was to have visual access to an observation window under the cone from two directions, so that all components of the diffusion tensor could be measured under exactly the same flow conditions. However, it turned out that measurements from position B in figure 3.5 were impossible. In spite of extensive attempts to optimize the refractive index matching of our suspensions, the optical penetration depth could not be increased to more than 3 mm, while about 7 mm would have been necessary for reliable measurements from position B (see also section 3.3.2). An alternative approach was therefore taken to measure diffusion in the $x-y-$plane: the cone was lowered up towards the glass plate and the outer Couette gap between cone and plate element was used for experiments, with camera position C. The wide-radius Couette gap has inner and outer radii $R_i = 117.3$ mm and $R_o = 121.6$ mm. The height of the fluid in the gap was chosen to be 8 mm, so that the influence of the cone-plate section on the velocity profile minimized, which was confirmed by numerical calculations. The mechanical precision of the flow elements was very high in the outer gap as well, the variations in gap width being no larger than 10 μm during a full rotation. In essence we have used the same geometry for the measurements of $\hat{D}_{yy}$ as described in chapter 2, but the counter-rotating character of the apparatus dramatically increases the maximum correlation time.

The conversion from rotational speeds to shear rates is based on standard equa-

tions for cone-plate and Couette rheometry:

$$\dot{\gamma}_A = \frac{\Omega}{\theta} = 3.0 \cdot \Omega \tag{3.5}$$

$$\dot{\gamma}_C = \frac{2\pi}{60} \frac{R_o^2 + R_i^2}{R_o^2 - R_i^2} \Omega = 2.89 \cdot \Omega \tag{3.6}$$

the indices indicating the viewing position and Ω [rpm] being the relative rotational speed of cone and plate. For the Couette system, equation 3.6 represents the shear rate $\dot{\gamma}_C$ at the position in the gap where the tangential velocity equals zero, since the images are collected at this location:

$$r = \left(\frac{2 R_o^2 R_i^2}{R_o^2 + R_i^2} \right)^{\frac{1}{2}} \tag{3.7}$$

The drive units are capable of producing shear rates ranging from $3 \cdot 10^{-3}$ to 30 s^{-1}, but all experiments were carried out for $\dot{\gamma}$ between 0.1 and 2.0 s^{-1}.

Since both the initial positions and displacements of the tracer particles are available from image analysis and correlation procedures, for the Couette geometry (observation window in the $x-y-$plane) it is possible to determine the velocity field of the macroscopic shear flow experimentally from the data. The measured values were higher than the Couette predictions of equation 3.6 for Newtonian fluids. For the study presented in this paper, we have used the experimental values for the shear rate, since they accurately represent the actual shear rate at the observation location in the gap. The procedure to measure the velocity field is explained and discussed in detail in chapter 5.

3.3.2 Materials

Experiments were performed with suspensions of PMMA (polymethylmethacrylate) particles (produced by ICI, class 4F) dispersed in a fluid consisting of demineralized water (9.2 weight-%), zinc-II-chloride (13.4%) and Triton X-100 (77.4%), following the recipe of Krishnan *et al.* (1996). The fluid was Newtonian with a viscosity of 3.4 Pa s at 23°C and matched both the density (1.172 kg/l) and refractive index ($n_D^{25} = 1.491$) of the particles. In our attempts to measure from camera position B (fig. 3.5), we have tried to improve the refractive index matching by changing the fluid composition. However, we never obtained penetration depths larger than 3 mm. Most likely this is due to small variations in refractive index between different particles or even within particles. We have noticed that changes in the fourth decimal of the refractive index are sufficient to cause significant blurring effects of the video images.

The particles were sieved repeatedly to obtain fairly monodisperse particles with a diameter of $90 \pm 15\,\mu$m. Spheres with air bubbles were removed by means of density segregation. The particles were suspended in a water-glycerol mixture of a slightly lower density and the creaming fraction of light particles was removed. A small fraction of the particles, typically 0.2 volume-% of the suspension, was coloured with liquid fabric dye (RIT) to serve as tracer particles in the transparent suspension; no changes could be found in their density after colouring. The suspensions were homogenized by gently tumbling the components overnight at low rotational speed. Then they were set to rest to let the small quantity of air bubbles disappear. Measurements were performed for particle volume fractions ϕ of 20-50%.

3.3.3 Image acquisition and analysis

As shown in figure 3.5 the transparent plate provided optical access to the suspension volume from position A, which was used to measure $\hat{D}_{zz}$. From position C we entered the suspension through the free surface in order to find $\hat{D}_{yy}$. A digital CCD camera (JAI M-10, 768 by 582 pixels, 25 images per second) was mounted with optics to obtain a view window of 1.10 by 0.83 mm (determined by calibration) and connected to a PC. Illumination was arranged with a fiber optic halogen illuminator (Schott KL1500) that provided optimal contrast in the images.

The video images were stored directly on the PC through a frame grabber (Matrox Pulsar) that was operated using a special software tool (Hispa), which enabled accurate and controlled image acquisition of series of up to 200 images at discrete time intervals Δt of 40 ms (video rate) and multiples thereof. Since Hispa offered the possibility of automatical repetition of the acquisition procedure, the total number of images in a run was limited only by the hardware storage capacity of the computer system. In our case, runs were made of up to 8000 images.

All images were then analyzed with a commercial software package for image analysis (Optimas). Basic analysis tools provided the means to identify dark objects and extract information about their properties. These properties –size, sphericity and blackness– were compared to pre-set criteria in order to decide whether the object was a tracer particle. If so, its position (gray value weighted center of mass) was stored in a data file for correlation purposes. The accuracy of the image analysis procedures was checked by changing the settings of the different analysis steps and monitoring the result. The error in the particle positions was estimated to be circa 0.2 pixels under our experimental conditions. The sub-pixel accuracy is the result of averaging over any pixels.

3.4 Results and discussion

The data files with particle positions were used as input for the correlation procedure. As described in section 3.2 (see also chapter 2 for detailed description) the correlation vectors were calculated for all possible image combinations and grouped according to the correlation time $\dot{\gamma}\Delta t$ between images.

3.4.1 Correlation results

The resulting sets of correlation vectors for all values of $\dot{\gamma}\Delta t$ were collected in histograms (e.g. figure 3.4), which were fitted with a non-linear least square method to equation 3.1. The peak width σ_z obtained from the fitting was plotted against the strain $\dot{\gamma}\Delta t$ in a $\sigma_z^2/a^2 - \dot{\gamma}\Delta t-$graph in order to check the validity of scaling equation 3.4.

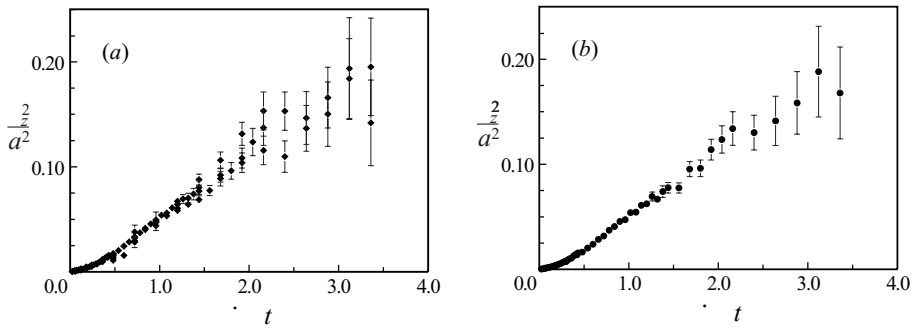

Figure 3.6: Scaling of the average squared displacement of the particles σ_z^2/a^2 with dimensionless time $\dot{\gamma}\Delta t$ for $\phi = 0.30$; *(a)* contains the raw fit data and *(b)* the results of the weighted average.

At each particle volume fraction, this procedure was repeated for different values of $\dot{\gamma}$ and Δt, thus covering the entire range of $\dot{\gamma}\Delta t$ between 0.03 and 3.5. Figure 3.6*a* shows the entire collection of data points for $\phi = 0.30$. The error bars of the individual points represent the errors of the non-linear fit. These statistical error estimates represent the scatter between different experimental runs very well. Since for most $\dot{\gamma}\Delta t-$values several data points were collected at different shear rates $\dot{\gamma}$, standard statistical manipulation of the data was appropriate. Figure 3.6*b* shows the resulting weighted averages (with $1/\text{error}^2$ as weight factor) and their associated standard deviations for $\phi = 0.30$.

The figure displays a number of interesting features. It distinctly shows that for large values of $\dot{\gamma}\Delta t$ the statistical information becomes less accurate, since less and less tracer particles remain within the field of view during the entire correlation time. Although the counter-rotating design strongly increased the range of accessi-

ble timescales and theoretically enables experiments at very large strain values, the $\dot{\gamma}\Delta t$ – range was in practice limited by the number of images that could be stored and analyzed on the computer. In our case, the upper limit of $\dot{\gamma}\Delta t$ was circa 3.5. Increased hardware storage capacity and image analysis speed would extend the range of accessible strain values and decrease the error bars.

Figure 3.6*b* also shows linear scaling over most of the range, which is the fingerprint of diffusion (see equation 3.4). In this regime, roughly for $\dot{\gamma}\Delta t > 0.7$, the data can be fitted linearly and the diffusion coefficient can be calculated directly from the slope of the fitted line, the dimensionless coefficient $\hat{D}_{zz}$ being half the slope. Figure 3.7 shows the experimental data in the vorticity direction and fitted line for various particle volume fractions.

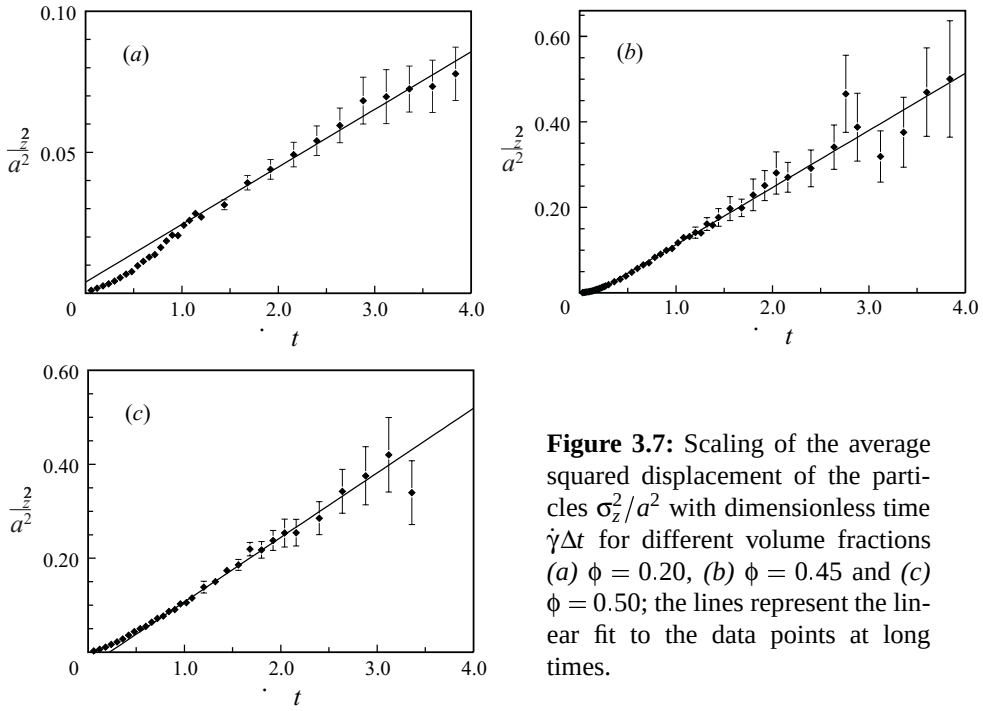

Figure 3.7: Scaling of the average squared displacement of the particles σ_z^2/a^2 with dimensionless time $\dot{\gamma}\Delta t$ for different volume fractions *(a)* $\phi = 0.20$, *(b)* $\phi = 0.45$ and *(c)* $\phi = 0.50$; the lines represent the linear fit to the data points at long times.

Measurements in the velocity gradient (y) direction were slightly more complicated, because the images had to be taken through the free surface in the Couette gap. In order to eliminate surface effects, the camera optics was focused on a location 1.5-2.0 mm below the surface. With a particle diameter of 100 μm this should be sufficiently deep. In some experimental runs we deliberately focused on the particles at the suspension surface to investigate the surface effects and a significantly larger diffusion coefficient was found in those runs. In addition to the surface diffusion, measurements at the highest volume fractions are complicated by surface

"roughening" as particles are pushed out of the suspension by strong hydrodynamic interaction forces. Thus the image quality deteriorates and the average number of detected tracer particles per image decreases, so that statistical information becomes less accurate. Nevertheless we have been able to obtain reliable results for diffusion in the $y-$direction. In figure 3.8 the scaling of the average squared displacement σ_y^2/a^2 is presented for different volume fractions together with the linear fit to the diffusive regime at long times. In comparison to figure 3.7, the onset of diffusion in the $y-$direction occurs for larger values of $\dot{\gamma}\Delta t$. The range of the linear fits has been adapted accordingly.

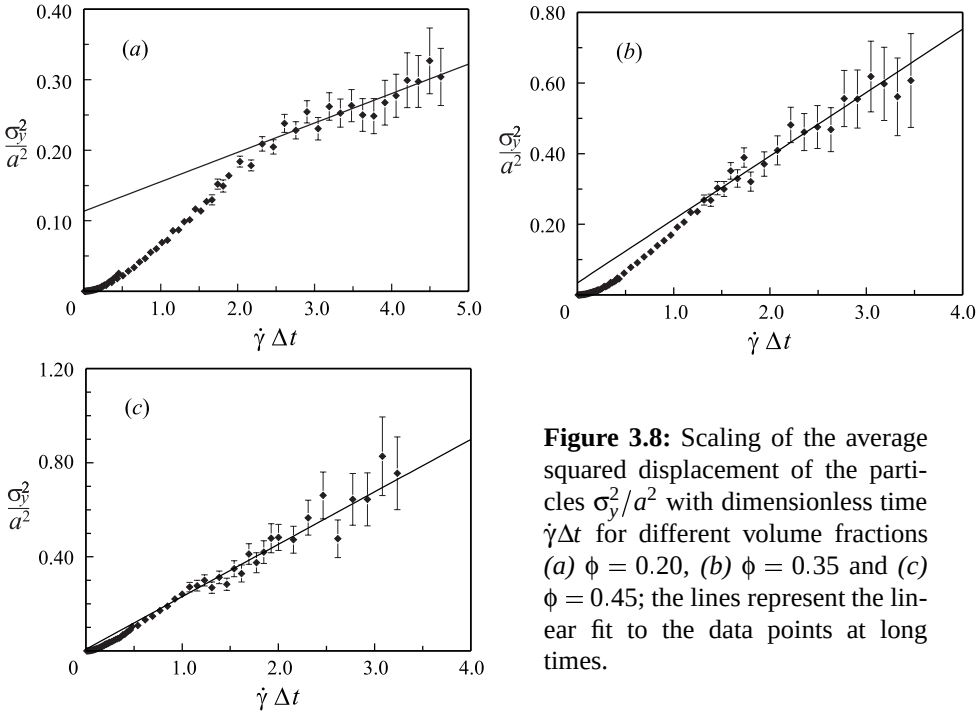

Figure 3.8: Scaling of the average squared displacement of the particles σ_y^2/a^2 with dimensionless time $\dot{\gamma}\Delta t$ for different volume fractions *(a)* $\phi = 0.20$, *(b)* $\phi = 0.35$ and *(c)* $\phi = 0.45$; the lines represent the linear fit to the data points at long times.

3.4.2 Diffusion coefficients

Within experimental errors the diffusion coefficient (slopes in figure 3.7 and 3.8) is constant down to $\dot{\gamma}\Delta t \sim 1$, which implies that the concept of shear-induced self-diffusion is applicable over a large range of timescales. In particular the lower boundary of validity is rather surprising. Within the framework of the collision model of Leighton & Acrivos (1987a) it was generally believed that diffusive behaviour could only be attained on experimental times $\dot{\gamma}\Delta t \gg 1$, i.e. for times large compared to the assumed collision time in simple shear flow, so that a particle has experienced several interactions with its neighbours. The early onset of diffusion is the result of

ensemble averaging. As soon as all particles have experienced a single displacement step, the correlations with previous moments in time are lost, since the direction of the displacement is random due to the random starting conditions of each interaction. As soon as the correlation has vanished, diffusive motion can be observed, although individual tracer particles have not yet undergone multiple displacements. The fact that characteristic time of the diffusion is of the order $\dot{\gamma}\Delta t = 1$ does therefore not automatically imply that mechanistic (collision based) models are inadequate.

For small values of $\dot{\gamma}\Delta t$, the curves in figures 3.7 and 3.8 are non-linear, so that diffusive motion cannot be assumed in this regime. Our previous experiments were carried out for $\dot{\gamma}\Delta t$ varying from 0.05 to 0.6, where in the current experiments linearity has not been reached. Within experimental accuracy of the former measurements it seemed appropriate to fit the data linearly, thus obtaining values for the diffusion coefficients. The present study suggest that in this way we have underestimated shear-induced self-diffusion. This is illustrated by figure 3.9. In the left graph, the data for $\phi = 0.45$ of figure 3.7*c* are fitted linearly over two different ranges of $\dot{\gamma}\Delta t$. The dotted curve represents the linear fit for $\dot{\gamma}\Delta t$ between 0.1 to 0.6, consistent with the procedures in chapter 2, the solid curve depicts the linear fit only over long times, $\dot{\gamma}\Delta t > 0.7$, analogous to figure 3.7.

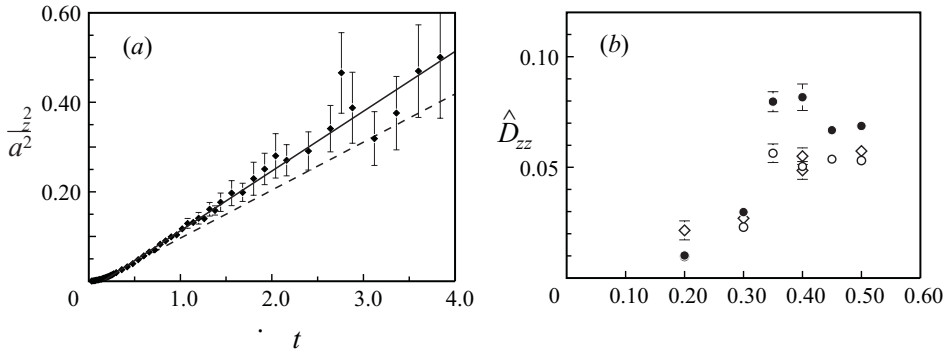

Figure 3.9: Comparison of the data of chapter 2 to the results of the current study. *(a)* shows two linear fits for $\phi = 0.45$, dashed line (- - -) for $\dot{\gamma}\Delta t = 0.10 - 0.60$, solid line (—) for $\dot{\gamma}\Delta t > 0.7$. *(b)* contains the associated diffusion coefficients in the vorticity direction as a function of ϕ; (●) and (○) represent data from this study, of respectively the full and limited fit, (◊) denote earlier results presented in chapter 2.

In figure 3.9*b* the short-time linear fits of our current data in the $z-$direction are compared to the diffusion coefficients reported in chapter 2. Leaving out the data for 20%, which were not very reliable, the figure shows that the previous study indeed underestimated the diffusion coefficient by up to 30% at the highest volume fractions. At the time of that study, we noticed deviations from the literature data of

Phan & Leighton (1993), but the differences were not very large in comparison with the significant experimental errors and the scatter in literature data. With our new results in mind, however, we must conclude that the accessible range of timescales in the Couette experiments of chapter 2 was insufficient to capture the onset of shear-induced self-diffusion.

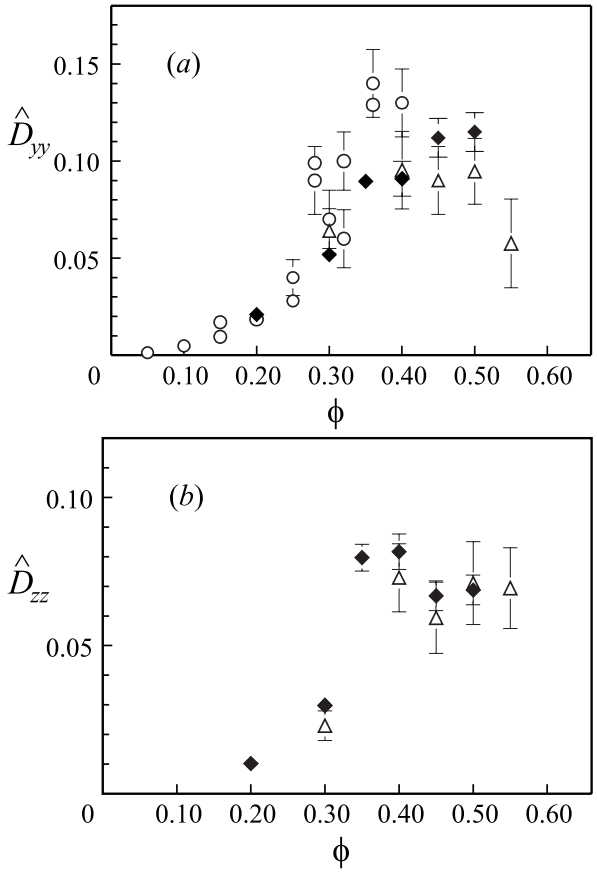

Figure 3.10: Coefficients of shear-induced self-diffusion as measured by various researchers in *(a)* the velocity gradient $\hat{D}_{yy}$ and *(b)* the vorticity $\hat{D}_{zz}$ direction as a function of particle volume fraction ϕ; (△) represent data of Phan & Leighton (1993), (○) of Leighton & Acrivos (1987a) and (⧫) were measured in this study.

All available experimental data for shear-induced self-diffusion as a function of volume fraction ϕ are combined in figure 3.10. The results of chapter 2 were left out for the reason explained above. Even if the experimental errors are significant, we can safely say that there is fair agreement between the results of the various experimental methods with different systems. In particular our results are in very good agreement

with the most recent data of other researchers, i.e. Phan & Leighton (1993). The results of Leighton & Acrivos (1987a) deviate somewhat from the other two studies, but in that study the authors had problems with crystallization of the suspending fluid and this could have affected their results.

The characteristic timescale $\dot{\gamma}\Delta t \sim 1$ above which we determine diffusion coefficients –and which was also used by Foss & Brady (1999)– has recently been questioned by Marchioro & Acrivos (2000). In their Stokesian Dynamics simulations these authors found that linear (diffusive) scaling could only be observed for $\dot{\gamma}\Delta t > 5$ in the reported cases. Unfortunately, even in our counter-rotating set-up we are unable to check this claim experimentally, because too many tracer particles leave the observation window at long times. However, we can compare our data to the results of Phan & Leighton (1993), who performed their measurements over even longer times ($\dot{\gamma}\Delta t \gg 10$, although exact numbers cannot be reconstructed) and calculated the diffusion coefficient by assuming a straight line through the origin in graphs like our figure 3.7. On these long times the offset can indeed be neglected without problem. The agreement between our data and the long-time experiments is very suggestive: it is hard to understand that the slope of our linear fit could be incorrect, while extrapolation of this line accurately intersects the data points of Phan & Leighton (1993).

Figure 3.10 reveals some intriguing trends. First of all the dimensionless diffusion coefficient in the velocity gradient direction ($\hat{D}_{yy}$) is about a factor 1.5 larger than in the vorticity direction ($\hat{D}_{zz}$). This is in agreement with the theoretical results of Brady & Morris (1997), who predict shear-induced self-diffusion coefficients in concentrated suspensions by analyzing the microstructure of the suspension, i.e. the contact values of the pair distribution function $g(\mathbf{r})$. On the other hand the experimentally found anisotropy $\hat{D}_{yy}/\hat{D}_{zz}$ for concentrated suspensions is significantly smaller than the results of theoretical models for dilute suspensions that attribute shear-induced diffusion to the symmetry breaking of particle collisions due to particle roughness (Da Cunha & Hinch, 1996) or to the presence of a third particle (Wang *et al.*, 1996). Both models predict the anisotropy to be circa 10 and the discrepancy implies that the behaviour of concentrated suspensions deviates strongly from the dilute limit.

Secondly, in figure 3.10 there is clear experimental evidence that both diffusion coefficients do not grow monotonically with volume fraction, as has been suggested by the measurements of Leighton & Acrivos (1987a) and by the theoretical work of Brady & Morris (1997). Up to volume fractions of circa 0.35 the diffusion coefficients increase rapidly. Above this volume fraction they level off and even exhibit a tendency to go down for the highest volume fractions of 0.5 and 0.55, although this final decrease can not be concluded beyond experimental doubt. The measured diffusion coefficient $\hat{D}_{yy}$ at 45% lies somewhat higher than the trend in our experiments

suggests and underlines the decrease in diffusivity at 50%.

In their theoretical study Brady & Morris (1997) have argued that shear-induced self-diffusion should scale as the product of the velocity fluctuations ($\dot{\gamma}a$) and the size of the displacements ($O(a)$). Since in their model the frequency of particle collisions is directly associated with the pair distribution function at contact, it should increase strongly with volume fraction, thus giving rise to growing self-diffusion coefficients as well. Our experimental results however reveal a different qualitative behavior. We have no explanation for this difference, but apparently one of the above scaling arguments is oversimplified. It could very well be that the contact value of the pair distribution function, $g(2)$, is insufficient to describe the hydrodynamic influence of the many particle problem for modeling shear-induced diffusion, although it has proven its usefulness in modeling suspension viscosities.

Stokesian Dynamics simulations (e.g. Yurkovetsky, 1998) have generally supported the theoretical ideas. However, recent numerical calculations of Foss & Brady (1999) and Marchioro & Acrivos (2000) have shown a tendency for $\hat{D}_{yy}$ to level off at high concentrations, even if it is hard to draw strong conclusions on basis of their work, especially since $\hat{D}_{zz}$ does not exhibit the same qualitative behaviour. The diffusion in the vorticity direction clearly increases with ϕ in both studies.

3.5 Conclusions

In combination with a counter-rotating flow geometry the correlation technique has proven to be a powerful method to study shear-induced self-diffusion of concentrated non-colloidal suspensions. Visual observation of tracer particle positions in a refractive index matched suspension at well-controlled time intervals enabled a detailed analysis of the particle motion. Statistical tools could be applied to accurately characterize this motion. The most important feature of the method is the fact that in the counter-rotating cone-plate geometry used in this study the dimensionless experimental time $\dot{\gamma}\Delta t$ could be varied from circa 0.03 to 3.5, so that different timescales could be probed. The upper boundary of the $\dot{\gamma}\Delta t$ range is only limited by computer capacity for image storage and analysis.

The onset of self-diffusion could be observed and the associated long-time diffusion coefficients were determined as a function of particle volume fraction. The dimensionless diffusion coefficients $\hat{D}_{yy}$ and $\hat{D}_{zz}$ were in good agreement with previous results of Leighton & Acrivos (1987a) and Phan & Leighton (1993) who employed a different technique based on the analysis of the motion of single tracer particles over very long times ($\dot{\gamma}\Delta t \sim O(10)$). The results significantly differed from our previous results in non-counter-rotating Couette flow (chapter 2),but these discrepancies could be fully attributed to the limited range of $\dot{\gamma}\Delta t$ in those experiments (0.05-0.60).

The onset of diffusion occurs at a dimensionless time $\dot{\gamma}\Delta t$ of $O(1)$, as could be

expected, since $1/\dot{\gamma}$ is the governing timescale in shear flow. The onset changes with particle volume fraction, shifting to shorter times at higher concentrations. In the velocity gradient direction, the diffusive regime is reached for larger strain values than in the vorticity direction. Recent numerical results (Marchioro & Acrivos, 2000) suggest that much longer times are needed to reach diffusive motion. Although we are unable to prove otherwise in our set-up, the agreement with the measurements of Phan & Leighton (1993) would be very peculiar if the regime of the linear fit in our experimental data is incorrect.

The measurements provide additional experimental evidence about the remarkable behaviour of the diffusion coefficients as a function of particle volume fraction ϕ. In contrast to recent theoretical predictions of Brady & Morris (1997) and numerical results of Foss & Brady (1999) and Marchioro & Acrivos (2000), experimental self-diffusion coefficients in the velocity gradient and vorticity direction, resp. $\hat{D}_{yy}$ and $\hat{D}_{zz}$, do not increase monotonically as a function of ϕ. Up to volume fractions of 35% the diffusion rises strongly and then it levels off and even shows the tendency to go down again above 45%.

Furthermore, the experimentally determined values of the diffusion coefficient in the velocity gradient direction ($\hat{D}_{yy}$) are significantly larger than in the vorticity direction ($\hat{D}_{zz}$), the anisotropy being circa a factor 1.5.

The research described in this paper was supported by the Foundation for Fundamental Research on Matter (FOM) in the Netherlands.

References

ACRIVOS, A. 1995 Shear-induced particle diffusion in concentrated suspensions of non-colloidal particles. *J. Rheol.* **39** (5), 813–826.

ADRIAN, R.J. 1991 Particle-imaging techniques for experimental fluid mechanics. *Ann. Rev. Fluid Mech.* **23**, 261–304.

BRADY, J.F. & MORRIS, J.F. 1997 Microstructure of strongly sheared suspensions and its impact on rheology and diffusion. *J. Fluid Mech.* **348**, 103–139.

CHAPMAN, B.K. & LEIGHTON, D.T. 1991 Dynamic viscous resuspension. *Int. J. Multiphase Flow* **17** (4), 469–483.

CHOW, A.W. , SINTON, S.W. , IWAMIYA, J.H. & STEPHENS, T.S. 1994 Shear-induced particle migration in Couette and parallel-plate viscometers: NMR imaging and stress-measurements. *Phys. Fluids* **6** (8), 2561–2576.

DA CUNHA, F.R. & HINCH, E.J. 1996 Shear-induced dispersion in a dilute suspension of rough spheres. *J. Fluid Mech.* **309**, 211–223.

DAVIS, R.H. 1996 Hydrodynamic diffusion of suspended particles: a symposium. *J. Fluid Mech.* **310**, 325–335.

ECKSTEIN, E.C. , BAILEY, D.G. & SHAPIRO, A.H. 1977 Self-diffusion of particles in shear flow of a suspension. *J. Fluid Mech.* **79**, 191–208.

FOSS, D.R. & BRADY, J.F. 1999 Self-diffusion in sheared suspensions by dynamic simulation. *J. Fluid Mech.* **401**, 243–274.

DE HAAS, K.H. , VAN DEN ENDE, D. , BLOM, C. , ALTENA, E.G. , BEUKEMA, G.J. & MELLEMA, J. 1998 A counter-rotating Couette apparatus to study deformation of a sub-millimeter sized particle in shear flow. *Rev. Sci. Instrum.* **69** (3), 1391–1397.

KRISHNAN, G.P. , BEIMFOHR, S. & LEIGHTON, D.T. 1996 Shear-induced radial segregation in bidisperse suspensions. *J. Fluid Mech.* **321**, 371–393.

LEIGHTON, D. & ACRIVOS, A. 1987a Measurement of shear-induced self-diffusion in concentrated suspensions of spheres. *J. Fluid Mech.* **177**, 109–131.

MARCHIORO, M. & ACRIVOS, A. 2000 Shear-induced particle diffusivities from numerical simulations. *J. Fluid Mech.* **submitted**.

MORRIS, J.F. & BOULAY, F. 1999 Curvilinear flows of noncolloidal suspensions: the role of normal stresses. *J. Rheol.* **43** (5), 1213–1237.

PHAN, S.E. & LEIGHTON, D.T. 1993 Measurement of the shear-induced tracer diffusivity in concentrated suspensions. *J. Fluid Mech.* **submitted**.

WANG, Y. , MAURI, R. & ACRIVOS, A. 1996 The transverse shear-induced liquid and particle tracer diffusivities of a dilute suspension of spheres undergoing a simple shear flow. *J. Fluid Mech.* **327**, 255–272.

WESTERWEEL, J. 1993 Digital particle image velocimetry. PhD thesis, Delft Technical University.

YURKOVETSKY, Y. 1998 I. Statistical mechanics of bubbly liquids; II. Behavior of sheared suspensions of non-Brownian particles. PhD thesis, Californian Institute of Technology.

Chapter 4

Self-Diffusion and Rheology: Timescales and Particle Displacements*

Abstract

The shear-induced diffusion and rheology of concentrated suspensions of non-colloidal hard sphere have been studied experimentally. Both properties are directly related to the particle configuration in the suspension and the combined results provide an interesting physical picture. The projection of the trajectories of individual particles on the vorticity(z)-velocity(x)-plane were determined through particle tracking. For a quantitative analysis of the particle displacements we measured the evolution of the ensemble averaged displacements as a function of time. Statistical analysis revealed two diffusion regimes. For large strain values ($\dot{\gamma}\Delta t > 1$) long-time self-diffusion was observed. The associated diffusion coefficient $\hat{D}_\infty$ is in excellent agreement with literature data on shear-induced self-diffusion. On very short times ($\dot{\gamma}\Delta t \ll 1$) a novel diffusive regime was discovered, characterized by a diffusion coefficient $\hat{D}_0$, which is significantly smaller than $\hat{D}_\infty$ and grows monotonically with ϕ. $\hat{D}_0$ is detected for timescales on which the particle configuration has not changed significantly and thus it must represent the fluctuating motion of particles inside the 'cage' formed by their nearest neighbours. Dynamic viscosity measurements in a controlled stress rheometer revealed that the viscoelastic response of the suspension is determined by the deformation as well. At small strain amplitudes $\gamma_0 < 1$, the response is linear and the dynamic viscosity η' is in good agreement with the high frequency limit η'_∞ for colloidal hard sphere suspensions. Around $\gamma_0 = 1$ the 'cage' around a particle is deformed and a shear-induced microstructure is built. This leads to $O(a)$ displacements of the particles and the viscoelastic response becomes strongly non-harmonic.

*This chapter has been submitted to *J. Chem. Phys.* as "Shear-induced Diffusion and Rheology of non-Colloidal Suspensions: Timescales and Particle Displacements" by V. Breedveld, D. van den Ende, R.J.J. Jongschaap and J. Mellema (2000)'

4.1 Introduction

Shear-induced diffusion is an important phenomenon in the field of suspension rheology. It is one of the basic transport processes in concentrated suspensions and has significant influence on the macroscopic flow behaviour of non-colloidal suspensions (see e.g. Acrivos, 1995). The underlying mechanism of shear-induced diffusion is formed by the velocity fluctuations of individual particles due to the changing configuration of all other particles. The macroscopic flow drives particles on adjacent streamlines towards each other and because of excluded volume effects the particles are forced to leave their streamlines. In concentrated suspensions the excluded volume effects result in net particle displacements. Although in principle hydrodynamic interactions are of deterministic nature, the changing configuration causes diffusive behaviour in concentrated suspensions.

The driving force of shear-induced diffusion differs from the more familiar concept of Brownian diffusion, which is driven by thermal forces and plays an important role for smaller, colloidal, particles. Moreover, shear-induced diffusion occurs at very low Reynolds numbers, so that inertia is insignificant as opposed to the case of particle dispersion in turbulent flows.

Since the experimental work of Leighton & Acrivos (1987a,b) shear-induced diffusion has been studied experimentally, numerically and theoretically by various research groups, both on the level of self-diffusion and collective or gradient diffusion (for a review see Davis, 1996). In this paper we restrict ourselves to self-diffusion, which describes the velocity fluctuations of individual particles.

Experimentally, shear-induced self-diffusion has been studied with a number of different techniques. Eckstein *et al.* (1977) have introduced the method of observing long-time displacements of a single tracer particle in a Couette flow by recording its position after each full rotation. The technique was improved by Leighton and coworkers (Leighton & Acrivos, 1987a; Phan & Leighton, 1993). They also introduced measurements of diffusion in the vorticity (z) direction.

In chapter 2 and 3 we have introduced another technique, which monitors the motion of an ensemble of tracer particles over much shorter times and extracts shear-induced diffusion coefficients by means of spatial correlation procedures. These measurements were also performed in a steady shear situation and reveal that for strain values roughly $\dot{\gamma}\Delta t > 1$ ($\dot{\gamma}\Delta t$ being the relevant dimensionless time) the particle motion becomes diffusive. The latest experimental studies in shear flow (chapter 2 and 3; Phan & Leighton (1993)) are in good agreement and have provided a consistent picture of the experimental values of the long-time diffusion coefficients.

Now that reliable experimental data are available on long-time shear-induced diffusion coefficients, it seems feasible to investigate particle motion in sheared non-

colloidal suspensions in more detail. Our technique offers the possibility to study the evolution of ensemble averaged particle displacements over a wide range of strain ($0.03 < \dot{\gamma}\Delta t < 3.5$). Thus we can focus on the regime where the transition to diffusive motion occurs ($\dot{\gamma}\Delta t \approx 1$). In addition the nature of particle motion for even smaller strain values can be studied. Since shear-induced self-diffusion in non-colloidal hard-sphere suspensions is induced by the changing configuration of the particles –the spatial distribution determines the velocity of individual particles under shear–, the motion of individual particles probes the underlying microstructure.

Experimentally we have investigated particle motion and its relevant timescales in two different ways. Characteristic particle trajectories are presented in section 4.3. The trajectories have been determined by means of particle tracking and enable direct observation of the motion of individual particles. These particle paths are useful in developing a qualitative picture of the particle motion.

The trajectories, however, are not very suitable to collect quantitative information about the particle displacements, since the method is laborious and a large number of trajectories is required for accurate statistical analysis. Detailed information about the ensemble averaged displacements was therefore obtained with our correlation method, which was originally developed to measure long-time self-diffusion coefficients (chapter 3). In section 4.4 the ensemble averaged data are evaluated in search for the characteristic timescales of the particle motion.

Not only self-diffusion, but also rheology is governed by particle positions, often represented by the particle distribution function. In a non-colloidal suspension of hard spheres without interparticle forces in Stokes flow, the net hydrodynamic force on any particle must be zero (see e.g. Brady & Bossis, 1988). In that case the stresses and viscosities are determined directly by microstructure. In section 4.5 we report on steady shear and dynamic rheometry. Similar experiments have been reported by Gadala-Maria & Acrivos (1980) and Gondret *et al.* (August 18-23, 1996); we have further explored the phenomena which they observed for our system. By combining the self-diffusion and rheological measurements for our suspensions a coherent picture arises. In section 4.6 we combine the results in an attempt to provide a consistent physical interpretation of our observations.

4.2 Materials and methods

For all experiments reported in this paper we made use of the experimental system described in chapter 2, a refractive index and density matched suspension of PMMA particles suspended in a fluid mixture of demineralized water, zinc-II-chloride and Triton X-100. The suspending fluid was measured to be Newtonian over the entire range of shear rates that could be covered by the rheometer (up to 100 s^{-1}) at a vis-

cosity of 3.4 Pa s (23°C). The particles (produced by ICI, class 4F, $\rho = 1.172$ g/ml) were sieved repeatedly to obtain a well-defined size fraction of diameter $90 \pm 15\mu$m. The sieved particles were density segregated to remove the particles with air-bubbles. A small fraction of the particles was then colored with fabric dye (Rit, CPC International) and used as tracer particles to visualize particle motion.

Correlation experiments were performed to measure the ensemble averaged particle displacements and subsequently extract the long-time self-diffusion coefficients. The technique is based on spatial correlation of tracer particle positions in sequences of video images; for a detailed description of our experiments in a counter-rotating cone-plate apparatus we refer to chapter 3. In the current chapter we reanalyze the results of the original study with the aim to collect detailed information about the microscopic nature of the diffusion process.

The video images used for the diffusion experiments could also be used to apply particle tracking. Thus the trajectories of individual tracer particles were determined over relatively long times. Our image grabbing system, consisting of CCD-camera, frame grabber and PC, was able to capture sequences of maximally 200 images. The upper limit was set by the amount of RAM (256Mb) in the frame grabbing PC. The actual physical length of the sequences –expressed in dimensionless strain units– depended on the interval time between consecutive images and on the shear rate, which were both varied. In this study we have collected time series in which particles could be tracked for as long as 50 strain units ($\dot{\gamma}\Delta t$). Sequences with shorter interval times were also analyzed to obtain a higher strain resolution.

The tracking procedure consisted of the following steps. First, suitable sequences were identified, in which a specific tracer particle remained within the camera window during the entire sequence. The images of these series were then analyzed with a commercial software package for image analysis (Optimas): the position of the tracer particle was determined manually by fitting a circular overlay to the particle contour. The position of the overlay was registered as a measure for the tracer position.

In spite of the software's sophisticated particle recognition algorithms the tracking procedure could not be automated. Not every image was of sufficiently high quality because of particle overlap and other image distortions. When measuring the self-diffusion in chapter 3 this effects was unimportant, since the ensemble statistics were not affected significantly by the odd missing tracer position. Particle tracking, however, requires accurate knowledge of the particle position at every moment in time. Omissions in the time series would seriously disrupt the trajectory. By performing the analysis manually even the positions of overlapping tracers could be determined accurately. As long as a significant part of the particle contour is visible, precise placement of the circular overlay is relatively easy. Furthermore, automatical

particle tracking would require a clever algorithm to identify individual particles in subsequent images, which by eye is a simple task.

In order to determine the experimental errors of the manual particle tracking procedure, for a number of images the manual outcome was compared to the results of the automated image analysis algorithm which was employed in the diffusion experiments. The influence of the operator was also checked by having a small sample of images analyzed by different people. All in all the error in tracer position as measured with the manual procedure turned out to be no larger than 1 pixel, which was also the spatial resolution of the placement of the circular overlay.

The rheological properties of the suspensions were characterized using a controlled stress rheometer (Haake RheoStress RS150) equipped with a Couette geometry (inner and outer gap radius respectively 20.71 and 21.71 mm). Since the average particle diameter is 90 μm, the gap is on the small side according to the rheological rule of thumb that a minimum gap size of circa 15 particle diameters is required for reliable viscosity measurements. As a result, we cannot exclude wall-slip in our system. Wall-slip would have influenced our rheological experiments, leading to underestimated viscosity values. However, a Couette geometry with larger gap was unavailable and we believe that our most important observations, the oscillatory measurements to be presented in section 4.5 (fig. 4.10), have not been affected by the limited gap size. This belief is supported by the fact that quantitatively identical results have been observed by Knipmeyer & Pine (2000) in a wider Couette geometry with roughened walls where wall slip is unlikely to play a role.

After loading the suspensions we applied pre-shear to eliminate the loading effects that have been reported by Leighton & Acrivos (1987b) under similar experimental conditions and that have been related to shear-induced gradient migration across the annular gap. Stress sweeps were then applied to measure the flow curves and finally frequency sweeps were performed at constant stress values. The details on the chosen values of stress and frequency are given in section 4.5

4.3 Particle trajectories

Direct visual observation is a natural approach when studying particle motion, especially for non-colloidal suspensions of 90 μm particles that can easily be visualized with standard optics. As described in the previous section, video images were taken from concentrated refractive index matched suspensions with a small fraction of opaque tracer particles. Besides the diffusion measurements to be described in the next section, the images could also be used to reconstruct trajectories of individual tracer particles.

To this purpose image sequences had to be identified for which tracers remained

within the observation window for a much longer period than needed for the diffusion measurements. Sequences could be found with particle residence times as long as 50 strain units. Figure 4.1 shows typical particle trajectories in the $x-z-$plane for suspensions of 30 and 50% particle volume fraction. The strain step $\dot{\gamma}\Delta t$ between consecutive points in the graphs is 0.24 (for particles 3 and 4 in *(a)* the interval is 0.024). The figure represents the location of the particles on the CCD image (752x568 pixels). The measured positions were slightly shifted to minimize overlap of the trajectories and improve clarity. The average particle size (diameter 62 pixels) is indicated on the left side.

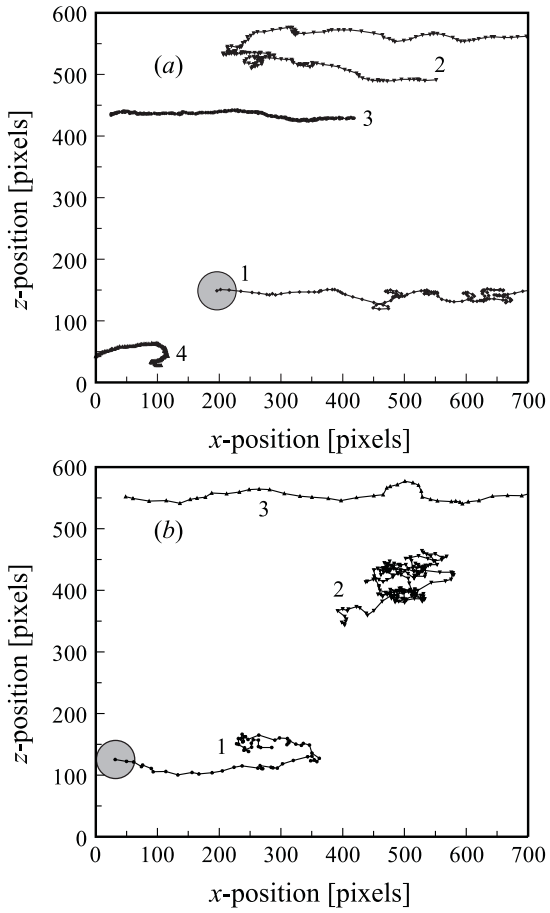

Figure 4.1: Typical particle trajectories in the image window ($\Delta x - \Delta z$-plane) for volume fractions *(a)* $\phi = 0.30$ and *(b)* $\phi = 0.50$; strain $\dot{\gamma}\Delta t$ between consecutive points is 0.24 for all particles, except for particle 3 and 4 in *(a)*, where the strain interval is 0.024. The paths have been shifted over arbitrary distances to minimize overlap and improve clarity.

The trajectories are replotted in figure 4.2, representing the particle coordinates as a function of time. The starting point of all trajectories was set to $\dot{\gamma}\Delta t = 0$ and although some of the particles in figure 4.1 were followed for as long as 50 strain units, figure 4.2 has a maximum strain $\dot{\gamma}\Delta t = 30$ so that details can be distinguished. Note that different particles could be tracked over different lengths of time. The refined trajectories of the high resolution measurements of particle 3 and 4 in the 30% suspension ($\dot{\gamma}\Delta t = 0.024$) did not alter the picture. All important observations can be made from the long (low resolution) trajectories with $\dot{\gamma}\Delta t = 0.24$.

For both concentrations, the fluctuations in the $x-$direction (closed symbols) are more pronounced than in the $z-$direction (open symbols). The explanation is straightforward: displacements in the $y-$direction (the unregistered out-of-plane velocity gradient direction) onto a different streamline inherently affect the convective motion in the velocity direction (x). Since the motion in the $y-$direction is also of diffusive nature, the observed fluctuations along the $x-$axis are the result of two processes: the fluctuations in $x-$velocity itself and an additional coupling term due to fluctuations in the $y-$direction.

The convective velocity field also causes the particles to occasionally drift over large distances along the $x-$axis, i.e. when they are displaced onto a different streamline. Because of this, the particles can drift away from the zero velocity plane and (temporarily) disappear from the viewing window (for example particle 3 at both concentrations). On average, however, the particles should fluctuate around their original position, which is validated by the $z-$data of figure 4.2*a* and *b*.

The largest displacements in figure 4.2 are of $O(a)$ for both volume fractions and in both flow directions (a being the particle radius), thus confirming the scaling ideas of Leighton & Acrivos (1987a) and Brady & Morris (1997) which are based on the assumption that interactions will lead to displacements of the size of the particle. The present study provides unique experimental evidence in support of their predictions. In particular the $O(a)$ displacements in the $z-$direction are notable. Calculations of particle interactions in the dilute regime (da Cunha & Hinch, 1996; Wang *et al.*, 1996; Pesche, 1998) have shown that displacements in the vorticity direction are considerably smaller than in the velocity gradient direction, irrespective of the mechanism responsible for braking the symmetry of two particle interactions in Stokes flow: particle roughness (Da Cunha & Hinch, 1996), the presence of a third particle (Wang *et al.*, 1996) or a repulsive force (Pesche, 1998). As a consequence, the calculations in the dilute regime render highly anisotropic self-diffusion coefficients, $\hat{D}_{yy}/\hat{D}_{zz} \sim O(10)$, while experiments (chapter 3, Phan & Leighton (1993)) and Stokesian Dynamics calculations (Foss & Brady, 1999) in the concentrated regime both find $\hat{D}_{yy}/\hat{D}_{zz} \approx 2$. Taking into account that both theoretical (dilute) and Stokesian Dynamics (concentrated) calculations show $O(a)$ displacements in the $y-$direction, our experimental particle trajectories with $O(a)$ steps in the $z-$direction (fig. 4.2) are

in good agreement with the data for concentrated suspensions. Apparently, additional effects must be incorporated in the theories for dilute suspensions to account for the relatively low experimental anisotropy.

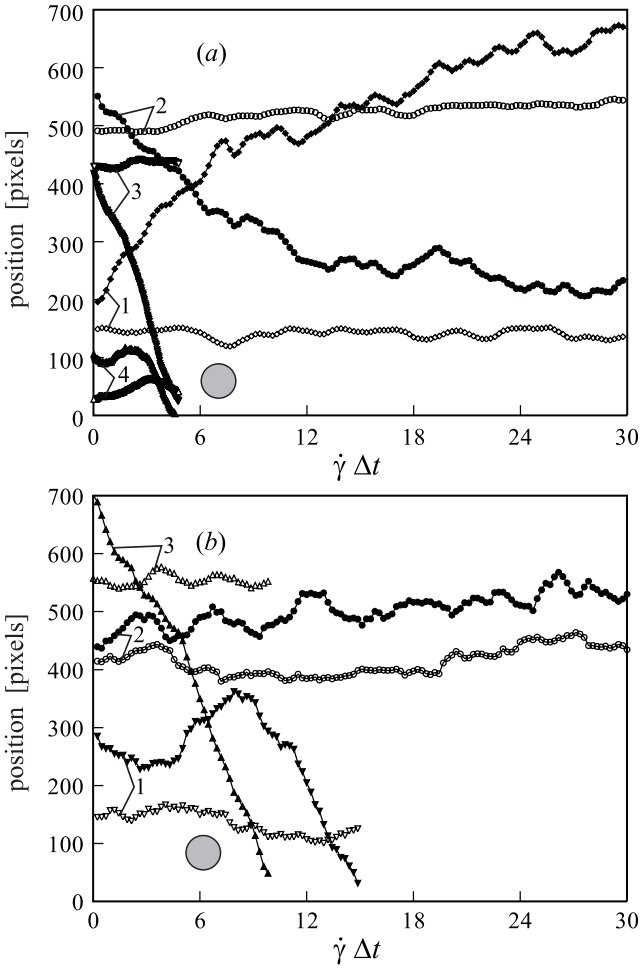

Figure 4.2: Positions of individual particles as a function of dimensionless time $\dot{\gamma}\Delta t$ for *(a)* $\phi = 0.30$ *(b)* $\phi = 0.50$ in the $x-$direction (closed symbols) and $z-$direction (open symbols). Numbers correspond to fig. 4.1 and the average particle size is indicated.

Figure 4.1 and 4.2 reveal slight differences in particle motion at the two volume fractions. For $\phi = 0.30$ the curves are very smooth, which is particularly clear in the $z-$direction. The particle trajectories consist of a chain of successive displacements, which occur relatively slowly. In the highly concentrated 50% suspension the particles move more violently: the major displacements occur faster and are larger

in amplitude. In between the large steps the particles keep wiggling around their location with a characteristic time that is shorter than the sampling interval. Occasionally, sudden stationary sections can be observed (e.g. $x-$position of particle 2 around $\dot{\gamma}\Delta t = 12$) as if the particle is trapped.

Although the trajectories provide useful insight into the motion of individual tracers, they are less suitable for a detailed quantitative analysis. The manual procedure is labor-intensive and a significant number of paths would be needed for reliable statistics.

4.4 Self-diffusion measurements

For a quantitative analysis of the particle motion we have switched to another observational level: the statistics of motion of a large ensemble of particles.

In recent years we have developed a correlation technique for measuring self-diffusion coefficients in non-colloidal suspensions under shear (described in chapter 2 and 3). Without going into details, the experimental procedure essentially results in $\langle \Delta x \Delta x \rangle / a^2 - \dot{\gamma}\Delta t-$graphs which show the ensemble averaged square displacement versus time. Both the displacement and time are made dimensionless by scaling with respectively the particle radius a and shear rate $\dot{\gamma}$. Linear scaling in these graphs indicates diffusive behaviour and in that case the self-diffusion coefficients can be extracted directly from the slope of the linear regime, making use of the standard diffusion relation $\langle \Delta x \Delta x \rangle \sim 2\, D\, \Delta t$.

The transition to the linear (diffusive) regime is expected to depend on the underlying microstructure of the suspension. Therefore we believe that a detailed timescale analysis of the shear-induced diffusion data will yield valuable information about the microstructure in sheared suspensions. Figure 4.3 is reproduced from chapter 3 and shows the results of the original correlation study together with the long-time linear fits which were used to determine the long-time diffusion coefficient $\hat{D}$ (also dimensionless). The graphs all concern particle displacements in the vorticity (z) direction, which was also visible in the particle trajectories of the previous section.

Figure 4.3 shows a transition to linear (diffusive) behaviour that is most pronounced for the lowest volume fractions. The evolution from figure *a* to *d* suggests that the transition time decreases with increasing volume fraction ϕ.

In an attempt to find a quantitative criterion for the transition point the data were plotted on log-log-scale, so that deviations of the linear fit could be observed more clearly. In figure 4.4 the logarithmic versions of figure 4.3 are presented together with the long-time linear fit and the results of an empirical model fit to be described in section 4.4.1. The deviations of the data at short times from the long-time linear fit are more pronounced, but it proved to be difficult to formulate an objective quantitative criterion to unambiguously determine the transition location.

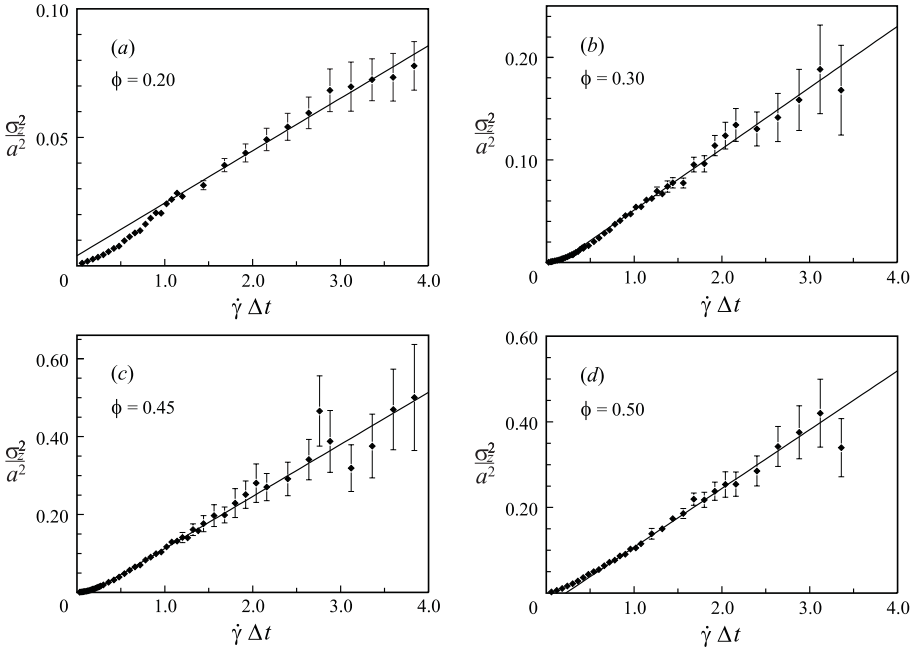

Figure 4.3: Scaling of the average squared particle displacement σ_z^2/a^2 with dimensionless time $\dot{\gamma}\Delta t$ for *(a)* $\phi = 0.20$,*(b)* $\phi = 0.30$, *(c)* $\phi = 0.45$ and *(d)* $\phi = 0.50$; the lines represent the linear fit to the data points at long times.

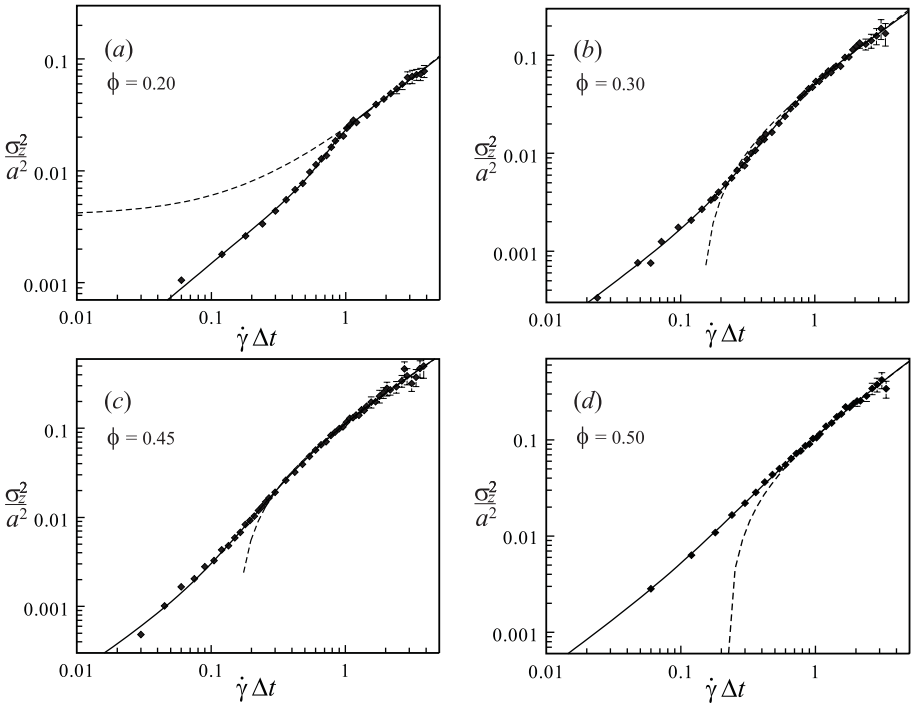

Figure 4.4: Logarithmic version of figure 4.3; σ_z^2/a^2 versus $\dot{\gamma}\Delta t$ for *(a)* $\phi = 0.20$, *(b)* $\phi = 0.30$, *(c)* $\phi = 0.45$ and *(d)* $\phi = 0.50$; the dashed lines (- - -) represent the linear fit to the data points at long times, the solid lines (—-) are the results of the empirical fit with equation 4.1.

The preferable approach for the characterization of the curves in figure 4.4 would have been the use of a theoretical model which contains the transition time as a fitting parameter. In this idealized situation standard statistical fitting routines could provide an unambiguous best fit value for the transition time. However, no theoretical model with a sound physical basis has been developed so far for shear-induced self-diffusion. Therefore we have chosen another solution.

4.4.1 Empirical model

We have attempted to find an empirical model that is capable of describing the curves of figure 4.4. Such a model should fulfill a number of important requirements in order to be scientifically acceptable. First of all, it should provide an accurate fit to the experimental data over the entire range of data. Secondly, it should involve a minimum number of free parameters and finally these parameters should have physical significance.

A closer look at the log-log-plots of figure 4.4 discloses interesting scaling in the short-time regime. Within the classical framework of diffusion a transition might be expected from quadratic ('ballistic') to linear (diffusive) scaling. However, the graphs do not display slope +2 at short times. Instead, the suggestion arises that the short-time scaling is also more or less linear, with slope +1. This observation implies the existence of two diffusive regimes: the long-time shear-induced self-diffusion which is characterized by the linear fit in figure 4.3 and an additional short-time diffusivity for $\dot{\gamma}\Delta t$ smaller than roughly 0.20. On intermediate timescales there is a smooth transition between the two diffusive regimes.

The considerations mentioned above lead to the following empirical model to capture the observed phenomena:

$$\frac{\sigma^2}{a^2} = \frac{c_2 \cdot \dot{\gamma}\Delta t}{1 + (\frac{\dot{\gamma}\Delta t}{c_0})^{c_1}} + \frac{(c_3 \cdot \dot{\gamma}\Delta t + c_4)(\frac{\dot{\gamma}\Delta t}{c_0})^{c_1}}{1 + (\frac{\dot{\gamma}\Delta t}{c_0})^{c_1}} \tag{4.1}$$

where σ/a and $\dot{\gamma}\Delta t$ are the dimensionless peak width and time. In the limits of short and long times equation 4.1 converges to the asymptotes:

$$\frac{\sigma^2}{a^2} = c_2 \cdot \dot{\gamma}\Delta t \quad \text{for } \dot{\gamma}\Delta t \ll c_0 \tag{4.2}$$

$$\frac{\sigma^2}{a^2} = c_3 \cdot \dot{\gamma}\Delta t + c_4 \quad \text{for } \dot{\gamma}\Delta t \gg c_0 \tag{4.3}$$

The fit parameters can be interpreted as follows: the location of the transition (c_0), the strength of the transition (c_1), the short-time diffusion coefficient ($c_2 = 2\hat{D}_0$), the long-time diffusion coefficient ($c_3 = 2\hat{D}_\infty$) and the off-set of the linear long-time fit

(c_4). Equation 4.1 is similar to the well-known Cross model, often used to characterize shear-thinning fluids with two viscosity plateaus Cross (1965).

Equation 4.1 was used to parameterize the data by means of a standard least square non-linear fitting routine. Since the linear fits in figure 4.3 show that the off-set of the long-time linear fit only differs significantly from 0 at high volume fractions ($\phi > 0.35$), parameter c_4 was used in equation 4.1 only if it had a significant and meaningful contribution to the convergence of the fitting routine. The fit procedure was carried out with $1/\varepsilon^2$ as weight factor, ε being the statistical standard deviation of σ^2/a^2 that was also used for the error bars in figures 4.3 and 4.4. In their turn these errors have been obtained from non-linear Gaussian fits (chapter 3).

4.4.2 Fit parameters

The results of the empirical model fit are presented in figure 4.4 as the solid curves. It can be concluded that the proposed model describes the data surprisingly well over the full range of time and volume fraction.

Although the proposed model is of empirical nature, its parameters have a clear physical meaning and their dependence on particle volume fraction ϕ, as presented in figure 4.5, can serve as a starting point to gain physical insight into the nature of the processes that take place in concentrated suspensions under shear. The error bars in the graphs are purely the result of an external statistical estimation, obtained from the covariance matrix of the non-linear fit. It provides an explanation for the fact that some of the data points (e.g.c_0 for $\phi = 0.45$) have unrealistically small errors in comparison to the rest of the data points. Nevertheless, this error estimate is the only available objective measure of the parameter reliability and regarding the empirical nature of our model it seemed appropriate to present those values.

Of the fitting parameters, c_2 and c_3 are directly related to the physical quantities $\hat{D}_0$ and $\hat{D}_\infty$, respectively a short- and long-time diffusion coefficient (eq. 4.2). The dependence of c_3 on ϕ should be identical to that of the long-time self-diffusion coefficient $\hat{D}_{zz}$ which was determined by using the long-time linear fit of figure 4.3 in chapter 2. This requirement is indeed satisfied.

The existence of a short-time diffusion regime, however, has not been reported before. As far as we are aware no previous experimental technique has been capable of measurements on such short timescales and no detailed analysis of numerical simulations in this regime has been reported so far, although it should be relatively straightforward to retrieve the necessary data from standard simulation runs.

Although for the highest volume fractions the short-time linear regime lies outside the accessible time window, the quality of the fit with equation 4.1 and the data for $\phi = 0.20$ and 0.30 provide strong evidence that short-time diffusivity indeed exists at all volume fractions. The corresponding diffusion coefficient, $\hat{D}_0 = 0.5 \cdot c_2$, exhibits a ϕ-dependence that strongly differs from the behaviour of $\hat{D}_\infty$. Although

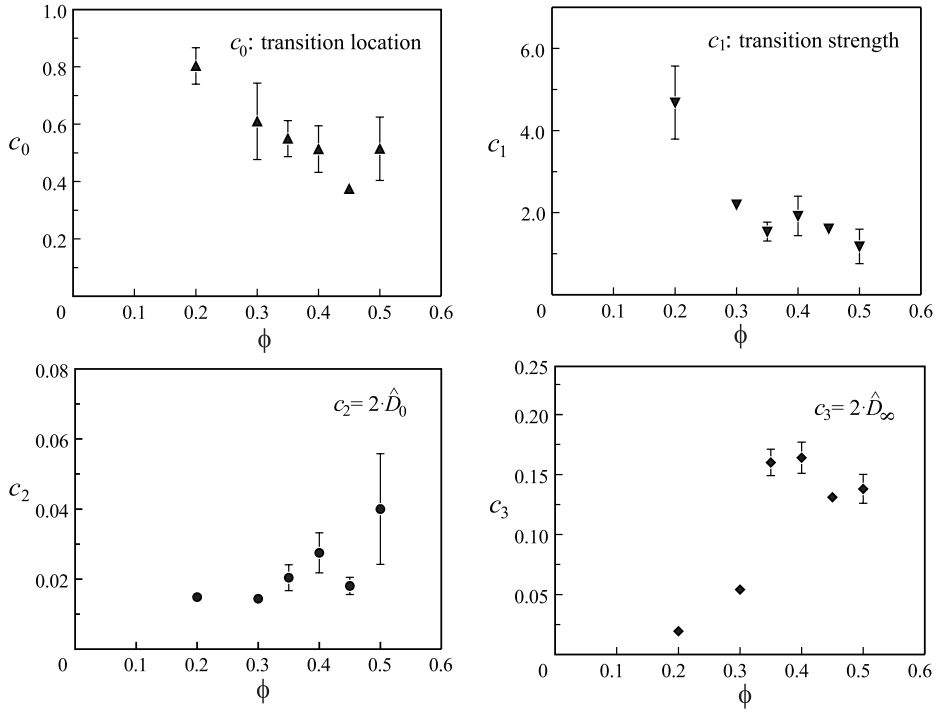

Figure 4.5: Fit parameters of equation 4.1 as a function of ϕ.

the standard deviations are significant because of the limited amount of data at short times, especially for $\phi = 0.50$, $\hat{D}_0$ seems to grow continuously with increasing ϕ, whereas $\hat{D}_\infty$ increases strongly for intermediate volume fractions, followed by a plateau above $\phi = 0.35$ and an apparent decrease at even higher volume fractions (reported as well by Phan & Leighton (1993)).

The parameters c_0 and c_1 are somewhat more difficult to interpret. They characterize the transition between the two diffusion regimes through its slope (c_1) and location (c_0). For the development of a physical picture of the microscopic processes, it seems more useful to define two transition times, $\hat{\tau}_0$ and $\hat{\tau}_\infty$, which respectively mark the end of short-time and the onset of long-time diffusion, expressed in dimensionless strain units.

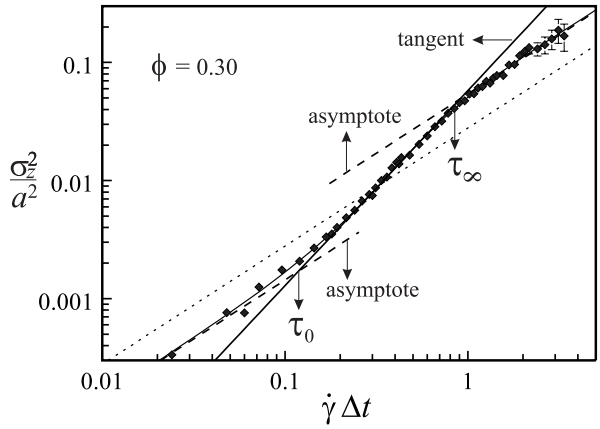

Figure 4.6: Definition of the characteristic dimensionless times $\hat{\tau}_0$ and $\hat{\tau}_\infty$; the dashed lines denote the asymptotes, the dotted line the intermediate line and the thin curve the fit function equation 4.1; the thick line represents the log-log tangent at the intercept.

The definition of $\hat{\tau}_0$ and $\hat{\tau}_\infty$ that we have chosen is illustrated in figure 4.6. The characteristic times are determined as follows: first, in the log-log-plot (figure 4.4) the linear asymptotes of equation 4.2 are drawn and used to construct an additional line in between. The intersect of this intermediate line with the model fit (eq. 4.1) is then determined analytically and at the intersection point the tangent of the fit function (straight line in the log-log-plot) is calculated. Finally, the intersects of the tangent with the asymptotes can be computed and these points are called $\hat{\tau}_0$ and $\hat{\tau}_\infty$.

The values of $\hat{\tau}_0$ and $\hat{\tau}_\infty$ were calculated for all volume fractions and are plotted in figure 4.7. The logarithmic scale was chosen to enable direct comparison of the two times, which differ by an order of magnitude. The error bars are the result of a rigourous analysis of the propagation of errors: for each fit parameter (c_0 to c_4) the influence of its statistical error on the determined values for $\hat{\tau}_0$ and $\hat{\tau}_\infty$ was calculated.

The resulting error estimates were summed quadratically to obtain a reliable measure for the error bars in figure 4.7.

Within the experimental errors, which are significant especially for $\phi = 0.50$, the longest timescale $\hat{\tau}_\infty$ is constant at $\dot{\gamma}\Delta t \sim 1$ over the full range of volume fractions, indicated by the dashed line.

The shortest timescale, $\hat{\tau}_0$, is an order of magnitude smaller and decreases with ϕ. Simple hand-waving arguments can be used to estimate an upper limit for $\hat{\tau}_0$. The point where short-time diffusion ends and long-time diffusion starts to dominate particle motion, here characterized by $\hat{\tau}_0$, should be smaller than the affine shear deformation where particles directly interact with their nearest neighbours. This deformation can be approximated by δ/a with a the particle radius and δ the space around a particle in the 'cage' formed by its neighbours. Assuming a homogeneous distribution of monodisperse particles, δ/a can be estimated by means of the following equation:

$$\frac{\delta}{a} = \left(\frac{\phi_{\max}}{\phi}\right)^{1/3} - 1 \tag{4.4}$$

where $\phi_{\max}$ denotes the maximum particle volume fraction. In figure 4.7 the curve (dash-dotted) has been drawn for $\phi_{\max} = 0.63$ and provides a decent upper limit to the data.

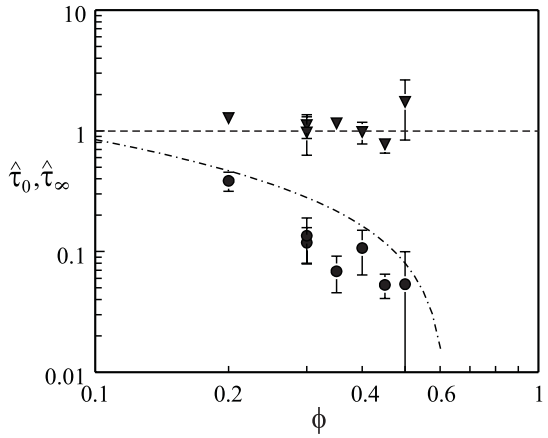

Figure 4.7: Transition times (●) $\hat{\tau}_0$ and (▼) $\hat{\tau}_\infty$ as a function of ϕ; (- - -) represents $\hat{\tau} = 1$ and (- · -) eq. 4.4 with $\phi_{\max} = 0.63$.

4.5 Rheological measurements

In addition to the direct observation of particles and a statistical analysis of the displacements we have investigated the rheological properties of the suspensions. Like shear-induced diffusion the rheological properties are the result of the underlying microscopic structure. Rheometry thus can be used as an independent method to experimentally address fundamental questions about the nature of the particle distribution in suspensions.

Our rheological experiments on concentrated non-colloidal suspensions were inspired by the work of Gadala-Maria & Acrivos (1980) and Gondret *et al.* (August 18-23, 1996), who observed peculiar behaviour of the dynamic viscosity η' of non-colloidal suspensions. In order to relate the diffusion and rheology in our system, we have carried out similar experiments for our suspensions. Since the physical chemistry of suspensions is known to be of great influence on the rheology, it is non-trivial that our specific suspension should behave exactly like the materials used in previous studies.

Amongst other observations Gadala-Maria & Acrivos (1980) discovered that the stress response in their controlled strain oscillations in both plate-plate and Couette configuration was linear at low strain amplitudes, but became highly non-linear at amplitudes of $\gamma_0 \sim 1$ (see their figure 8).

Gondret *et al.* (August 18-23, 1996) reported that the dynamic viscosity of concentrated suspensions strongly depended on frequency and amplitude of the oscillations. As far as we can reconstruct from their paper, the experiments were carried out in a plate-plate geometry as well, which has the disadvantage that the strain distribution over the sample volume is highly non-uniform, being zero in the center and maximum at the edge of the plates.

Our rheological measurements were carried out in a controlled stress rheometer with Couette geometry (see section 4.2). Before performing dynamic measurements, first the flow curves of the suspensions were determined. Contrary to Gadala-Maria & Acrivos (1980) we did not wait for the equilibrium value to be reached, as it has been shown by Leighton & Acrivos (1987a) that the gradual decrease of viscosity in their experiments can be attributed to shear-induced particle migration out of the Couette gap towards the stagnant fluid reservoir below the inner cylinder. To prevent migration, which would decrease the particle volume fraction in the annular gap, we have pre-sheared the suspensions only for a relatively short time as described in section 4.2 in order to reach a reproducible starting point.

Due to particle migration out of the gap it was inevitable that in the course of our experiments the viscosity slightly decreased. We have been careful to minimize the applied shear in order to limit this effect. Figure 4.8 presents the typical flow curves

we found. As an estimate of the effect of migration flow curves are shown which were taken before and after our oscillatory experiments, the curves being separated by circa 14 hours of oscillations. The curves for 30% overlap nearly perfectly, but for the 50% suspension a significant decrease in η_r was observed after the initial pre-shear.

As correctly pointed out by Gadala-Maria & Acrivos (1980), migration complicates the comparison of steady shear viscosity results for non-colloidal suspensions from various researchers. Such a comparison is not the purpose of our current work, we just note that our viscosity data are somewhat higher than the results of Gadala-Maria & Acrivos (1980) which should be expected since we do not wait for the system to reach the migratory equilibrium.

Figure 4.8 exhibits shear-thinning behaviour, most notably at the highest volume fraction. The shear-thinning is also present in the equilibrium curves of Gadala-Maria & Acrivos (1980), but in their case it can be –at least partly– explained by the fact that shear-induced migration increases with shear rate, thereby lowering the volume fraction in the annular gap with increasing shear rate. The flow curves were measured subsequently for increasing and decreasing stresses and the minimal amount of hysteresis was insufficient to relate the shear-thinning effect to shear-induced particle migration.

Recently, Zarraga *et al.* (2000) have presented steady shear viscosity data from parallel plate rheometry and reported the same phenomenon. As they suggest, the explanation probably lies in the underlying suspension microstructure, but it is unclear what happens exactly. As far as we could examine, our PMMA particles can be considered as hard spheres without additional interparticle interactions. Refractive index matching eliminates Van der Waals interactions even at the lowest shear rates and the large amount of salt screens off electrostatic repulsions –if present at all. Brownian motion, finally, is also extremely small for our 90 μm particles and cannot be held responsible for the shear-thinning behaviour.

The steady shear experiments were followed by dynamic measurements. Because of the controlled stress nature of the Haake RS150 rheometer, the stress amplitude of the oscillations (σ) was kept constant, while the angular frequency (ω) was varied from 0.0094 to 628 rad s^{-1} (0.0015-100 Hz). Because of constant σ, the amplitude γ_0 of the strain response varied with ω. For a sample with frequency independent rheological properties (e.g. Newtonian fluid) the relation would simply have been $\gamma_0 \sim \sigma/\omega$.

Figure 4.9 shows the result of frequency sweeps for different values of σ and $\phi = 0.30$. In the left graph, the strain amplitude of the response signal γ_0 is plotted versus ω. As expected, γ_0 decreases strongly with ω and for each specific value of ω the strain amplitude increases with σ. The corresponding data for the relative dynamic viscosity η_r' data are presented in the right graph and show very pe-

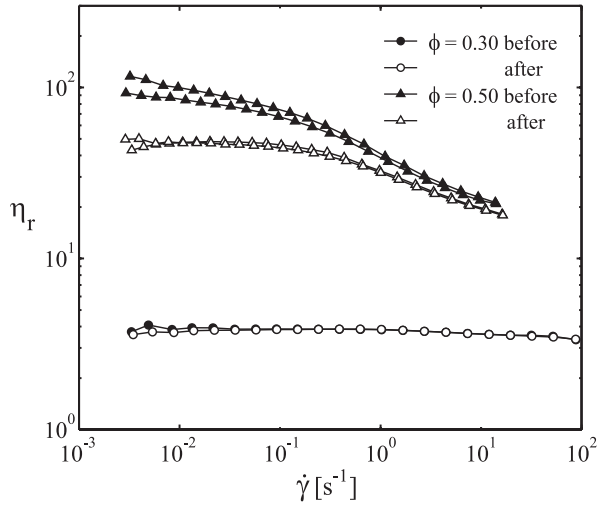

Figure 4.8: Relative shear viscosity of concentrated non-colloidal suspensions as measured by a controlled stress rheometer with Couette geometry; (○) $\phi = 0.30$ and (△) $\phi = 0.50$; closed symbols were measured before and open symbols after the dynamic measurements, about 14 hours later.

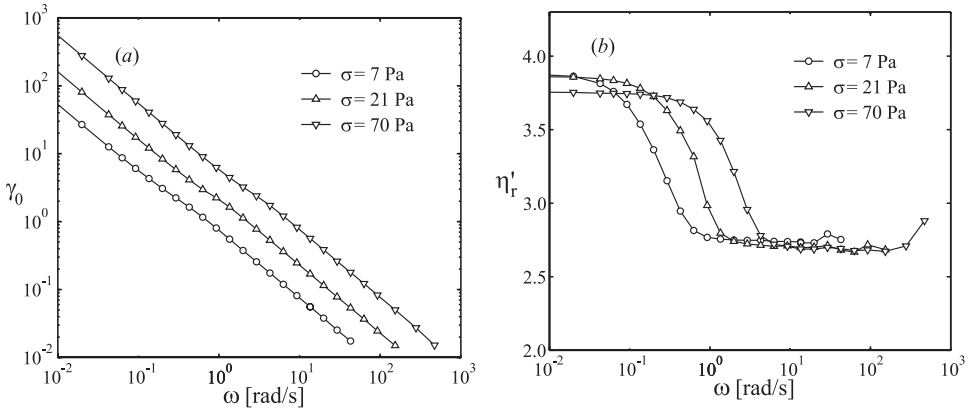

Figure 4.9: Results of constant stress frequency sweeps for a 30% suspension; *(a)* the amplitude of the strain response, γ_0, vs. angular frequency ω and *(b)* η_r' vs ω for varying stress values: (○) 7 Pa, (△) 21 Pa and (▽) 70 Pa.

culiar behaviour. At low frequencies η'_r has a well-defined plateau value. Another –considerably lower– plateau is observed at high frequencies. In the intermediate regime, there is a sharp transition, which shifts with variations in the stress amplitude σ.

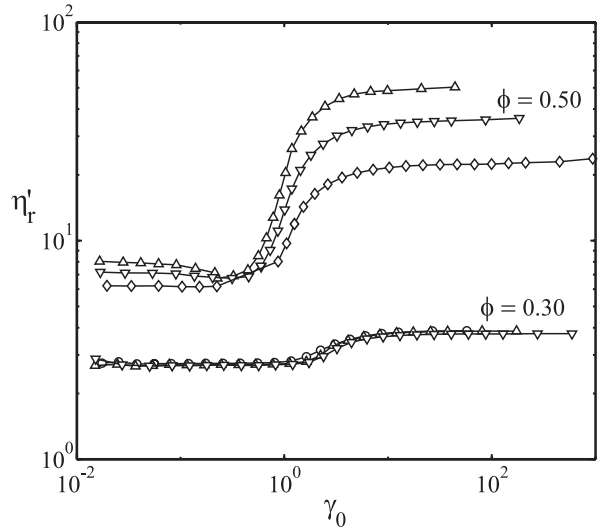

Figure 4.10: Relative dynamic viscosity η'_r versus amplitude of the strain response, γ_0, measured for $\phi = 0.30$ and 0.50 in frequency sweeps at various stress levels: ($\circ$) 7 Pa, ($\triangle$) 21 Pa, ($\triangledown$) 70 Pa and ($\Diamond$) 210 Pa.

The two graphs of figure 4.9 suggest that the η'_r transition is determined by strain amplitude rather than by frequency. To check this hypothesis, we have plotted η'_r against γ_0 in figure 4.10 for $\phi = 0.30$ and 0.50 (note the logarithmic scale). The transitions in the dynamic viscosity curves nicely collapse for both volume fractions. A sudden change in the viscoelastic response of the suspension occurs at strain amplitudes around $\gamma_0 \sim O(1)$.

Figure 4.10 clearly shows that for our non-colloidal suspensions the dynamic viscosity η'_r strongly depends on strain amplitude γ_0. Within rheological nomenclature it would thus be more appropriate to name the quantity "*apparent* dynamic viscosity", since the use of η' is generally restricted to the linear low strain regime. However, to avoid extended formulations we simply refer to η' as "dynamic viscosity" over the entire measurement range, referring to the out of phase component of the strain response signal as produced by the rheometer.

Graphs similar to figure 4.10 were obtained by Gondret *et al.* (August 18-23, 1996), but in their experiments the transitions were more gradual, most probably due to the wide range of shear rates in the parallel plate configuration which smooths out strain dependent transitions.

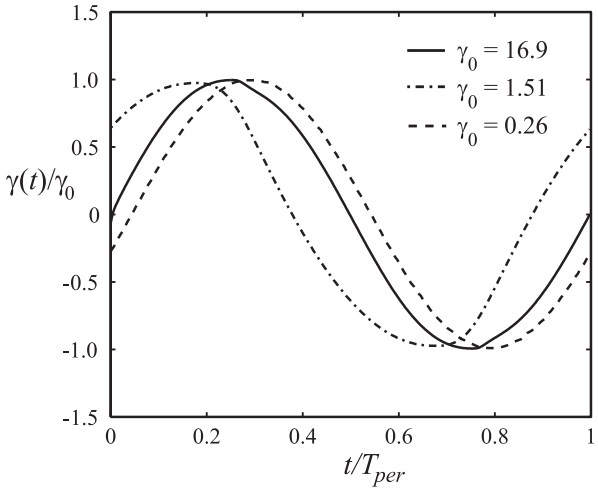

Figure 4.11: Strain response signals $\gamma(t)$ for sinusoidal stress input signal (amplitude 70 Pa) at three different values of ω –and therewith γ_0–; $\phi = 0.50$ and the curves are scaled by the oscillation period T_{per} and amplitude γ_0.

A close look at the raw oscillatory signals provides more insight into the observed effects, as can be seen in figure 4.11. The graph denotes the strain response functions for a 50% suspension at various frequencies (and thus various strain amplitudes). Note that for clarity the strain signals $\gamma(t)$ have been scaled by the oscillation period T_{per} and amplitude γ_0. Unfortunately, our rheometer was unable to start its measurements at a reproducible point of the stress input signal, so that no conclusions are to be drawn from the apparent phase differences in figure 4.11.

Below the transition (γ_0=0.26 in figure 4.11) the strain response is sinusoidal and linear, so that η' is independent of γ_0 and a plateau is found. In the transitional regime the response is strongly non-harmonic: the strain response for $\gamma_0 = 1.51$ resembles a saw-tooth rather than a sinus. Note that the signal is asymmetrical on reversal of flow direction at the maxima of the oscillation. At very large strain values (γ_0=16.9) the material response is nearly harmonic again, at a considerably higher value of η'. Traces of non-linear response can still be observed at the turning points where the flow direction changes, but at large amplitudes the response is dominated by a sinusoidal contribution that is responsible for the determination of η'_r. Figure 4.11 shows that the rheometer output for η'_r in the transitional regime has no clear physical meaning: η' is only a well-defined quantity for sinusoidal input and output.

The discrepancy between the two plateaus in figure 4.10 strongly increases with volume fraction, ranging from a factor 1.3 for $\phi = 0.30$ up to a factor 5 for $\phi = 0.50$.

The location of the transition ($\gamma_{0,\mathrm{tr}}$) also varies with volume fraction, defining $\gamma_{0,\mathrm{tr}}$ as the strain amplitude at the point where η_r' is halfway between the plateau values on the log-log-scale. The transition point shifts from $\gamma_{0,\mathrm{tr}} = 3.0 \pm 0.4$ for $\phi = 0.30$ to $\gamma_{0,\mathrm{tr}} = 1.0 \pm 0.2$ for $\phi = 0.50$, the errors being largely due to the variations in plateau values.

4.6 Discussion

The results of the various experimental techniques described in the previous sections provide inspiration for considerations on their physical background. In this section we will first discuss the results of diffusion and rheology separately and then draw the parallels and provide a framework for physical interpretation.

4.6.1 Self-diffusion

The self-diffusion data under steady shear are described extremely well by an empirical fit function (eq. (4.1)). The measurements show how the average particle motion develops when monitored from a certain arbitrary starting point in time ($\dot{\gamma}\Delta t = 0$). For very small deformations $\dot{\gamma}\Delta t$ the surroundings of a particle are hardly changed and particles are observed to move diffusively, characterized by a diffusion coefficient $\hat{D}_0$. In the particle trajectories this effect can be noticed for $\phi = 0.50$ in the shape of rapid fluctuations of small amplitude. For larger deformations, $\dot{\gamma}\Delta t \approx 1$, the initial particle configuration is distorted significantly and the average particle motion is affected accordingly. In this regime particles are forced by the shear flow to pass their neighbours. The trajectories clearly display the associated steps of size $O(a)$. After even longer times $\dot{\gamma}\Delta t > 1$, the correlation of the particle motion with the initial state is lost and a diffusive mode is reached, with diffusivity $\hat{D}_\infty$. Although the flow is in steady state macroscopically at every moment, the particle motion measured from an arbitrary starting point $\dot{\gamma}\Delta t = 0$ reaches a 'steady' diffusive state only after deformation $\dot{\gamma}\Delta t > 1$.

The characteristic times that can be associated with the transition, $\hat{\tau}_0$ marking the end of the short-time diffusion and $\hat{\tau}_\infty$ marking the on-set of long-time diffusion, show a different scaling with concentration, $\hat{\tau}_\infty \sim 1$ being constant and $\hat{\tau}_0$ decreasing with increasing ϕ. The associated diffusion coefficients $\hat{D}_0$ and $\hat{D}_\infty$ also exhibit different dependencies on ϕ: while $\hat{D}_\infty$ grows strongly with ϕ at intermediate concentrations ($\phi < 0.35$) and reaches a plateau value for higher volume fractions, $\hat{D}_0$ grows monotonically as a function of ϕ.

The $\phi-$dependence of the long-time self-diffusion coefficient is remarkable. As discussed in more detail in chapter 3 this particular behaviour has so far only been

found experimentally. Numerical Stokesian Dynamics calculations have not yet resulted in a clear numerical picture: shear-induced diffusion data seem to depend on system size and numerical algorithm. The only theoretical attempt by Brady & Morris (1997) predicts $\hat{D}_\infty$ to grow with ϕ up to volume fractions were flow becomes impossible. Their prediction, which is in fact an extrapolation of scaling relations in the dilute regime rather than a first principles theory, is based on the idea that diffusion should scale with the product of frequency and size of the particle displacements due to interactions. Using the contact value of the pair-distribution function $g_($**r**$)$, they argue that the interaction frequency should increase with volume fraction, while the step-size remains more or less constant $O(a)$, thus giving rise to an increasing diffusivity.

There is recent evidence however (Morris, 2000) that in numerical Stokesian Dynamics calculations at high concentrations (roughly above 30%) particle pairs tend to align in the flow direction. This effect is deduced from the appearance of peaks in the particle pair-distribution function $g(\mathbf{r})$ along the direction of flow. At high Péclet numbers the concentration of particle pairs is usually enlarged along the compressive axes of the shear flow, but recent calculations revealed the existence of additional peaks along the streamlines. The effect was not found to cause long-range order in the system (formation of particle strings), but the change in the local particle structure could very well be responsible for a decrease in the interaction frequency, since the increased number of particle pairs aligned along the streamlines effectively screens interactions with other particles on neighbouring streamlines. Thus the number of interactions would be reduced with increasing volume fraction, providing an explanation for the experimentally observed plateau in $\hat{D}_\infty$.

To our knowledge the experimental observations of a short-time shear-induced self-diffusion are unique. Its existence is concluded from the quality of an empirical model fit to all available data. Although clear experimental evidence exists it is not straightforward to interpret the observations. The existence of an additional short-time diffusive process in itself is not strange. In Brownian suspensions a similar distinction between long and short-time diffusion can be found: at short times the particles are rattling within the cage formed by their neighbours, the short-time self-diffusion, and only when the cage has been deformed sufficiently particles are able to undergo large displacements, characterised by a long-time self-diffusion coefficient.

Following the analogy with colloidal systems, apparently also non-colloidal systems exhibit small displacements within a 'cage' on timescales which are so short that the configuration of particles remains unchanged ($\dot{\gamma}\Delta t \ll 1$). Two possible mechanisms have come to our mind to explain these fluctuations in the absence of Brownian motion. The first possibility is an interparticle force with a short but finite range (e.g. as a result of inevitable particle roughness in experimental systems) which at

short times is able to relax the flow-induced contacts between non-colloidal particles by pushing them apart, thus giving rise to minute displacements. An alternative explanation could be found in the long-range character of the hydrodynamic forces in a sheared suspension. Each particle will not only feel the interaction with its immediate neighbours, but always experience fluctuations due to particle motion at larger distances. Fluctuations of this kind could cause diffusive displacements and would most likely be of a higher frequency than the interactions with direct neighbours, which give rise to long-time diffusion.

The 'cage' concept is in agreement with the observed behaviour of the transition time $\hat{\tau}_0$. As shown in figure 4.7 a simple calculation of the size of the cage (eq. (4.4)) provides a good estimate for the upper limit of the deformation where short-time diffusion should be dominated by the large displacements of long-time self-diffusion.

The experimental observation that $\hat{D}_0$ grows with ϕ (fig. 4.5) at first sight seems compatible with both mechanisms: at larger volume fractions stronger hydrodynamic fluctuations could be expected and also particles would be pushed harder towards each, which could lead to larger relaxation steps. Conclusive evidence on this topic could not be extracted from either of our experiments, but the persistent observation of $\hat{D}_0$ is quite intriguing.

4.6.2 Rheology

Steady shear and oscillatory measurements have shown that the two important parameters to characterize the results are stress and strain. The flow curves show that for increasing stress, shear-thinning occurs (fig. 4.8). This effect is most probably the result of changes in microstructure. All other possible explanations seem to fail: Brownian motion is absent and the presence of interparticle forces is unlikely.

In oscillatory experiments two strain regimes can be identified in the dynamic viscosity η'_r. At small amplitudes ($\gamma_0 \ll 1$) the stress and strain signals are harmonic and a well-defined plateau exists. The particle positions remain virtually unchanged during these measurements and the microstructure at rest is probed.

For larger amplitudes ($\gamma_0 \sim O(1)$) the strain signal becomes non-harmonic (see fig. 4.11). Similar non-harmonic responses were also reported by Gadala-Maria & Acrivos (1980) who analyzed the raw signals of their controlled strain rheometer for $\gamma_0 \leq 1.05$. The authors were able to directly relate the shape of the non-linear stress response to the build-up of shear-induced microstructure, which they also found in elegant steady shear flow reversal experiments. The typical deformation required to complete structure formation in the flow reversal measurements was $\gamma \sim 2$ and the value decreased with increasing volume fraction (see their Fig. 7). Oscillatory measurements on our suspensions corroborate their results. The characteristic strain value $\gamma_{0,\mathrm{tr}}$ which we used to define the location of the transition between the η'_r-plateaus is in quantitative agreement with the typical timescale for flow-induced structure for-

mation as measured by Gadala-Maria & Acrivos.

At very large strain amplitudes ($\gamma_0 \gg 1$) the particles are forced into a microstructure which resembles the situation under steady shear. After reversal of the flow direction only a small fraction of the oscillation period is needed to break down and rebuild the microstructure. During the remaining part of the oscillation, the microstructure has reached a steady state and the response is 'apparently' linear with a dynamic viscosity η'_r. This is nicely illustrated by figure 4.11, where the strain response is strongly non-linear for intermediate strain amplitude $\gamma_0 = 1.51$ after flow reversal, while only a relatively small dimple can be observed for the large amplitude experiment $\gamma_0 = 16.9$. In absolute strain units, the region of microstructural rearrangements are of the same magnitude for both signals: $\Delta\gamma \sim 3$.

The plateau values of η'_r at high strain oscillations exhibit shear-thinning behaviour that is similar to the steady shear flow curves. In particular for $\phi = 0.50$ the high strain plateau values do not overlap completely. The variations in plateau value can not be attributed to migration: in our experiments we have repeated the full sequence of three frequency sweeps for several times over night and the overlap between the first and last sequence at each specific stress value was excellent, the over night variations in η'_r at a specific stress value being much smaller than variations between different stress curves.

Quantitative analysis of the low strain (high frequency) plateau, where shear-induced microstructure is absent reveals an interesting observation. In figure 4.12 we have plotted the plateau values for our non-colloidal suspensions together with literature data on colloidal suspensions (van der Werff *et al.*, 1989; Shikata & Pearson, 1994). For colloidal hard-sphere suspensions the high frequency limit of the dynamic viscosity, $\eta'_{r,\infty}$, is a well-defined quantity representing the hydrodynamic viscosity contribution at timescales where the Brownian motion is negligible, so that the equilibrium particle distribution is probed. The agreement is excellent, suggesting that the high frequency viscosity of hard sphere suspensions is independent of Péclet number.

At first glance the agreement is remarkable. For colloidal particles the Brownian motion rapidly relaxes shear-induced structure after cessation of flow, but for non-colloidal particles this force is extremely weak so that the associated relaxation processes become very slow and the particle distribution is not in thermodynamic equilibrium during the dynamic measurements. Nevertheless, within experimental errors the high frequency measurements yield the same relative dynamic viscosity for both colloidal and non-colloidal systems.

This observation can be interpreted within the theoretical framework developed by Brady and coworkers (Brady & Morris, 1997). Their approach is based on analyzing the particle pair distribution function $g(\mathbf{r})$. Without going into the details,

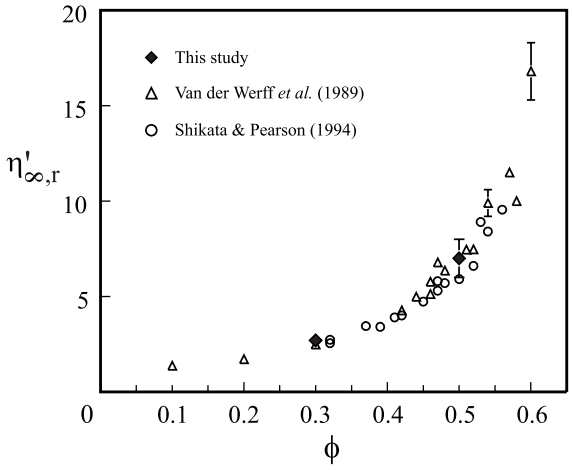

Figure 4.12: Relative dynamic viscosity η'_r as a function of particle volume fraction; low strain plateau values from this study (♦) are compared to the high frequency limit as determined by Van der Werff *et al.* (1989) (○) and Shikata & Pearson (1994) (△) for colloidal hard-sphere suspensions.

a relevant result of the analysis is the existence of a thin lubrication boundary layer around a particle of thickness $O(a\,\mathrm{Pe}^{-1})$, where Pe is the Péclet number and a the particle radius. At high concentrations the fraction of particle pairs residing within this boundary layer –described by the pair-distribution function at contact, $g(2,\theta)$– is argued to dominate the suspension stress. As a result, relaxation of this extremely thin boundary layer would be sufficient to remove the shear-induced viscosity contribution. Since the Péclet number in our non-colloidal system is very high ($O(10^{10})$), the boundary layer is so thin that even the extremely weak residual Brownian motion or the slightest particle roughness will be strong enough to rapidly destroy the boundary layer after cessation of flow. The high-frequency viscosity is then determined by the fraction of particles that remains within the boundary layer after relaxation, which is probed in oscillatory flow. Outside the equilibrium boundary layer our non-colloidal system has not reached thermodynamical equilibrium and the distribution is non-homogeneous. Nevertheless, the same $\eta'_{\infty,r}$-values are found for colloidal and non-colloidal systems, in accordance with the idea that the boundary layer dominates viscosity.

4.6.3 Relation between self-diffusion and rheology

In this section we compare the different observations and try to embed the results in a coherent physical interpretation. Our main aim is to provide a sound experimental basis for discussions about the microscopic processes in sheared suspensions and

not to give a detailed quantitative theoretical interpretation. We want to make use of the acquired expertise by pointing out striking correspondences within our set of experiments.

At first glance the combination of studying self-diffusion and rheology might raise questions. However, both physical quantities have the same origin: the spatial distribution of particles. This can easily be shown within the formalism used by Brady & Bossis (1988):

$$\begin{bmatrix} F^H \\ S \end{bmatrix} = \begin{bmatrix} R^{Fv} & R^{FE} \\ R^{Sv} & R^{SE} \end{bmatrix} \begin{bmatrix} v^\infty - v \\ E^\infty \end{bmatrix} \tag{4.5}$$

where $F^H \equiv (\mathbf{F}_1^H, \mathbf{F}_2^H, ..., \mathbf{F}_N^H)^T$ is a vector of the hydrodynamic forces on the N particles in the system. Similar definitions apply to the stresslet vector S and the particle velocities relative to the ambient flow $v^\infty - v$. E^∞ represents the external rate of strain. The resistance matrices $R_{\alpha,\beta}$ depend on the positions of all particles in the suspension.

By partial inversion Eq. 4.5 can be rewritten in a more suitable form (Jongschaap & Mellema, 1995):

$$\begin{bmatrix} v^\infty - v \\ S \end{bmatrix} = \begin{bmatrix} A^{vF} & A^{vE} \\ A^{SF} & A^{SE} \end{bmatrix} \begin{bmatrix} F^H \\ E^\infty \end{bmatrix} \tag{4.6}$$

where the matrix elements $A_{\alpha,\beta}$ are directly related to the resistance matrices $R_{\alpha,\beta}$ and thus also depend on particle configuration only. For our non-colloidal suspension in Stokes flow and in absence of interparticle forces, the hydrodynamic force $\mathbf{F}_i^H = 0$ on every particle. Thus the relative velocity and stresslet are functions of the external rate of strain and the particle configuration only. Self-diffusion is directly related to the autocorrelation of $\mathbf{v}^\infty - \mathbf{v}_i$, averaged over all particles. The macroscopic viscosity can be calculated through the integral of the particle stresslet $\mathbf{S}_i$ weighted with the particle distribution function. Thus both self-diffusion and viscosity directly depend on the spatial distribution of particles.

Because of the joint background, a comparison between the experimental results is meaningful. The on-set of the long-time self-diffusion regime in particle motion can be associated with the occurrence of non-linearity in the strain response signal during dynamic viscosity measurements. Both indicate the typical strain at which excluded volume effects of neighbouring particles become of importance. Indeed, there is qualitative agreement in the sense that both transitions take place for strain values of $O(1)$ and that the transition shifts to lower values for increasing volume fraction ϕ. Quantitative agreement is difficult to verify, since the definition of the transition locations is somewhat subjective.

The diffusion coefficient $\hat{D}_\infty$ and plateau in η_r' for large strain amplitudes show the effect of multiple excluded volume effects in the large deformation limit, where the

initial configuration has been lost. The volume fraction dependency of these quantities shows an notable correlation: at high volume fractions the long-time diffusion levels off, while the large amplitude dynamic viscosity increases strongly. Apparently, it becomes more difficult for particles to move and deformation requires larger stresses.

In the limit of small deformation the particle configuration is hardly changed. Both $\hat{D}_0$ and $\eta'_{r,\infty}$ reflect the suspension properties under these conditions and following the correlation for diffusion and viscosity at large deformations, they should be linked. The existence of a short-time diffusion requires the a driving force of unknown origin; two possible explanations were provided in section 4.6.1. From oscillatory measurements we have discovered that the small amplitude viscosity $\eta'_{r,\infty}$ of colloidal suspensions is the same as the high frequency limit for non-colloidal suspensions. These results, although not yet completely understood, set the stage for further discussion on the microstructure of concentrated suspensions.

4.7 Conclusions

We have experimentally studied the particle motion in concentrated non-colloidal suspensions under shear by employing three different techniques: particle tracking to determine the trajectories of individual particles, ensemble averaged displacements statistics and rheometry. The techniques probe the suspension on three different levels: the microscopic particle position, the ensemble level of average motion and the macroscopic level of mechanical properties. The combination of measurements has enabled us to find a number of intriguing results which altogether provide a coherent qualitative physical picture of the microscopic structure in sheared suspensions.

Particle tracking revealed that for medium concentrated suspensions (30%) the particle trajectories are very smooth with distinct displacements due to interactions with neighbouring particles on the characteristic timescale of the shear flow ($\dot{\gamma}\Delta t \sim O(1)$). The size of the displacements in both the vorticity and velocity direction was $O(a)$, which is in agreement with shear-induced diffusion experiments. The fluctuations in the velocity direction are more pronounced and this could be attributed to the coupling of diffusion in the velocity gradient direction with the convective flow.

For a highly concentrated 50% suspension the picture is similar, although the frequency and size of the displacements are slightly larger and the particles exhibit additional fluctuations of a shorter timescale superimposed on the 'slow' fluctuations.

A more detailed analysis of previously reported shear-induced self-diffusion data showed that in addition to the well-known long-time diffusivity the motion at the shortest experimentally accessible timescales ($\dot{\gamma}\Delta t < 0.10$) is also of diffusive nature.

This phenomenon has not been observed before.

Our data over the entire range of time could be characterized very well by means of an empirical model. The model was chosen in such a way that a minimum of physically meaningful parameters was sufficient to describe the data, i.e. two dimensionless diffusion coefficients –$\hat{D}_0$ and $\hat{D}_\infty$–, two transition times –$\hat{\tau}_0$ and $\hat{\tau}_\infty$– and an unimportant, but physically meaningful parameter c_4.

The long-time diffusion coefficient $\hat{D}_\infty$ exhibits a peculiar dependence on volume fraction: up to $\phi = 0.35$ it strongly increases, above this volume fraction $\hat{D}_\infty$ levels off and even has the tendency to go down at 0.50. Experimentally this behaviour has been reported before (chapter 3, Phan & Leighton (1993)) with two different techniques. However, because of contradictory numerical and theoretical results, its origin is still subject of discussion. The characteristic onset of long-time diffusion, $\hat{\tau}_\infty$ (for definition see figure 4.7), is more or less constant within the experimental errors at a value $\tau \approx 1$ –expressed in strain units– as would be expected from a phenomenon driven by particle interactions in shear flow.

The short-time diffusive process was described by the diffusion coefficient $\hat{D}_0$, which is significantly smaller than $\hat{D}_\infty$ and increases with ϕ. We have no unambiguous interpretation of this quantity, but the underlying displacements occur on a timescale on which the configuration of neighbouring particles has not changed. The timescale of this diffusive process is much shorter, $\hat{\tau}_0 \ll \hat{\tau}_\infty$, and quantitatively the values of $\hat{\tau}_0$ are in agreement with the concept of 'caging' at short times. At longer times, direct hydrodynamic interactions with neighbouring particles lead to larger displacements and the long-time self-diffusion becomes dominant.

In controlled stress oscillatory experiments a strong dependence of the (apparent) relative dynamic viscosity η'_r on the strain amplitude γ_0 was noticed. At high strain values ($\gamma_0 \gg 1$) a well-defined plateau of η'_r exists and a much lower plateau was found for small amplitudes (γ_0). The difference between the two plateaus was attributed to shear-induced structure at high deformations, when particles are driven closely together, thus giving rise to an extra contribution to the viscosity. The structure is generally characterized by the pair-distribution function $g_2(\mathbf{r})$ in the thin boundary layer around the particle (e.g. Brady & Morris (1997)). During low strain oscillations this structure related viscosity contribution disappeared, leaving a lower η'_r plateau which coincides perfectly with the high frequency (and thus low strain) limit $\eta'_{\infty,r}$ as observed in Brownian suspensions (Van der Werff *et al.*, 1989). This correspondence suggests that even in non-colloidal suspensions the boundary layer is rapidly destroyed after cessation of flow. According to the theoretical scaling of Brady & Morris (1997), the small residual Brownian force would be sufficient to eliminate the extremely thin boundary layer structure, so that the boundary layer

reaches equilibrium almost instantly. The distribution of particles outside the boundary layer is apparently less important for the high frequency limit of η_r'. In non-colloidal suspensions the particle distribution outside the boundary layer does not reach equilibrium during oscillatory measurements.

References

ACRIVOS, A. 1995 Shear-induced particle diffusion in concentrated suspensions of non-colloidal particles. *J. Rheol.* **39** (5), 813–826.

BRADY, J.F. & BOSSIS, G. 1988 Stokesian dynamics. *Ann. Rev. Fluid Mech.* **20**, 111–157.

BRADY, J.F. & MORRIS, J.F. 1997 Microstructure of strongly sheared suspensions and its impact on rheology and diffusion. *J. Fluid Mech.* **348**, 103–139.

CROSS, M.M. 1965 Rheology of non-Newtonian fluids: a new flow equation for pseudoplastic systems. *J. Colloid Sci.* **20**, 417–437.

DA CUNHA, F.R. & HINCH, E.J. 1996 Shear-induced dispersion in a dilute suspension of rough spheres. *J. Fluid Mech.* **309**, 211–223.

DAVIS, R.H. 1996 Hydrodynamic diffusion of suspended particles: a symposium. *J. Fluid Mech.* **310**, 325–335.

ECKSTEIN, E.C. , BAILEY, D.G. & SHAPIRO, A.H. 1977 Self-diffusion of particles in shear flow of a suspension. *J. Fluid Mech.* **79**, 191–208.

FOSS, D.R. & BRADY, J.F. 1999 Self-diffusion in sheared suspensions by dynamic simulation. *J. Fluid Mech.* **401**, 243–274.

GADALA-MARIA, F. & ACRIVOS, A. 1980 Shear-induced structure in a concentrated suspension of solid spheres. *J. Rheol.* **24** (6), 799–814.

GONDRET, P. , PETIT, L. & BOSSIS, G. August 18-23, 1996 Static and dynamic viscosity of macroscopic suspensions of solid spheres. In *Proc. of the XIIth Int. Conf. Rheology* (ed. A. Ait-Kadi, J.M. Dealy, D.F James & M.C. Williams), pp. 554–555. Quebec City (Quebec): Laval University.

JONGSCHAAP, R.J.J. & MELLEMA, J. 1995 Stress tensor expressions for dispersions. *J. Rheol.* **39** (5), 953–959.

KNIPMEYER, K.M. & PINE, D.J. 2000 personal communication.

LEIGHTON, D. & ACRIVOS, A. 1987a Measurement of shear-induced self-diffusion in concentrated suspensions of spheres. *J. Fluid Mech.* **177**, 109–131.

LEIGHTON, D. & ACRIVOS, A. 1987b The shear-induced migration of particles in concentrated suspensions. *J. Fluid Mech.* **181**, 415–439.

MORRIS, J.F. 2000 personal communication.

PESCHE, R. 1998 Etude par simulation numerique de la segregation de particules dans une suspension bidisperse. PhD thesis, Universite de Nice-Sophia Antipolis, France.

PHAN, S.E. & LEIGHTON, D.T. 1993 Measurement of the shear-induced tracer diffusivity in concentrated suspensions. *J. Fluid Mech.* **submitted**.

SHIKATA, T. & PEARSON, D. 1994 Viscoelastic behavior of concentrated spherical suspensions. *J. Rheol.* **38** (3), 601–616.

WANG, Y. , MAURI, R. & ACRIVOS, A. 1996 The transverse shear-induced liquid and particle tracer diffusivities of a dilute suspension of spheres undergoing a simple shear flow. *J. Fluid Mech.* **327**, 255–272.

VAN DER WERFF, J.C. , DE KRUIF, C.G. , BLOM, C. & MELLEMA, J. 1989 Linear viscoelastic behaviour of dense hard-sphere dispersions. *Phys. Rev. A* **39**, 795–807.

ZARRAGA, I.E. , HILL, D.A. & LEIGHTON, D.T. 2000 The characterisation of the total stress of concentrated suspensions of noncolloidal spheres in Newtonian fluids. *J. Rheol.* **44** (2), 185–220.

Chapter 5

Measuring the Full Diffusion Tensor of Shear-Induced Self-Diffusion

Abstract

The full tensor of shear-induced self-diffusion is studied experimentally for concentrated suspensions of non-colloidal hard spheres. A new approach for data analysis is presented, which enables to extract all components of the diffusion tensor. In previous studies only the components in the velocity gradient and vorticity direction could be measured, $\hat{D}_{yy}$ and $\hat{D}_{zz}$. The method is an extension of the spatial correlation technique devised in chapter 2. The main feature of the advanced method is the removal of large affine particle displacements due to the macroscopic shear flow, so that small diffusive displacements can be detected. Experimental data are fitted directly to the theoretical transition probability distribution. Evaluation of the evolution of the fit parameters with strain $\dot{\gamma}\Delta t$ makes it possible to identify the range of $\dot{\gamma}\Delta t$ where the particle motion is diffusive. In this regime for the first time shear-induced diffusion in the velocity direction $\hat{D}_{xx}$ and for the off-diagonal component $\hat{D}_{xy}$ could be measured. The off-diagonal component was found to be negative. Both $\hat{D}_{xx}$ and $\hat{D}_{xy}$ seem to be independent of volume fraction. $\hat{D}_{xx}$ is an order of magnitude larger than diffusion in the other directions.

5.1 Introduction

Suspensions are widely used in industry, e.g. slurries for transportation of solid particulate materials, paints, pastes, food. Fundamental understanding of their complex properties has therefore been the aim of many studies. In addition to macroscopic properties like suspension viscosity and sedimentation velocities, shear-induced diffusion is one of the basic transport phenomena in concentrated non-colloidal suspensions under flow.

Shear-induced diffusion is the result of interactions between neighbouring particles: in concentrated suspensions under flow, particles on adjacent streamlines are forced by the bulk flow to overtake each other. In very dilute suspensions the hydrodynamic interactions can essentially be treated as two-particle interactions which are symmetrical in low Reynolds number flow. However, in concentrated suspensions this symmetry is broken and the interactions lead to net particle displacements of random nature which can be characterized as shear-induced self-diffusion.

Experimental observations of shear-induced particle diffusion in neutrally buoyant suspensions date back to Eckstein *et al.* (1977), who noticed that in Couette flow particles exhibit fluctuating motion. The Reynolds number of the flow was very low and the particles were non-colloidal. Under these circumstances, the more familiar phenomena of Brownian (thermally driven) and turbulent (inertially driven) diffusion can be neglected. Nevertheless the particle motion is chaotic and can be characterized as self-diffusion. The subject has been under renewed attention since the experimental work of Leighton & Acrivos (1986, 1987a,b).

In addition to self-diffusion measurements it was also shown that in case of inhomogeneities in shear rate and/or particle volume fraction shear-induced diffusion can lead to macroscopic migration. For example, a sediment layer of non-colloidal particles will be resuspended by applying shear flow (Leighton & Acrivos, 1986). In Couette rheometry shear-induced diffusion can lead to the migration of particles out of the annular gap into the stagnant reservoir underneath the bob. The decreased particle concentration in the annulus leads to underestimating the suspension viscosity (Leighton & Acrivos, 1987b).

In this paper we focus on self-diffusion, since we consider it to be the basic microscopic mechanism behind all shear-induced diffusion phenomena. Detailed knowledge about the behaviour of self-diffusion will be crucial for understanding particle motion on the microscopic level and thereby capturing the essential features of the associated macroscopic transport processes. In particular we will aim for the experimental determination of the full shear-induced self-diffusion tensor.

Experimental work on self-diffusion has up till now focused on the determination of diffusivities in the velocity gradient and vorticity direction, resp. D_{yy} and D_{zz}, since these are the easiest to measure. The technique employed by Eckstein *et al.* (1977); Leighton & Acrivos (1987a); Phan & Leighton (1993) is based on measuring the

passage time and/or axial position of an opaque tracer particle in a refractive index matched concentrated suspension after each full rotation in a Couette cell. Fluctuations in the passage time can be linked to the diffusion coefficient in the velocity gradient direction (usually referred to as $y-$axis), because in Couette flow the rotational velocity directly depends on the tracer $y-$position. In addition, the axial tracer position (Phan & Leighton, 1993) provide information about diffusion on the vorticity direction (z). Since the method is based on full rotations of tracers in a Couette cell, the observation time cannot be controlled externally and the accessible range of timescales is limited to relatively large strain values (the strain $\dot{\gamma}\Delta t$ representing the relevant dimensionless time of the experiments).

In chapter 2 and 3 we have developed a novel technique that is suitable for monitoring the particle displacements over a range of strain values. The technique is based on spatial correlation of tracer positions in a large set of video images. In a concentrated suspension the majority of particles are refractive index matched with the suspending fluid so that a small fraction of coloured tracer particles (typically 0.3% volume fraction) can be visualized with standard optics. Video images can be recorded with a digital camera and analyzed with image analysis software. Although the technique has so far only been applied to measure the diffusion coefficients D_{yy} and D_{zz} in respectively the velocity gradient and vorticity direction, it is capable of determining other components of the diffusion tensor, D_{xx} and D_{xy}, as will be shown in this paper. The data analysis requires significant calculational effort, as will be discussed in section 5.2. Experimental details are described in section 5.3, where a detailed example of the data analysis will be shown. The results will be presented and discussed in section 5.4. Before drawing conclusions in the final section, our results will also be compared to the recent numerical data of by Foss & Brady (1999).

5.2 Theory

In this section we will show how the data analysis of the correlation technique as described in detail in chapter 2 can be extended to extract the elements of the shear-induced self-diffusion tensor that have not yet been determined experimentally: the diffusivity in the velocity direction, D_{xx}, and the off-diagonal component D_{xy}.

5.2.1 The diffusion tensor

The shear-induced self-diffusion tensor $\mathbf{D}$ can be defined by the standard diffusion relation:

$$\langle \Delta\mathbf{x}\, \Delta\mathbf{x} \rangle \sim 2\, \mathbf{D}\, \Delta t \tag{5.1}$$

where $\Delta\mathbf{x}$ denotes the diffusive particle displacement vector and $\langle\rangle$ the ensemble average over an ensemble of macroscopically identical systems for the given flow geometry and boundary conditions.

Based on dimensional analysis, the shear-induced self-diffusion tensor $\mathbf{D}$ must scale like:

$$\mathbf{D} = \dot{\gamma}\, a^2\, \hat{\mathbf{D}}(\phi) \tag{5.2}$$

because the only relevant timescale in a concentrated non-colloidal suspension is the inverse shear rate $1/\dot{\gamma}$ and all length scales in the system must depend on the particle radius a. The dimensionless tensor $\hat{\mathbf{D}}$ is then only a function of dimensionless parameters of which the particle volume fraction ϕ is the most important one (Eckstein *et al.*, 1977). In principle other dimensionless numbers could still play a role, like Péclet number (Pe) and relative size of particles compared to the geometry, a/L (L being the gap width), but previous experiments on shear-induced self-diffusion have not produced evidence for such influences (chapter 2, Eckstein *et al.* (1977); Leighton & Acrivos (1987a); Phan & Leighton (1993)).

$\mathbf{D}$ is shear-induced and is therefore –in analogy to the stress tensor in viscometric flows– an isotropic tensor function $\mathbf{D} = f(\mathbf{L})$ of the velocity gradient tensor $\mathbf{L} = \dot{\gamma}\, \mathbf{e}_x\mathbf{e}_y$, which itself is an isotropic function of the vectors $\mathbf{e}_x$ and $\mathbf{e}_y$ that span the viscometric flow. Here $\mathbf{e}_x$ denotes the velocity direction and $\mathbf{e}_y$ the velocity gradient direction. According to a representation theorem for isotropic functions $\mathbf{D}$ can then be written as

$$\mathbf{D} = \alpha_0(\dot{\gamma})\, \mathbf{I} + \alpha_1(\dot{\gamma})\, (\mathbf{e}_x\mathbf{e}_x) + \alpha_2(\dot{\gamma})\, (\mathbf{e}_y\mathbf{e}_y) + \alpha_3(\dot{\gamma})\, (\mathbf{e}_x\mathbf{e}_y + \mathbf{e}_y\mathbf{e}_x) \tag{5.3}$$

Combining equation 5.2 and 5.3 leads to the following form of the self-diffusion tensor:

$$\mathbf{D} = \dot{\gamma}\, a^2\, \hat{\mathbf{D}} = \dot{\gamma}\, a^2 \begin{bmatrix} \hat{D}_{xx} & \hat{D}_{xy} & 0 \\ \hat{D}_{xy} & \hat{D}_{yy} & 0 \\ 0 & 0 & \hat{D}_{zz} \end{bmatrix} \tag{5.4}$$

The representation theorem does not prove that the four remaining diffusion components in equation 5.4 differ from zero. It only shows that based on symmetry considerations only these components can be of physical importance.

The interpretation of the diagonal components ($\hat{D}_{xx}$, $\hat{D}_{yy}$, $\hat{D}_{zz}$) is straightforward: these components represent anisotropic diffusion in the various flow directions. In a sheared suspension, such anisotropy seems reasonable because of the distinct character of the three directions. The off-diagonal component $\hat{D}_{xy}$ is more difficult to interpret. Equation 5.1 shows that this component is the result of correlations between the displacements in the flow direction, Δx, and in the velocity gradient direction, Δy, thus leading to a non-zero $\langle \Delta x\, \Delta y \rangle$. Foss & Brady (1999) provide an explanation for

the sign and magnitude of $\hat{D}_{xy}$ over a wide range of Péclet numbers. For our non-colloidal suspensions only the case of extremely high Péclet numbers is of interest. The concept of Foss & Brady (1999) is repeated here in a simplified mechanistic framework, which we believe to be of assistance for understanding the nature and origin of $\hat{D}_{xy}$.

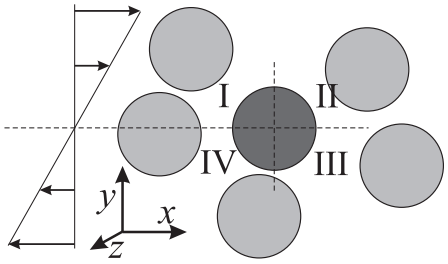

Figure 5.1: Particles interacting in the $x-y-$plane of simple shear flow.

Figure 5.1 displays suspended particles in simple shear flow, the central particle being located at the stationary velocity plane so that its position is unchanged by the shear flow. The central particle experiences an influx of neighbouring particles in the compressive quadrants I and III, whereas in quadrants II and IV neighbouring particles are being pulled away by the flow. Every particle that "collides" with the central particle in quadrant I will encounter a positive Δy displacement. In addition, its motion in the velocity direction will be hindered, causing a negative displacement Δx in comparison with the undisturbed trajectory. For particles in quadrant III, $\Delta y < 0$ and $\Delta x > 0$. In principle, particle motions in the quadrants II and IV would generate positive values of $\Delta x \cdot \Delta y$, but as a result of the flow asymmetry there is an increased probability of near contact in the compressional quadrants I and III so that averaging over all particle configurations results in a negative value of $\langle \Delta x \, \Delta y \rangle$ and a diffusive component $\hat{D}_{xy} < 0$.

Within the same framework it can easily be seen that the other off-diagonal components must be zero, as was already shown by the representation theorem. Consider for example $\hat{D}_{yz}$: interactions in quadrant I lead to positive Δy displacements, but the sign of Δz depends on the $z-$coordinate of the colliding particle. Particles behind the x-y-plane sketched in figure 5.1 will experience $\Delta z < 0$ and particles in front of that plane $\Delta z > 0$. Because of the symmetry of the flow with respect to the plane of shear, these contributions cancel out in the ensemble average $\langle \Delta y \, \Delta z \rangle$. The concept can also be used to explain the observations of negative D_{xy} in granular shear flows (Campbell, 1997), where in absence of hydrodynamics the mechanistic picture is applicable even more directly.

5.2.2 Influence of shear flow

The expressions in the preceding subsection are oversimplified in the sense that particles in shear flow not only experience diffusive displacements. They are also subjected to the macroscopic flow. The influence of the affine flow on the appearance of shear-induced diffusion in experimental situations is examined in this section.

Following the definitions presented in chapter 2, we define the transition probability $P^{trans}(\Delta\mathbf{x};\Delta t,\mathbf{x})$ which represents the probability for a tracer particle to be displaced over a vector $\Delta\mathbf{x}$ during a time interval Δt, starting from position $\mathbf{x}$. Under the assumption that shear-induced diffusion is a purely diffusive motion superimposed on affine motion with the macroscopic shear flow, the evolution of the transition probability P^{trans} is given by the convective diffusion equation:

$$\frac{\partial P^{trans}}{\partial t} = -\nabla\cdot(\mathbf{v}\,P^{trans}) + \nabla\cdot\mathbf{D}\cdot\nabla P^{trans} \tag{5.5}$$

with initial condition $P^{trans}(\Delta\mathbf{x};0,\mathbf{x}_0) = \delta(\Delta\mathbf{x})$, requiring all particles to start at their initial position $\mathbf{x}_0$. The bulk velocity is represented by $\mathbf{v}$. For stationary simple shear flow $\mathbf{v} = \mathbf{L}\cdot\mathbf{x} + v_0\,\mathbf{e}_x$, where v_0 is a translational velocity that determines the location of the stationary plane.

The solution of equation 5.5 can be obtained (see e.g. Chandrasekhar, 1943; van Kampen, 1992):

$$P^{trans}(\Delta\mathbf{x};\mathbf{x},\Delta t) = \frac{1}{(2\pi)^{3/2}\sigma_x\sigma_y\sigma_z}\cdot\exp\left(-\frac{\delta^2}{2\sigma_x^2} - \frac{(\Delta y)^2}{2\sigma_y^2} - \frac{(\Delta z)^2}{2\sigma_z^2}\right) \tag{5.6}$$

with

$$\delta = \Delta x - \Delta y\frac{D_{xy}}{D_{yy}} - \dot\gamma\Delta t\left(y + \frac{\Delta y}{2}\right) - v_0\Delta t \tag{5.7}$$

and

$$\begin{aligned}
\sigma_x^2 &= 2\,\Delta t\,\left(D_{xx} + \tfrac{1}{12}(\dot\gamma\Delta t)^2\,D_{yy} - \frac{D_{xy}^2}{D_{yy}}\right),\\
\sigma_y^2 &= 2\,\Delta t\,D_{yy},\\
\sigma_z^2 &= 2\,\Delta t\,D_{zz}
\end{aligned} \tag{5.8}$$

The expressions for δ and σ_x^2 show that the particle displacements in the velocity direction, as described in the first term of equation 5.6 are affected by the convective shear flow and the diffusive coupling term D_{xy}. Both numerator and denominator reflect this coupling effect.

The transition probability P^{trans} describes the statistical distribution of particle displacements. Within the framework of the experimental correlation technique of chapter 2 they can be related to auto-correlation vectors, which also reflect the motion of individual tracer particles. The temporal evolution of the Gaussian distribution of equation 5.6 can then be used to evaluate experimental data and measure self-diffusion coefficients. For diffusion components D_{yy} and D_{zz} this is relatively straightforward, since these components can be extracted relatively easily (see chapter 2 and 3). The displacements in the velocity direction are affected by the shear flow, which depends on the initial particle position $\mathbf{x}$ (equation 5.7), so that the experimental analysis of the diffusion coefficients D_{xx} and D_{xy} is complicated considerably.

5.2.3 Distribution under experimental conditions

The first challenge is to find a relation between the experimentally observed distribution of correlation vectors and the theoretical prediction of equation 5.6 so that the diffusion coefficients D_{xx} and D_{xy} can be determined. For the other components D_{yy} and D_{zz} such a method has been described and applied in chapter 2 and 3. For completeness and clarity, part of the mathematics in those papers is repeated here to pave the way for more advanced analysis steps required to measure D_{xx} and D_{xy}.

Relating the experimental results –a large set of correlation vectors between tracer positions in subsequent video images– to the theoretical predictions of the previous section entails a number of specific problems. In the first place, the experimental technique is unable to identify individual particles in subsequent images. Therefore the correlation procedures not only yield auto-correlation vectors that represent the displacements of individual particle, but it also generates cross-correlation vectors between different particles. As a result, the total probability of finding a correlation vector $\Delta\mathbf{x}$ after interval Δt in the system volume V needs to be written as:

$$\Gamma(\Delta\mathbf{x},\Delta t) = \int_V \sum_i \left(P_1(\mathbf{x}) \cdot \left[P^{trans}(\Delta\mathbf{x};\mathbf{x},\Delta t) + \sum_{j\neq i} \frac{1}{V} P_2(\mathbf{x}+\Delta\mathbf{x};\mathbf{x},\Delta t) \right] \right) d^3\mathbf{x} \quad (5.9)$$

where both summations take place over all i tracer particles in the system. $P_1(\mathbf{x})$ denotes the chance of finding a tracer particle at position $\mathbf{x}$. P^{trans} is the probability that this specific tracer particle has experienced a displacement $\Delta\mathbf{x}$ during the time step Δt, whereas $P_2(\mathbf{x}+\Delta\mathbf{x};\mathbf{x},\Delta t)$ is the conditional probability that *another* particle is located at $\mathbf{x}+\Delta\mathbf{x}$ provided that the first tracer was at $\mathbf{x}$ a time Δt earlier. The conditional probability P_2 can be expressed in P^{trans} and the pair distribution function $g_2(\mathbf{r})$, which describes the chance of finding two particles a distance $\mathbf{r}$ apart within the same image:

$$P_2(\mathbf{x}+\Delta\mathbf{x};\mathbf{x},\Delta t) = \int_V P^{trans}(\mathbf{x}+\Delta\mathbf{x}-\mathbf{x}';\mathbf{x}',\Delta t) \cdot g_2(\mathbf{x}'-\mathbf{x})\, d^3\mathbf{x}' \quad (5.10)$$

The integrand represents the joint possibility of the secondary particle to be located at position $\mathbf{x}'$ initially and then making a transitional step towards $\mathbf{x}+\Delta\mathbf{x}$ during interval Δt.

For a homogeneous suspension $P_1(\mathbf{x}) = 1/V$ is constant and equation 5.9 reduces to:

$$\Gamma(\Delta\mathbf{x},\Delta t) = \int_V \left[n\, P^{trans}(\Delta\mathbf{x};\mathbf{x},\Delta t) + n^2\, P_2(\mathbf{x}+\Delta\mathbf{x};\mathbf{x},\Delta t)\right] d^3\mathbf{x} \tag{5.11}$$

with n the particle number density.

In addition to the mixing of auto- and cross-correlations, the experimental technique has another important limitation. It only provides two-dimensional images that are projections of a three-dimensional imaging volume, while the preceding equations describe the unbounded three-dimensional space. The observed volume is bounded by the size of the CCD chip, the magnification of the camera optics and the focal depth of the optical system. Moreover, image analysis procedures which identify positions of tracer particles are imperfect. Therefore not every tracer particle within the image volume will be detected. All these effects have implications for the experimentally observed distribution of displacement vectors and the associated analysis steps. When describing the correlation technique in chapter 2, we have introduced some mathematical tools to account for these effects.

The detection probability of a tracer particle that resides at a position $\mathbf{x}$ is expressed by a function $S(\mathbf{x})$. In contrast to our previous work where we implemented the boundaries of imaging volume by adjusting the limits of integration in equation 5.11, here we introduce the rectangular shape function $\Pi(u)$, which gives the same result:

$$\Pi(u) = \begin{cases} 1 & 0 < u < 1 \\ 0 & \text{elsewhere} \end{cases} \tag{5.12}$$

We now introduce the function C_{3D} to represent the experimental three-dimensional distribution of correlation vectors within the limited imaging volume V_{im} bounded by $0 < x < W_x$, $0 < y < W_y$ and $0 < z < W_z$. Then equation 5.11 can be written as:

$$C_{3D}(\Delta\mathbf{x};\Delta t) = \int_V \mathbb{S}(\mathbf{x})\,\mathbb{S}(\mathbf{x}+\Delta\mathbf{x})\left[n\, P^{trans}(\Delta\mathbf{x};\mathbf{x},\Delta t) + n^2\, P_2(\mathbf{x}+\Delta\mathbf{x};\mathbf{x},\Delta t)\right] d^3\mathbf{x} \tag{5.13}$$

with

$$\begin{aligned} \mathbb{S}(\mathbf{x}) &= S(\mathbf{x})\,\Pi\left(\frac{x}{W_x}\right)\,\Pi\left(\frac{y}{W_y}\right)\,\Pi\left(\frac{z}{W_z}\right) \\ \mathbb{S}(\mathbf{x}+\Delta\mathbf{x}) &= S(\mathbf{x}+\Delta\mathbf{x})\,\Pi\left(\frac{x+\Delta x}{W_x}\right)\,\Pi\left(\frac{y+\Delta y}{W_y}\right)\,\Pi\left(\frac{z+\Delta z}{W_z}\right) \end{aligned} \tag{5.14}$$

Once the viewing direction of the optical system has been chosen, one of the three dimensions is lost as a result of projecting the image volume on the two dimensional plane of the CCD chip. Equation 5.13 can then be evaluated in more detail. In this paper we specifically aim for the retrieval of the diffusion coefficients D_{xx} and D_{xy}. To this purpose the observations must be made along the $z-$axis, so that the plane of view is the $x-y-$plane (plane of shear). The dimensions W_x and W_y are then set by the size (resp. width and height) of the CCD chip and the magnification. W_z represents the "depth of focus" of the camera optics: the plane of focus is located at $z = \frac{1}{2}W_z$ and particles out of focus by more than $\frac{1}{2}W_z$ cannot be observed. Under these circumstances it can be assumed that the detection probability $S(\mathbf{x})$ has the following form:

$$S(\mathbf{x}) = S_{\parallel}(z)\, S_{\perp}(x,y) = \lambda \cdot\ S_{\parallel}(z) \tag{5.15}$$

where λ is an $O(1)$ constant, since for homogeneous illumination the tracer detection efficiency over the $x-y-$plane should be constant and close to unity. Parallel to the viewing direction, the detection efficiency $S(z)$ varies strongly, being maximal –and close to unity– at the focal plane $z = \frac{1}{2}W_z$ and decreasing towards zero near the boundaries of the imaging volume, for $z = 0$ and W_z.

When viewing along the $z-$axis, only vectors $(\Delta x, \Delta y)$ can be observed by the CCD camera. Within the mathematical framework this is equivalent to integrating $C_{3D}(\Delta\mathbf{x};\Delta t)$ over the variable Δz:

$$C_{2D}(\Delta x, \Delta y;\Delta t) = \int C_{3D}(\Delta\mathbf{x};\Delta t)\, d\Delta z \tag{5.16}$$

By further reducing equation 5.16 and integrating over the velocity direction (Δx), D_{yy} can be retrieved directly (chapter 2). In this chapter, however, we are interested in the displacement component Δx along the velocity axis and the distribution is kept in its current form.

$C_{2D}(\Delta x, \Delta y;\Delta t)$ is the theoretical description of an experimental distribution of correlation vectors. Figure 5.2 is a typical experimental example of such a distribution. The data are presented in the shape of a histogram that reflects the experimental probability $P^{exp}(\Delta x, \Delta y)$ to find a vector $(\Delta x, \Delta y)$. The set of correlation vectors was taken from a set of 8000 images at volume fraction $\phi = 0.35$ and strain value $\dot{\gamma}\Delta t = 1.10$.

Without elaborating on the details that are provided in previous chapters it is sufficient to note that the central peak in figure 5.2 consists of auto-correlation vectors. The noisy background is the result of cross-correlation contributions. The terms are separated in the integrand of equation 5.13 and the auto-correlation peak should be described by the distribution function of equation 5.6 in case of diffusive motion.

The contours of the projections of the histogram along both axes that are included in the figure clearly show that the width in the velocity direction (Δx) is orders

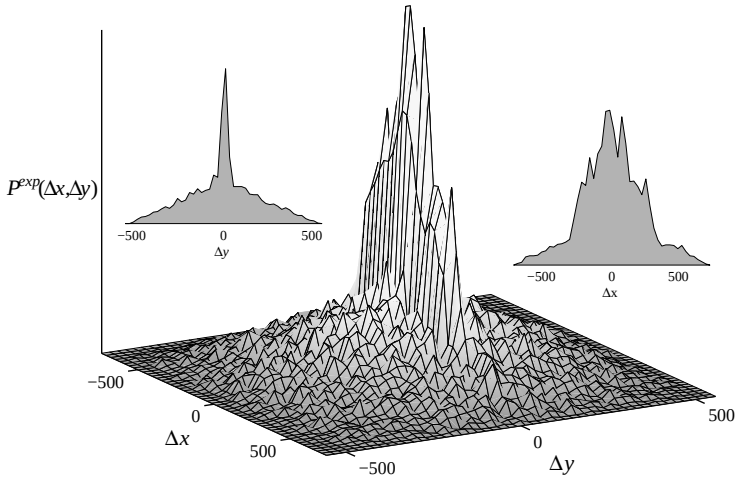

Figure 5.2: Experimental histogram of correlation vectors $(\Delta x, \Delta y)$ for an ensemble of 8000 images ($\dot{\gamma}\Delta t = 1.10$ and $\phi = 0.35$); the displacements Δx and Δy are expressed in pixels, while the probability P^{exp} has arbitrary (non-normalized) units. The contours of projections along both axes are shown as well.

of magnitude larger than in the velocity gradient direction (Δy). The resolution of the histogram is barely enough to capture the shape of the peak in the $y-$direction while the shape in the $x-$direction is very smooth. Returning to equation 5.6 and 5.7, one can see that the displacements in the velocity direction are smeared out by variations in the macroscopic velocity field $\mathbf{v}(y)$ within the plane of shear, while the displacements in the $y-$direction are purely the result of diffusion. However, also in the velocity direction we would like to retrieve the relatively small effects of shear-induced diffusion. In the next subsection an approach will be presented to remove the convective displacements of the shear flow in order to detect diffusion.

5.2.4 Coordinate transformation

The first exponential term of the transition probability P^{trans} in equation 5.6 is a function of the initial position $\mathbf{x}$, in particular the vertical position y. In our experimental observations this obscures diffusion effects along the flow axis. Moreover, it also makes direct comparison of the theoretical and experimental data mathematically complex since the integrand in equation 5.13 depends on $\mathbf{x}$ as well. Looking at the expression for P^{trans} a coordinate transformation seems the natural way to resolve the explicit dependence on y:

$$\Delta\mathbf{x} \rightarrow \mathbf{u} = \Delta\mathbf{x} - \left[\dot{\gamma}\Delta t \left(y + \tfrac{1}{2}\Delta y\right) + v_0\,\Delta t\right]\,\mathbf{e}_x \tag{5.17}$$

where the displacement $\Delta\mathbf{x} = (\Delta x, \Delta y, \Delta z)$ is transformed to $\mathbf{u} = (\xi, \eta, \zeta)$.

The transformation is equivalent to adjusting the positions of a tracer particle before and after the displacement step, at the respective positions $\mathbf{x}$ and $\mathbf{x}+\Delta\mathbf{x}$, in the following way:

$$\begin{aligned} \mathbf{x} \rightarrow \tilde{\mathbf{x}} &= \mathbf{x} + \tfrac{1}{2}\,\mathbf{v}(y)\,\Delta t = \mathbf{x} + \tfrac{1}{2}\,[\dot{\gamma}\,y + v_0]\,\Delta t\,\mathbf{e}_x \\ \mathbf{x}+\Delta\mathbf{x} \rightarrow \tilde{\mathbf{x}}+\mathbf{u} &= \mathbf{x}+\Delta\mathbf{x} - \tfrac{1}{2}\,\mathbf{v}(y+\Delta y)\,\Delta t = \mathbf{x}+\Delta\mathbf{x} - \tfrac{1}{2}\,[\dot{\gamma}\,(y+\Delta y) + v_0]\,\Delta t\,\mathbf{e}_x \end{aligned} \tag{5.18}$$

The adjustment can be interpreted as the application of local corrections for the affine shear flow at both ends of the displacement vector. Experimentally, the transformation of equation 5.17 can thus be performed relatively easily. A list of particle positions in all the images is available, from which correlation vectors are calculated. If the parameters $\dot{\gamma}$ and v_0 are known, the particle positions can be subjected to the transformation of equation 5.18 before calculating the correlation vectors.

The proposed coordinate transformation is not unique: other transformations could be chosen to remove the dependence on y. Regarding our experimental conditions, however, equation 5.17 represents a logical choice. In section 5.3.2 the experimental procedures will be described using the data set of figure 5.2 as an example. First the implications for the theoretical predictions of the probability distribution must be investigated.

Application of the coordinate transformation to equation 5.6 gives the following result:

$$\tilde{P}^{trans}(\mathbf{u};\tilde{\mathbf{x}},\Delta t) = \tilde{P}^{trans}(\mathbf{u};\Delta t) = \tilde{T}_1(\xi,\eta)\cdot\tilde{T}_2(\eta)\cdot\tilde{T}_3(\zeta) \tag{5.19}$$

where the exponent has been split in the following way

$$\begin{aligned} \tilde{T}_1(\xi,\eta) &= \frac{1}{\sigma_x\sqrt{2\pi}}\,\exp\left(-\frac{(\xi-\eta\,D_{xy}/D_{yy})^2}{2\sigma_x^2}\right) \\ \tilde{T}_2(\eta) &= \frac{1}{\sigma_y\sqrt{2\pi}}\,\exp\left(-\frac{\eta^2}{2\sigma_y^2}\right) \\ \tilde{T}_3(\zeta) &= \frac{1}{\sigma_z\sqrt{2\pi}}\,\exp\left(-\frac{\zeta^2}{2\sigma_z^2}\right) \end{aligned} \tag{5.20}$$

The transformed function $\tilde{P}^{trans}(\mathbf{u};\Delta t)$ is independent of the initial particle position $\tilde{\mathbf{x}}$. It should be noticed that the splitting of the exponent is not unique. By using $\tilde{P}^{trans}$ as the appropriate weight function for the ensemble averaging, it is straightforward

to calculate the various components of equation 5.1 in the new coordinates:

$$\begin{aligned} \langle \xi\, \xi \rangle &= \sigma_x^2 + \sigma_y^2 \left(\frac{D_{xy}}{D_{yy}} \right)^2 \\ \langle \eta\, \eta \rangle &= \sigma_y^2 \\ \langle \xi\, \eta \rangle &= \frac{D_{xy}}{D_{yy}} \langle \eta\, \eta \rangle \\ \langle \zeta\, \zeta \rangle &= \sigma_z^2 \end{aligned} \tag{5.21}$$

Using the definitions of σ_x, σ_y and σ_z (eq. 5.8) this can be rewritten as:

$$\begin{aligned} \langle \xi\, \xi \rangle &= 2\,\Delta t\, D_{xx} + \tfrac{1}{12} (\dot\gamma \Delta t)^2 \langle \eta\, \eta \rangle \\ \langle \eta\, \eta \rangle &= 2\,\Delta t\, D_{yy} \\ \langle \xi\, \eta \rangle &= 2\,\Delta t\, D_{xy} \\ \langle \zeta\, \zeta \rangle &= 2\,\Delta t\, D_{zz} \end{aligned} \tag{5.22}$$

Equation 5.22 shows that in spite of subtraction of the macroscopic convective flow by means of a coordinate transformation, the displacements in the velocity and velocity gradient direction remain coupled. Physically this means that a diffusive step η in the $y-$direction automatically leads to displacements in the velocity direction. So even if the diffusion D_{xx} would be zero, tracer particles would still spread in the velocity direction due to the shear flow. The effect grows with $(\dot\gamma \Delta t)^2$ and is not of diffusive nature. Before $\langle \xi\, \xi \rangle$ can be related to the diffusion coefficient D_{xx} the second term must be subtracted.

In the work of Foss & Brady (1999) the displacements corrected for affine motion are related directly to the diffusion coefficients (see their eqn. 6). The additional term in $\langle \xi\, \xi \rangle$ due to $\langle \eta\, \eta \rangle$ does not occur. In order to understand this difference it must be noted that numerical calculations are carried out on another level of description. While our equations are derived at the Smoluchovski level, where the statistical information of macroscopical displacements is studied, the simulations are performed using the Langevin equations for very small time steps. Correction for the affine flow on the Langevin level not necessarily yields the same results as when the flow field is compensated for on the Smoluchovski level.

To enable comparison of transformed experimental histograms with the theoretical predictions of equation 5.13, the remaining functions in the integrand must be

transformed as well:

$$\begin{aligned}
\mathbb{S}(\mathbf{x}) &\rightarrow \mathbb{S}(\mathbf{x}(\tilde{\mathbf{x}})) && (5.23)\\
\mathbb{S}(\mathbf{x}+\Delta\mathbf{x}) &\rightarrow \mathbb{S}(\mathbf{x}(\tilde{\mathbf{x}})+\Delta\mathbf{x}(\mathbf{u})) && (5.24)\\
P_2(\mathbf{x}+\Delta\mathbf{x};\mathbf{x},\Delta t) &\rightarrow \int_V \tilde{P}^{trans}(\mathbf{x}+\mathbf{u}-\tilde{\mathbf{x}}';\Delta t)\cdot g_2(\tilde{\mathbf{x}}'-\tilde{\mathbf{x}})\, d^3\tilde{\mathbf{x}}' && (5.25)\\
&= \int_V \tilde{P}^{trans}(\mathbf{u}-(\tilde{\mathbf{x}}'-\tilde{\mathbf{x}});\Delta t)\cdot g_2(\tilde{\mathbf{x}}'-\tilde{\mathbf{x}})\, d^3(\tilde{\mathbf{x}}'-\tilde{\mathbf{x}}) = \tilde{P}_2(\mathbf{u},\Delta t)
\end{aligned}$$

The final step denotes a translation of the limits of integration, which is irrelevant since the domain ranges from $-\infty$ to $+\infty$. Thus the explicit $\mathbf{x}-$dependence has vanished for $\tilde{P}_2$ as well. The detection function $\mathbb{S}$ remains a function of the positions before the coordinate transformation, $\mathbf{x}$ and $\mathbf{x}+\Delta\mathbf{x}$, because the images are taken in the original coordinate system. Therefore the image boundaries and detection efficiency must be expressed in the original reference frame. C_{3D} can now be transformed and substituted into equation 5.16:

$$\begin{aligned}
&C_{2D}(\xi,\eta;\Delta t) = \\
&\int\left(\left[n\,\tilde{P}^{trans}(\mathbf{u};\Delta t)+n^2\,\tilde{P}_2(\mathbf{u},\Delta t)\right]\int\mathbb{S}(\mathbf{x}(\tilde{\mathbf{x}}))\,\mathbb{S}(\mathbf{x}(\tilde{\mathbf{x}})+\Delta\mathbf{x}(\mathbf{u}))\,d^3\tilde{\mathbf{x}}\right)d\zeta
\end{aligned} \tag{5.26}$$

Using equations 5.14 and 5.15 the second integral can be specified:

$$\begin{aligned}
&\int\mathbb{S}(\mathbf{x}(\tilde{\mathbf{x}}))\,\mathbb{S}(\mathbf{x}(\tilde{\mathbf{x}})+\Delta\mathbf{x}(\mathbf{u}))\,d^3\tilde{\mathbf{x}}\\
&=\lambda^2\int S_{\parallel}(\tilde{z})S_{\parallel}(\tilde{z}+\zeta)\,\Pi\left(\frac{\tilde{x}-\frac{1}{2}\Delta t(\dot{\gamma}\tilde{y}+v_0)}{W_x}\right)\Pi\left(\frac{\tilde{x}+\xi+\frac{1}{2}\Delta t\,(\dot{\gamma}\tilde{y}+\dot{\gamma}\eta+v_0)}{W_x}\right)\times\\
&\qquad\Pi\left(\frac{\tilde{y}}{W_y}\right)\Pi\left(\frac{\tilde{y}+\eta}{W_y}\right)\Pi\left(\frac{\tilde{z}}{W_z}\right)\Pi\left(\frac{\tilde{z}+\zeta}{W_z}\right)\,d\tilde{x}\,d\tilde{y}\,d\tilde{z}\\
&=\lambda^2\int S_{\parallel}(\tilde{z})S_{\parallel}(\tilde{z}+\zeta)\Pi\left(\frac{\tilde{z}}{W_z}\right)\Pi\left(\frac{\tilde{z}+\zeta}{W_z}\right)d\tilde{z}\;\times\\
&\qquad\int W_x\;\Pi\left(\frac{\tilde{y}}{W_y}\right)\Pi\left(\frac{\tilde{y}+\eta}{W_y}\right)\Delta\left(\frac{\xi+\frac{1}{2}\dot{\gamma}\Delta t(2\tilde{y}+\eta)+v_0\Delta t}{W_x}\right)d\tilde{y}
\end{aligned} \tag{5.27}$$

where $\Delta(x)$ is a triangular shape function:

$$\Delta(x)=\begin{cases}1-|x| & \text{for } |x|\le 1\\ 0 & \text{for } |x|>1\end{cases} \tag{5.28}$$

Defining

$$F(\xi,\eta) = \int \Pi\left(\frac{\tilde{y}}{W_y}\right) \Pi\left(\frac{\tilde{y}+\eta}{W_y}\right) \Delta\left(\frac{\xi + \frac{1}{2}\dot{\gamma}\Delta t(2\tilde{y}+\eta) + \frac{1}{2}v_0\Delta t}{W_x}\right) d\tilde{y} \qquad (5.29)$$

and using equation 5.20 the following form can be derived for $C_{2D}(\xi,\eta;\Delta t)$:

$$C_{2D}(\xi,\eta;\Delta t) = \lambda^2 W_x F(\xi,\eta)\left[n\, k_1\, \tilde{T}_1(\xi,\eta)\, \tilde{T}_2(\eta) + n^2\, k_2(\xi,\eta)\right] \qquad (5.30)$$

with

$$k_1 = \int \tilde{T}_3(\zeta) \int S_{\|}(\tilde{z})\, S_{\|}(\tilde{z}+\zeta)\, \Pi\left(\frac{\tilde{z}}{W_z}\right)\, \Pi\left(\frac{\tilde{z}+\zeta}{W_z}\right) d\tilde{z}\, d\zeta \qquad (5.31)$$

$$k_2(\xi,\eta) = \int \tilde{P}_2(\xi,\eta,\zeta;\Delta t) \int S_{\|}(\tilde{z})\, S_{\|}(\tilde{z}+\zeta)\, \Pi\left(\frac{\tilde{z}}{W_z}\right)\, \Pi\left(\frac{\tilde{z}+\zeta}{W_z}\right) d\tilde{z}\, d\zeta \qquad (5.32)$$

5.2.5 Data analysis

Equation 5.30 can be used for the analysis of experimental data, which are obtained in the form of a histogram $\tilde{P}^{exp}(\xi,\eta;\Delta t)$. $\tilde{T}_1(\xi,\eta)$ and $\tilde{T}_2(\eta)$ are known functions of the desired parameters $\hat{D}_{xx}$, $\hat{D}_{xy}$ and $\hat{D}_{yy}$. The latter has also been determined already by means of a simpler analysis technique in chapter 3. $F(\xi,\eta)$ is a known geometrical shape function and k_1 is a constant function which is independent of ξ and η. The function $k_2(\xi,\eta)$ is *a priori* unknown, but we have verified by calculations that close to the autocorrelation peak k_2 is only a weak function of the displacements and can very well be approximated as a constant. The equation then reduces to:

$$C_{2D}(\xi,\eta;\Delta t) = F(\xi,\eta)\left[A\, \tilde{T}_1(\xi,\eta)\, \tilde{T}_2(\eta) + B\right] \qquad (5.33)$$

which can be compared to the measured distribution of correlation vectors, using A, B, $\hat{D}_{xx}$, $\hat{D}_{xy}$ and $\hat{D}_{yy}$ as parameters.

The following consideration is of importance for the comparison of our experimental histograms to the full prediction of equation 5.33. The experimental distribution is available in the shape of a histogram and the choice of the numerical resolution could be of influence. The histogram value $\tilde{P}^{exp}(\xi_n,\eta_m;\Delta t)$ represents the number of vectors that are found within the range:

$$\begin{aligned} \xi_n - \tfrac{1}{2}\, w_\xi < \xi \leq \xi_n + \tfrac{1}{2}\, w_\xi \\ \eta_m - \tfrac{1}{2}\, w_\eta < \eta \leq \eta_m + \tfrac{1}{2}\, w_\eta \end{aligned} \qquad (5.34)$$

where w_ξ and w_η denote the width of the histogram bins along respectively the $\xi-$ and $\eta-$axis and thus the resolution. To minimize the influence of the bin distribution it is advisable not to compare the value of $\tilde{P}^{exp}(\xi_n,\eta_m;\Delta t)$ to the value of $C_{2D}(\xi_n,\eta_m)$

at the center of the bin, but rather to the integrated value of C_{2D} over the entire bin domain specified in equation 5.34. In particular for strongly varying functions the results are improved by this method. For example, the histogram of a Gaussian peak is generally a little wider than the analytical function. Uncorrected comparison with the theoretical function then results in overestimating the peak width. Since the shape function $F(\xi,\eta)$ in equation 5.33 must be calculated numerically anyway, it is relatively straightforward to incorporate the integration of the fit function $C_{2D}(\xi,\eta;\Delta t)$ in the data analysis. To this purpose we have used a 12 point Gaussian integration over every bin.

The numerical procedures to extract the diffusion parameters will be explained in more detail at the end of the experimental section by means of an example.

5.3 Experiments

The analysis of the diffusion components $\hat{D}_{xx}$ and $\hat{D}_{xy}$ is essentially a matter of reinterpreting experimental data that were used originally for the determination of $\hat{D}_{yy}$. Therefore we do not provide extensive information about the experimental set-up. For this we refer to chapter 3 where the original data are presented. In this section we restrict ourselves to essential information about the materials and methods. Furthermore, we illustrate the implementation of the analysis technique described in the previous section by means of an example.

5.3.1 Materials and methods

The suspensions for this study consisted of PMMA particles in a density and refractive index matched fluid mixture of demineralized water, zinc-II-chloride and Triton X-100. The fluid was measured to be Newtonian over the entire range of shear rates covered by our rheometer (up to 100 s^{-1}) at a viscosity of 3.4 Pa s (23° C). The particles (produced by ICI, class 4F, $\rho = 1.172$ g/ml, $n_D^{25} = 1.491$) were sieved repeatedly to obtain a well-defined size fraction (90 ± 15 μm) and density segregation was applied to remove the particles that included air bubbles. A small fraction was then colored black with fabric dye (Rit, CPC International) to function as tracer particles in the refractive index matched suspension. To mix the particles and the fluid, the suspensions were gently tumbled for a couple of hours. The mixing technique resulted in a perfectly homogeneous system while minimizing the inclusion of small air bubbles. After mixing the suspensions were left to rest in order to remove the inevitable air and then loaded into the rheoscope (chapter 3 and de Haas *et al.* (1998)).

The suspension was sheared in a wide radius counter-rotating Couette geometry with inner and outer radius 117.0 and 121.6 mm. The plane of shear $(x-y)$ could be observed through the suspension surface (for details see chapter 3). A digital

CCD camera (JAI, type M-10, 768x582 pixels) was mounted with standard optics to obtain the desired magnification (field of view 1.10 x 0.83 mm, particle radius $a \equiv 30.8$ pixels) and depth of focus (ca. 0.4 mm from back to front). The camera was connected to a PC with frame grabber (Matrox, type Pulsar) with dedicated software for image grabbing at video rate. In this way, sequences of up to 200 images could be obtained at controlled intervals of 40 msec (25 images/sec) and multiples thereof. Storage of the image sequence and repetition of the grabbing process allowed us to collect up to 8000 images per experimental run at fixed experimental conditions ($\dot{\gamma}\Delta t$).

The images were analyzed with commercial image analysis software (Optimas, Media Cybernetics) to extract the positions of tracer particles within the images. The resulting list of particle positions $\{(x,y)_i\}_N$ in all the N images forms the basis of our analysis procedure.

In this paper measurements will be analyzed for particle volume fractions $\phi = 0.20 - 0.50$. The applied shear rate was varied between 0.19 and 0.76 s^{-1} and the interval Δt ranged from 40 to 4000 msec, so that a wide range of $\dot{\gamma}\Delta t \approx 0.007 - 3.5$ could be probed to check the scaling with $\dot{\gamma}\Delta t$.

5.3.2 Example of analysis procedure

By means of an example we explain how the procedures that were derived in section 5.2 can be applied in practice.

The list of tracer positions $\{(x,y)_i\}_N$ can be used to calculate the correlation vectors $(\Delta x, \Delta y)$ between tracer positions in subsequent images. As shown in figure 5.2 the resulting experimental set of correlation vectors, all recorded at the same parameter values $\dot{\gamma}$ and Δt, can be presented in the form of a histogram, which represents the experimental probability $P^{exp}(\Delta x_n, \Delta y_m; \Delta t)$ to find a vector $(\Delta x, \Delta y)$ that fits into the numerical bin (n,m).

The graph also illustrated the influence of macroscopic shear flow on the distribution function. To demonstrate this effect more clearly we have plotted the data of figure 5.2 in another way. Since we have the full information about particle positions at our disposal we can investigate how the displacements in the $x-$direction depend on the mean $y-$position of the particle during the time interval Δt. Figure 5.3 presents the top view of three histograms of this type, which reflects the probability $P^{exp}(\Delta x, y_{ave}; \Delta t)$ for a tracer particle to undergo a step Δx in the velocity direction when its average $y-$position equals $y_{ave} = \frac{1}{2}(2y + \Delta y)$, where y is the initial vertical position and $y + \Delta y$ the position at the end of the interval. The lighter the colours, the higher the probability. When the data are accumulated in a $P^{exp}(\Delta \mathbf{x}; \mathbf{x}, \Delta t)-$histogram like figure 5.2, the information about the position y_{ave} is disregarded and the width in the $\Delta x-$direction reflects the sum of all affine displacements.

Since convective flow forms the major contribution to $\Delta x-$displacements, the

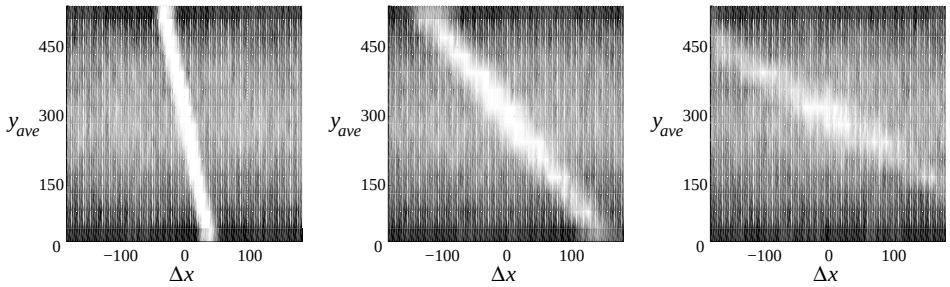

Figure 5.3: Top view of three experimental histograms of correlation vectors Δx as a function of the average $y-$position during the time interval, y_{ave}; data set is the same as for figure 5.2 and from left to right the strain values are respectively $\dot{\gamma}\Delta t = 0.14$, 0.55 and 1.10.

profiles provides information about the macroscopic shear flow. The convective displacements can simply be written as:

$$\Delta x_{ave} = \left[\dot{\gamma} y_{ave} + v_0\right] \Delta t = \left[\dot{\gamma}\left(y + \tfrac{1}{2}\Delta y\right) + v_0\right] \Delta t \tag{5.35}$$

which exactly matches the coordinate transformation of equation 5.17. The histograms of figure 5.3 indeed display this linearity and the values of $\dot{\gamma}$ and v_0 can be retrieved directly from the data by a linear fit. The accuracy of the estimated values for $\dot{\gamma}$ and v_0 is increased by making use of the fact that the correlation plots for multiple time steps (like $\dot{\gamma}\Delta t_0$, $4 \cdot \dot{\gamma}\Delta t_0$ and $8 \cdot \dot{\gamma}\Delta t_0$ in fig. 5.3) should all be described by the same parameters. Note that our geometry in combination with the reference frame of image analysis leads to negative values for the shear rate. It can also be seen that the stationary plane of our counter-rotating flow geometry is located nearly at the middle of the viewing window.

For Couette flow, theoretical predictions are available for the velocity distribution over the gap in case of Newtonian fluids, which can be compared to the experimentally determined values. The measured flow profile yielded significantly larger values for the shear rate. The effect increased with increasing volume fraction. Although we do not have a quantitative explanation for this phenomenon, deviations from the Newtonian predictions are not too surprising. In chapter 4 we have shown that non-colloidal suspensions are non-Newtonian (see also Zarraga *et al.* (2000) and Gadala-Maria & Acrivos (1980)). Moreover, in Couette flow it is well-known that particle migration occurs from the inner towards the outer cylinder. According to the predictions of Phillips *et al.* (1992) this migratory effect should not very pronounced in our narrow gap geometry. Although, the particle concentration in the middle of the gap –where our diffusion measurements are performed– should be even less affected than the concentrations at the wall, the effects on the velocity profile are unknown. Since the coordinate transformation of section 5.2.4 is very sensitive to the parameters $\dot{\gamma}$

and v_0 we have used the experimental values for the shear rate, since these accurately represent the actual shear rate in the observation window.

The equations in section 5.2 were all derived for the case of simple shear flow. However, we have used a Couette geometry. In spite of the large radius (120 mm) compared to the dimensions of the image window (height $W_y = 0.8$ mm), curvature effects could be observed, causing particle displacements of the order of a few pixels. Since we want to measure minute diffusive displacements these effects could not be neglected. In addition to curvature, there can be small errors in the camera alignment. Although the effects of curvature and misalignment on the shape function $F(\xi,\eta)$ and the cross-correlation background B in equation 5.33 are negligible, the additional particle motion leads to errors in the displacements in the $x-$direction and thus in the diffusion coefficients $\hat{D}_{xx}$ and $\hat{D}_{xy}$. In the appendix it is explained in detail how second order corrections for the streamline curvature can be made fairly easily.

Once the velocity profile is fully characterised, the route to extraction of the desired diffusion parameters proceeds now as follows. With the shear flow parameters the corrected experimental distribution of correlation vectors $\tilde{P}^{exp}(\xi_n,\eta_m;\Delta t)$ can be determined by applying the coordinate transformation of equation 5.18 before calculating the correlation vectors. Tracer particles in the first image of each correlation pair are shifted over a distance $+\frac{1}{2}\,\mathbf{v}(y)\,\Delta t$ and tracers in the second image over $-\frac{1}{2}\,\mathbf{v}(y+\Delta y)\,\Delta t$. Figure 5.4 shows the transformed histogram for the experimental data used in this example. Note the difference in scales along the displacement axes in comparison with figure 5.2. The quality of our velocity correction was verified by slightly changing the parameters and monitoring the resulting peak width in the $x-$direction. If the velocity correction deteriorates, this always leads to broadening of the auto-correlation peak. The corrections based on the fitting of figure 5.3 turned out to be very accurate.

The width in the $\xi-$direction is significantly smaller than it was in the Δx direction and is now purely the result of shear-induced diffusion. For a closer look into the diffusive displacements we have included figure 5.5 which shows the top view of the histogram in a contour plot for three different values of $\dot{\gamma}\Delta t$, the middle graph being equivalent to figure 5.4. The contours are drawn at evenly distributed levels between the background and top of the Gaussian peak. The effect of increasing noise for large strain values is evident. Although the graphs are unsuitable for quantitative analysis, they reveal important qualitative information. In the first place, it can be seen that the width in the $\xi-$direction is significantly larger than in the $\eta-$direction, which is consistent with the result of Foss & Brady (1999) that $\hat{D}_{xx} > \hat{D}_{yy}$. Secondly, the symmetry axes of the Gaussian peak are rotated relative to the $\xi-\eta-$axes, so that $\hat{D}_{xy}$ is non-zero. The direction of the rotation is in agreement with the predictions in section 5.2.1: the longest axis of the contour lines is located in the quadrant with positive values of $\xi\cdot\eta$. Taking into account that the shear flow in our experimental

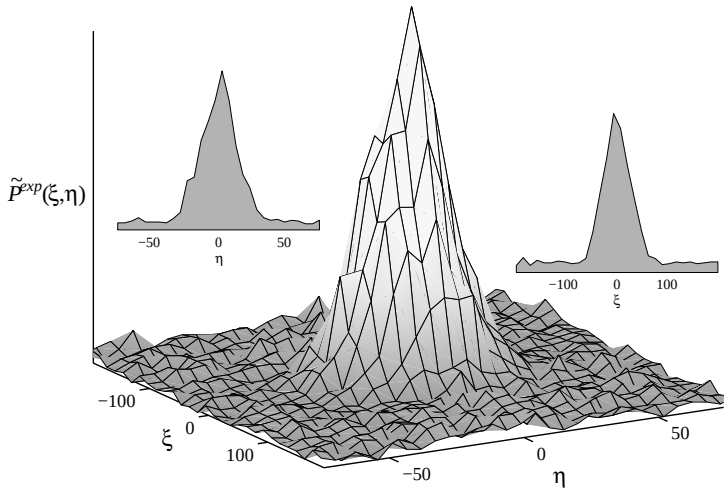

Figure 5.4: Experimental histogram of correlation vectors (ξ,η) after applying the coordinate transformation of section 5.2.4; data set is the same as for figure 5.2.

set-up is applied in the *negative* $x-$direction (see figure 5.3), this corresponds to a negative diffusion coefficient $\hat{D}_{xy}$.

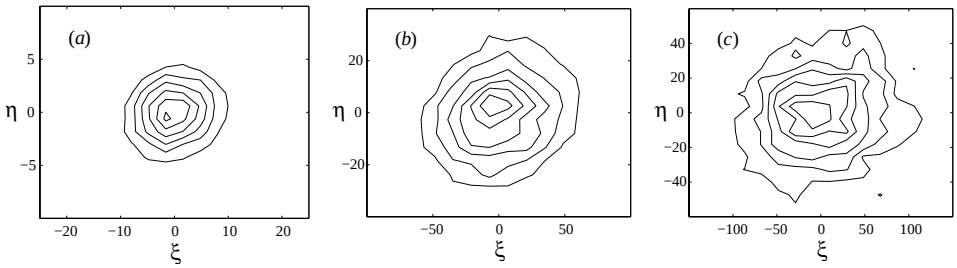

Figure 5.5: Contour plots of the corrected distribution of correlation vectors (ξ,η) for $\dot{\gamma}\Delta t = 0.14$ *(a)*, 1.10 *(b)* and 2.08 *(c)*; particle radius $a \equiv 30.8$pixels and data set is the same as for figure 5.2.

In order to extract quantitative measures for the diffusion coefficients we have to return to section 5.2, in particular to equations 5.33 and 5.8. The first step is to divide the experimental histogram by the numerically calculated shape function $F(\xi_n,\eta_m)$:

$$\frac{\tilde{P}^{exp}(\xi_n,\eta_m;\Delta t)}{F(\xi_n,\eta_m)} = A\,\tilde{T}_1(\xi_n,\eta_m)\,\tilde{T}_2(\eta_m) + B \tag{5.36}$$

where the analytical functions are integrated over the bin (n,m). The right side of the equation now provides the function to which the histogram can be fitted directly

by means of a non-linear least square fitting routine, using the Levenberg-Marquardt method (Press *et al.*, 1986):

$$\frac{\tilde{P}^{exp}(\xi_n,\eta_m;\Delta t)}{F(\xi_n,\eta_m)} = K_1 \exp\left(-\frac{(\xi_n - K_2\,\eta_m)^2}{K_3} - \frac{\eta_m^2}{K_4}\right) + K_5 \tag{5.37}$$

The fit parameters are related to the desired physical quantities in the following way (see eqn. 5.21):

$$\begin{aligned} \langle \xi\,\xi \rangle &= 0.5\,K_3 + 0.5\,K_4\,K_2^2 \\ \langle \eta\,\eta \rangle &= 0.5\,K_4 \\ \langle \xi\,\eta \rangle &= 0.5\,K_2\,K_4 \end{aligned} \tag{5.38}$$

A direct non-linear fit to these parameters was impossible. The denominator in the exponent of $\tilde{T}_1$ (eqn. 5.36) depends on all three parameters. When the full equation is used as fit function, convergence problems arise which can be circumvented by using the fit function of equation 5.37 and then applying the transformation by means of equation 5.38.

The fitting routine can be applied to histograms for different values of $\dot{\gamma}\Delta t$ and the development of the parameters with (dimensionless) time can be studied. Rewriting equation 5.22 and using the scaling of equation 5.2 one obtains:

$$\begin{aligned} \frac{1}{a^2}\left(\langle \xi\,\xi \rangle - \tfrac{1}{12}(\dot{\gamma}\Delta t)^2\,\langle \eta\,\eta \rangle\right) &= 2\,\hat{D}_{xx}\,\dot{\gamma}\Delta t \\ \frac{1}{a^2}\langle \eta\,\eta \rangle &= 2\,\hat{D}_{yy}\,\dot{\gamma}\Delta t \\ \frac{1}{a^2}\langle \xi\,\eta \rangle &= 2\,\hat{D}_{xy}\,\dot{\gamma}\Delta t \end{aligned} \tag{5.39}$$

The quantities on the left can now be plotted against the dimensionless time $\dot{\gamma}\Delta t$. In case of diffusive behaviour linear graphs are predicted. The slopes of the linear regime are a direct measure for the dimensionless diffusion coefficients $\hat{D}_{xx}$, $\hat{D}_{xy}$ and $\hat{D}_{yy}$. The advantage of the additional graphs is that the linear scaling can be verified before the data are interpreted in terms of diffusion.

5.4 Results and discussion

The operations described in the previous section were carried out for various volume fractions. It turned out that meaningful results could only be obtained for $\phi = 0.20$, 0.35 and 0.45. For the experiments at $\phi = 0.30$, 0.40 and 0.50 the data sets (number of images and number of particles per image) were too small to generate 3D histograms

(like figure 5.4) of sufficiently high quality for accurate non-linear fits. These concentrations are nicely spread over the range were intriguing effects have been observed before for $\hat{D}_{yy}$ and $\hat{D}_{zz}$, so that they can be expected to provide an decent overview of the behaviour of the other diffusion components as well.

For every volume fraction different experimental runs have been carried out and analyzed. The results for $\langle\xi\xi\rangle$, $\langle\eta\eta\rangle$ and $\langle\xi\eta\rangle$ were then averaged, using the variance of the fitted parameter as weight factor. In figure 5.6 the averaged results are shown for the three different volume fractions. In comparison to the work described in chapter 3 we have concentrated on the series for large strain values $\dot{\gamma}\Delta t$, since these data the most relevant for determining diffusion coefficients.

Figure 5.6 displays the evolution of the terms on the left side of equation 5.39. For all three figures linear regimes can be identified from which diffusion coefficients can be determined by means of a linear fit. For all volume fractions diffusion in the velocity direction occurs at larger values of $\dot{\gamma}\Delta t$. The scales of the plots reveal that $\hat{D}_{xx}$ is much larger than $\hat{D}_{xy}$ and $\hat{D}_{yy}$. This is even more pronounced in figure 5.7 which shows the diffusion coefficients as a function of particle volume fraction. For $\hat{D}_{xy}$ it must be noticed once again that due to the applied shear, positive values of $\langle\xi\eta\rangle$ correspond to a negative $\hat{D}_{xy}$.

The results can not be compared to other experimental studies. An internal check was available in the sense that values of $\langle\eta\eta\rangle$ should be equal to the results for σ_y^2 as determined from the more straightforward analysis as presented in chapter 3, since the underlying data set is the same. For each experimental run we found excellent agreement within experimental errors of the fit. In figure 5.7 we have used the results of chapter 3 for $\hat{D}_{yy}$ and $\hat{D}_{zz}$, since these data are based on more measurements and therefore more accurate.

The only external reference frame for our experimental results is formed by the recent Stokesian Dynamics calculations of Foss & Brady (1999). These authors have numerically calculated the full tensor of shear-induced self-diffusion for the first time. However, one should be careful when comparing between numerical and experimental results on shear-induced diffusion, since unresolved discrepancies still exist even for the well-known components $\hat{D}_{yy}$ and $\hat{D}_{zz}$. In particular the volume fraction dependence is qualitatively different (see e.g. Marchioro & Acrivos (2000) for a comparison). Therefore quantitative comparison of the results on the newly measured physical quantities $\hat{D}_{xx}$ and $\hat{D}_{xy}$ is not very useful. However, qualitatively, some interesting features can be found for both experimental and Stokesian Dynamics results.

Foss & Brady (1999) observe that $|\hat{D}_{xy}|$ is lower than $\hat{D}_{yy}$. At the concentration $\phi = 0.45$, for which they present numbers, these quantities are respectively -0.033 and 0.048. In our study $\hat{D}_{xy}$ is independent of ϕ within experimental errors. At $\phi = 0.45$ its value is lower than $\hat{D}_{yy}$.

Experiments and numerical results furthermore agree on a decreasing anisotropy

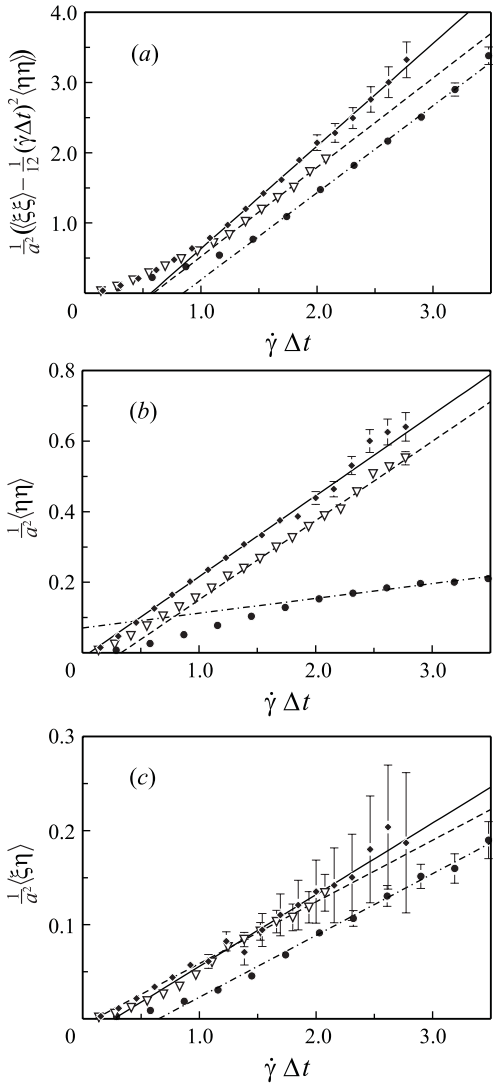

Figure 5.6: Averaged displacements (left terms of equation 5.39) as a function of dimensionless time $\dot\gamma\Delta t$ for three volume fractions $\phi = 0.20$ (●), 0.35 (▽), 0.45 (⧫); the lines represent linear fits for the determination of diffusion coefficients.

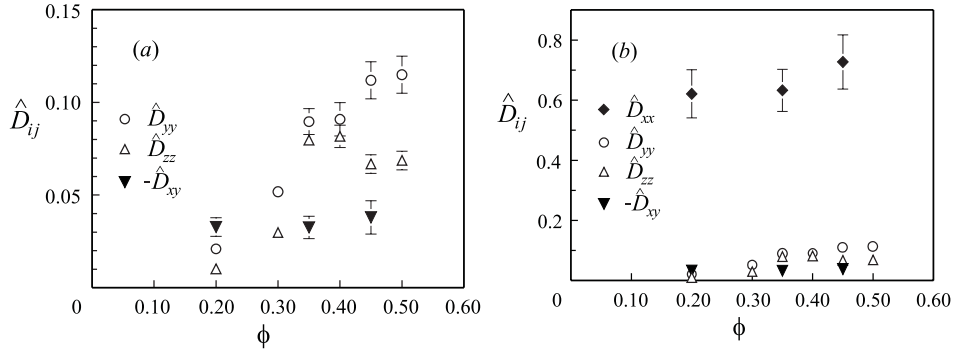

Figure 5.7: Volume fraction dependence of dimensionless diffusion coefficients of shear-induced self-diffusion; (♦) $\hat{D}_{xx}$, (▼) $-\hat{D}_{xy}$, (○) $\hat{D}_{yy}$ and (△)$\hat{D}_{zz}$, with the latter two taken from chapter 3; the two graphs show the same data on different scales.

$\hat{D}_{xx}/\hat{D}_{yy}$ with increasing concentration ϕ. However, in our experiments, $\hat{D}_{xx}$ is an order of magnitude larger than the other diffusive components, which is much higher than suggested by numerical results. All in all it can be concluded that there are striking similarities, but also unresolved quantitative differences between numerical simulations and experiments, which require further study.

5.5 Conclusions

In previous papers we have presented an experimental correlation technique which was originally developed for measuring shear-induced self-diffusion of non-colloidal suspensions of hard spheres in the velocity gradient and vorticity direction. In this paper we have shown that the technique can be used to measure the full diffusion tensor, including the two components which have so far not not been determined experimentally, $\hat{D}_{xx}$ and $\hat{D}_{xy}$. The first known experimental results for these quantities in concentrated non-colloidal suspensions are presented.

The main difficulty in the analysis procedure is to eliminate the large displacements due to the macroscopic shear flow, so that relatively small diffusive displacements can be detected. We have solved this problem by means of a coordinate transformation which is analogous to correcting the particle positions at both ends of the correlation vector for the local flow conditions. When we take into account various effects of the experimental set-up, the theoretical particle distribution, which is obtained by solving the convection-diffusion equation on the Smoluchovski level, can be fitted directly to experimental data so that statistical properties of the particle displacements can be measured. The evolution of the parameters ($\langle \xi\, \xi \rangle$, $\langle \eta\, \eta \rangle$ and $\langle \xi\, \eta \rangle$) for increasing strain values $\dot{\gamma}\Delta t$ is used to verify if the particle motion is diffusive and to calculate the diffusion coefficients.

Because of the complexity of the analysis steps it is difficult to get accurate quantitative results. Very large data sets are required. In our experiments we collected sufficiently reliable data over a long range of strain values $\dot{\gamma}\Delta t$ for three particle volume fractions: $\phi = 0.20$, 0.35 and 0.45.

Although the data are not extremely accurate in the quantitative sense, qualitatively unique observations have been done. We have found that the diffusion component in the velocity direction, $\hat{D}_{xx}$ is an order of magnitude larger than in the velocity gradient direction, $\hat{D}_{yy}$.

The component $\hat{D}_{xy}$ is negative. The sign is in agreement with the expectations for non-colloidal systems, where there is an increased concentration of particles along the compressional axis and a deficit in the extensional zone. Its value is independent of concentration and slightly lower than $\hat{D}_{yy}$ above $\phi = 0.20$.

The only reference frame for our results is formed by the recent Stokesian Dynamics calculations of Foss & Brady (1999), where the quantities have been calculated numerically for the first time. Quantitative comparison of the results on the newly measured diffusion coefficients is not very useful, because unresolved discrepancies exist between numerical and experimental work for the well-known components. However, important qualitative similarities can be identified. Foss & Brady (1999) also observed that $\hat{D}_{xy}$ is negative and that its magnitude is lower than $\hat{D}_{yy}$ for $\phi = 0.45$. In addition, experiments and numerical results agree on a decreasing anisotropy $\hat{D}_{xx}/\hat{D}_{yy}$ with increasing concentration ϕ.

Appendix A: Curvature correction for Couette flow

The curvature of a Couette geometry causes small complications in the data analysis that is described in section 5.2, especially when the viewing window is misaligned with the flow field. The misalignment can be due to small errors in the alignment with respect to the axis of rotation or even due to inaccuracy in the position of the CCD chip inside the camera. Although the effect is a higher order correction and the equations describing the particles distributions do not change significantly, it is relevant for the work in this paper, since we aim for measuring diffusion coefficients that are small compared to the convective flow displacements. This appendix contains a detailed survey of the effects of misalignment in a curved geometry.

Figure A.2 provides the reference frame for describing misalignment. In the ideal situation, the center of the viewing window O is positioned so that the $y-$axis intersects the axis of rotation. In case of misalignment, O is shifted over a distance h in the $x-$direction. H being the distance from the rotational axis to the $x-$axis, this is equivalent to an angle of misalignment θ with $\tan\theta = h/H$. Furthermore, the coordinates (x,y) define the position within the viewing window relative to its center

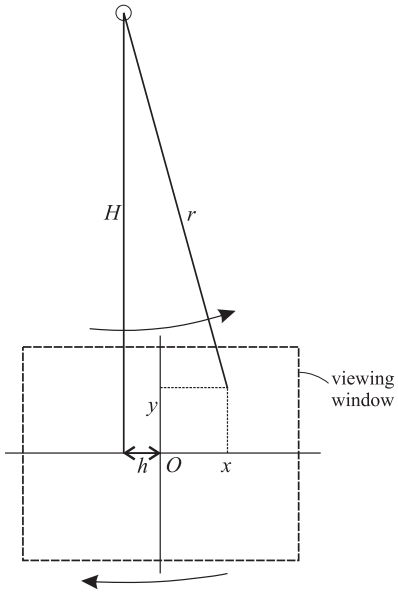

Figure A.2: Definition of variables in case of misalignment in curved Couette flow.

O and r denotes the distance from the rotational axis to this point:

$$r^2 = (h+x)^2 + (H-y)^2 \tag{A.2}$$

Since the geometry is a Couette flow, the rotational velocity ω, shear rate $\dot{\gamma}$ and translational velocity $\mathbf{v} = (v_x, v_y)$ at any point in the window can be written as:

$$\omega(r) = \alpha + \frac{\beta}{r^2} \tag{A.3}$$

$$\dot{\gamma}(r) = r\,\frac{d\omega}{dr} = -\frac{2\,\beta}{r^2} \tag{A.4}$$

$$v_x(x,y) = (\omega \times \mathbf{r})_x = \left(\alpha + \frac{\beta}{r^2}\right)(H-y) \tag{A.5}$$

$$v_y(x,y) = (\omega \times \mathbf{r})_y = \left(\alpha + \frac{\beta}{r^2}\right)(x+h) \tag{A.6}$$

The parameters α and β are related to geometrical parameters like the inner and outer radius, R_i and R_o, and the difference in rotational speed between the cylinders, Ω.

The velocity can be approximated with a Taylor series around the origin:

$$\begin{aligned} v_x(x,y) &= v_{x,o} + \left.\frac{\partial v_x}{\partial x}\right|_o x + \left.\frac{\partial v_x}{\partial y}\right|_o y + \tfrac{1}{2}\left.\frac{\partial^2 v_x}{\partial x^2}\right|_o x^2 + \tfrac{1}{2}\left.\frac{\partial^2 v_x}{\partial y^2}\right|_o y^2 + \left.\frac{\partial^2 v_x}{\partial x\,\partial y}\right|_o xy + \ldots \\ &\approx \frac{v_o H}{r_o} + \frac{\dot\gamma_o h H}{r_o^2}\,x - \left(\frac{v_o}{r_o} + \frac{\dot\gamma_o H^2}{r_o^2}\right) y + \frac{\dot\gamma_o H}{2\,r_o^2}\,(x^2-y^2) + \frac{3\,\dot\gamma_o h}{r_o^2}\,xy \qquad \text{(A.7)} \\ v_y(x,y) &= v_{y,o} + \left.\frac{\partial v_y}{\partial x}\right|_o x + \left.\frac{\partial v_y}{\partial y}\right|_o y + \tfrac{1}{2}\left.\frac{\partial^2 v_y}{\partial x^2}\right|_o x^2 + \tfrac{1}{2}\left.\frac{\partial^2 v_y}{\partial y^2}\right|_o y^2 + \left.\frac{\partial^2 v_y}{\partial x\,\partial y}\right|_o xy + \ldots \\ &\approx \frac{v_o h}{r_o} + \left(\frac{v_o}{r_o} + \frac{\dot\gamma_o h^2}{r_o^2}\right) x - \frac{\dot\gamma_o h H}{r_o^2}\,y + \frac{3\,\dot\gamma_o h}{2\,r_o^2}\,(x^2-y^2) - \frac{\dot\gamma_o H}{r_o^2}\,xy \qquad \text{(A.8)} \end{aligned}$$

where $r_o^2 = H^2 + h^2$, $\dot\gamma_o = -2\,\beta/r_o^2$, $v_o = \alpha\, r_o + \beta/r_o$ and we have made use of the fact that $h/r_o \ll 1$ and $H \approx r_o$. The second term of v_x represents the dominant deviation from planar shear flow. It is the contribution of curvature and misalignment to the particle displacements in the $x-$direction and is responsible for additional broadening of the Gaussian auto-correlation peak. For realistic values of the geometrical parameters the other terms can be neglected. In the $y-$direction no significant effects can be noticed at all.

The preceding equations A.7 and A.8 can be related to experimental data by plotting the correlation data in two different ways. In the first place, a histogram like figure 5.3 shows how the average horizontal displacement $\Delta x_{conv} = \langle v_x \rangle\, \Delta t$ depends on the average vertical position of the particles during the interval (y_{ave}). A similar graph can be made for the vertical peak displacement $\Delta y_{conv} = \langle v_y \rangle\, \Delta t$. These two histograms can be fitted to the equations:

$$\Delta x_{conv} = A_1 \cdot y_{ave} + B_1 \qquad \text{(A.9)}$$

$$\Delta y_{conv} = A_2 \cdot y_{ave} + B_2 \qquad \text{(A.10)}$$

and comparison of the parameters A_1, A_2, B_1 and B_2 with equations A.7 and A.8 can be used to perform the full correction for convective displacements, so that the corrected histogram $\tilde{P}^{exp}(\xi,\eta)$ can be calculated accurately.

In our experiments, we have found misalignment angles θ of typically 0.7° , which is hardly surprising.

References

CAMPBELL, C.S. 1997 Self-diffusion in granular shear flows. *J. Fluid Mech.* **348**, 85–101.

CHANDRASEKHAR, S 1943 Stochastic problems in physics and astronomy. *Rev. Mod. Phys.* **15**, 1–89.

ECKSTEIN, E.C. , BAILEY, D.G. & SHAPIRO, A.H. 1977 Self-diffusion of particles in shear flow of a suspension. *J. Fluid Mech.* **79**, 191–208.

FOSS, D.R. & BRADY, J.F. 1999 Self-diffusion in sheared suspensions by dynamic simulation. *J. Fluid Mech.* **401**, 243–274.

GADALA-MARIA, F. & ACRIVOS, A. 1980 Shear-induced structure in a concentrated suspension of solid spheres. *J. Rheol.* **24** (6), 799–814.

DE HAAS, K.H. , VAN DEN ENDE, D. , BLOM, C. , ALTENA, E.G. , BEUKEMA, G.J. & MELLEMA, J. 1998 A counter-rotating Couette apparatus to study deformation of a sub-millimeter sized particle in shear flow. *Rev. Sci. Instrum.* **69** (3), 1391–1397.

VAN KAMPEN, N.G. 1992 *Stochastic processes in physics and chemistry*. Amsterdam, the Netherlands: Elsevier Science Publishers.

KARNIS, A. , GOLDSMITH, H.L. & MASON, S.G. 1966 The kinetics of flowing dispersions. *J. Colloid Interface Sci.* **22**, 531–553.

LEIGHTON, D. & ACRIVOS, A. 1986 Viscous resuspension. *Chem. Engng Sci.* **41** (6), 1377–1384.

LEIGHTON, D. & ACRIVOS, A. 1987a Measurement of shear-induced self-diffusion in concentrated suspensions of spheres. *J. Fluid Mech.* **177**, 109–131.

LEIGHTON, D. & ACRIVOS, A. 1987b The shear-induced migration of particles in concentrated suspensions. *J. Fluid Mech.* **181**, 415–439.

MARCHIORO, M. & ACRIVOS, A. 2000 Shear-induced particle diffusivities from numerical simulations. *J. Fluid Mech.* **submitted**.

PHAN, S.E. & LEIGHTON, D.T. 1993 Measurement of the shear-induced tracer diffusivity in concentrated suspensions. *J. Fluid Mech.* **submitted**.

PHILLIPS, R.J. , ARMSTRONG, R.C. & BROWN, R.A. 1992 A constitutive equation for concentrated suspensions that accounts for shear-induced particle migration. *Phys. Fluids* **4** (1), 30–40.

PRESS, W.H , FLANNERY, B.P , TEUKOLSKY, S.A. & VETTERLING, W.T. 1986 *Numerical recipees: the art of scientific computing*. Cambridge, England: Cambridge University Press.

ZARRAGA, I.E. , HILL, D.A. & LEIGHTON, D.T. 2000 The characterisation of the total stress of concentrated suspensions of noncolloidal spheres in Newtonian fluids. *J. Rheol.* **44** (2), 185–220.

Chapter 6

Collision Model for Shear-Induced Self-Diffusion

6.1 Introduction

The contents of this thesis is strongly experimentally oriented. A novel technique has been developed and applied to measure various aspects of shear-induced self-diffusion. Our results have contributed to the quantification of shear-induced diffusion, which has improved considerably in recent years for both gradient and self-diffusion. Numerical techniques have made major evolutionary steps as well, so that more reliable data are available (Foss & Brady, 1999; Marchioro & Acrivos, 2000). In spite of the progress, there are still significant discrepancies between experimental and numerical results. As we described in section 1.2.2, where a literature review was presented, the situation is even more challenging at the theoretical front: there have been only a few attempts to model shear-induced diffusion and many aspects of experimental results have not been captured by theoretical predictions yet.

The aim has been to find a physically acceptable model for shear-induced self-diffusion which captures the main characteristics of experimental results (see chapter 2 to 5 and Phan & Leighton (1993)). The most salient features, the combination of which has not been predicted so far by any model, are the scaling of diffusion coefficients with $\dot{\gamma} a^2$, the characteristic diffusive timescale ($\dot{\gamma}\Delta t \sim 1$), the plateau value of the diffusion coefficients with increasing particle volume fraction and the measured anisotropy of the diffusive process.

Here we present a simple collision model, which approaches self-diffusion in a similar way as Leighton & Acrivos (1987) and Phillips *et al.* (1992) treated gradient diffusion. Following the mechanistic concept of these authors, the model is based on the assumption that individual particles move diffusively under the action of excluded volume effects with neighbouring particles on different streamlines in the shear flow. Although the particle motion during each encounter is of deterministic nature, the randomness of the initial conditions can still lead to diffusive displacements, when the effect is averaged over many particles.

The basis of our model is formed by the assumption that 'collisions' between particles can be modelled as effective two-particle processes which proceed unhindered until terminated by the presence of neighbouring particles. As will be shown later on, we are then able to calculate particle trajectories as a function of initial particle positions. Averaging the displacements over all configurations then provides a measure for shear-induced self-diffusion. Although the model is rather crude in the sense that it does not account for the complex hydrodynamics, its simplicity provides interesting insights into the nature of the microscopic processes that could be responsible for shear-induced self-diffusion. In contrast to the model of Phillips *et al.* (1992) for gradient diffusion, which incorporates adjustable parameters for comparison with experimental data, this approach does not have free parameters.

In the next section the model definitions will be explained and the implications of our key assumptions will be discussed. The remaining part of the chapter is then used to calculate and analyze results.

6.2 Model definitions

Within the collision model we use the following definitions for the coordinate system. Consider a simple shear field in which the velocity of the fluid (in Carthesian coordinates) is given by:

$$\mathbf{v} = \dot{\gamma} y \, \mathbf{e}_x \tag{6.1}$$

the $x-$axis being chosen in the velocity direction, the $y-$axis in the gradient and the z-axis in the vorticity direction. The initial orientation of a particle pair on approach is described by the angles θ and φ as illustrated in figure 6.1, where $\mathbf{r}_{12}$ is the end-end vector between the centers of the particles.

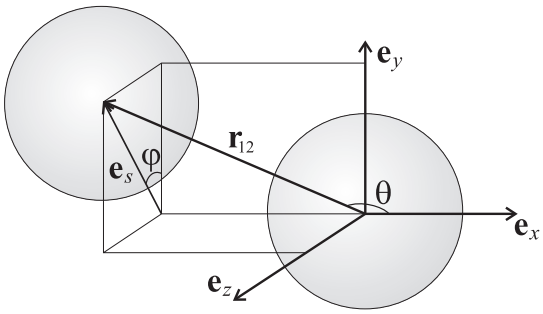

Figure 6.1: The frame of reference and spherical coordinates used.

Using spherical coordinates (r, θ, φ) the following unit vectors can be defined:

$$\begin{aligned} \mathbf{e}_r &= \cos\theta\, \mathbf{e}_x + \sin\theta\, \mathbf{e}_s \\ \mathbf{e}_\theta &= -\sin\theta\, \mathbf{e}_x + \cos\theta\, \mathbf{e}_s \\ \mathbf{e}_\varphi &= -\sin\varphi\, \mathbf{e}_y + \cos\varphi\, \mathbf{e}_z \\ \mathbf{e}_s &= \cos\varphi\, \mathbf{e}_y + \sin\varphi\, \mathbf{e}_z \end{aligned} \tag{6.2}$$

where $\mathbf{e}_s$ is the unit vector that defines the projection of $\mathbf{e}_r$ on the $y-z-$plane. In this framework it can easily be seen that two particles meet at the point where their relative position $\mathbf{r}_{12}$ is given by:

$$\mathbf{r}_{12} = 2\,a\,\mathbf{e}_r \tag{6.3}$$

a being the particle radius.

Now the framework has been set, model assumptions can be made on the evolution of the encounter between two particles. One important issue is how to choose the evolution of relative positions of the particles during this process. In a concentrated suspension the hydrodynamic interactions between particles are extremely complicated. In Stokesian Dynamics calculations, these interactions are taken into account, but the methods is computationally intensive and in order to generate solutions still assumptions must be made. So here we try to find a simplified approach to reduce the complexity of the problem.

For dilute suspensions under shear flow trajectories of particle during collisions have been calculated (e.g. da Cunha & Hinch, 1996). In the case of ideal hard spheres without interaction, the problem is symmetric and no net displacements can be found when the process is completed. When interaction forces are introduced, which could for example represent finite particle roughness, this introduces asymmetries and leads to net displacements. During the trajectory, the largest displacements occur in the velocity gradient direction (y), while only minor deviations in the vorticity direction (z) take place. When many of these interactions take place, the interaction forces thus lead to self-diffusion with a very large anisotropy D_{yy}/D_{zz}.

For concentrated however, experimental results have shown that the motion does not occur in the plane of nearly constant z. In chapter 4 we have presented particle trajectories which demonstrate that the displacements in the vorticity direction are of $O(a)$. Moreover experiments on shear-induced self-diffusion (chapter 3, Phan & Leighton (1993)) also indicate that diffusivity D_{zz} is of the same order of magnitude as D_{yy}. So for modelling the trajectories in concentrated suspensions, the results for dilute suspensions cannot be used.

In our model we propose that particles move affinely when not restricted by excluded volume effects. This means that particles move along the streamlines of macroscopic flow as long as they have not encountered another particle ($|\mathbf{r}_{12}| > 2\,a$):

$$\mathbf{v}_{12} = \mathbf{v}_\infty = \dot{\gamma}\, y\, \mathbf{e}_x \quad \text{for } |\mathbf{r}_{12}| > 2\,a \tag{6.4}$$

At contact only the tangential component is left:

$$\mathbf{v}_{12} = \mathbf{v}_\infty \left(\mathbf{I} - \mathbf{e}_r\,\mathbf{e}_r\right) \quad \text{for } |\mathbf{r}_{12}| = 2\,a \tag{6.5}$$

where y denotes the distance between particle centers in the velocity gradient direction.

A consequence of this assumption is that two particles move relative to each other in the plane of constant angle φ, spanned by the velocity direction $\mathbf{e}_x$ and the unit vector $\mathbf{e}_s(\varphi_0)$ that defines the orientation at first contact. Since particles move affinely until contact, the angle φ_0 is equal to the approach angle. It is clear that this choice implicates significant displacements in the vorticity direction and thus resolves one of the major issues, but how meaningful is this particular choice? The restriction of particles to the plane of constant φ means that only forces in the plane spanned by $\mathbf{e}_r$ and $\mathbf{e}_x$ are taken into account. In the $\mathbf{e}_r-$direction the most important force can be expected to be the excluded volume effect which prevents particles from overlapping and in the velocity direction there is a drag force of the macroscopic shear flow. Thus our model assumption about the particle trajectory is similar to what would be found in Brownian Dynamics simulations without hydrodynamics at high Péclet number. For a simple model such an assumption seems acceptable.

Another important element of modelling the two-particle motion during the encounter is the cut-off criterion. When does a collision end? Here we used the following concept: when two particles rotate around each other, the collision is ended either when the angle $\theta = \pi/2$ is reached –then $\mathbf{v}^0_{rel} \perp \mathbf{e}_r$–, or when a particle experiences a new collision with an incoming third particle. The maximum angle $\theta = \pi/2$ is consistent with the idea that the excluded volume effect dominates, since this effect terminates instantly when the particles enter the extensional region of shear-flow and are pulled apart by the flow. If the concentrations are high, the average time between subsequent collisions is shorter than the time needed to complete the interaction and then the latter criterion is used: collisions are finished when an interaction with new particle occurs.

Under these model assumptions it is possible to determine the particle trajectories and average the resulting displacements over all initial configurations. Thus diffusion coefficients can be extracted as a function of particle volume fraction.

6.3 Collision frequency

Using the definitions in the preceding section, the relative position between two particles (equation 6.3) can be rewritten as

$$\mathbf{r}_{12} = 2\,a\left(\cos\theta\,\mathbf{e}_x + \sin\theta\,\mathbf{e}_s\right) \tag{6.6}$$

The relative velocity between the particles at the start of the collision can now be calculated by means of equation 6.1, noting that the only relevant parameter is the relative position in the $\mathbf{e}_y-$direction:

$$\mathbf{v}_{12} = 2\,\dot{\gamma} a \sin\theta \cos\varphi\, \mathbf{e}_x \tag{6.7}$$

The particle flux onto a tagged particle can then be estimated as:

$$\mathbf{j} = n\,\mathbf{v}_{12} = 2\,n\,\dot{\gamma} a \sin\theta_0 \cos\varphi_0\, \mathbf{e}_x \tag{6.8}$$

where θ_0 and φ_0 define the initial orientation of the colliding particle pair; n represents the number density of particles in the suspension.

The collision rate within a certain space angle $d\dot{N}/d\Omega$ is now given by

$$\frac{d\dot{N}}{d\Omega} = -4\,a^2\,\mathbf{j}\cdot\mathbf{e}_r = -8\,n\,\dot{\gamma}\cos\varphi_0\, a^3 \sin\theta_0 \cos\theta_0 \tag{6.9}$$

and using $n = 3\phi/4\pi a^3$ the total collision rate per particle is then equal to

$$\begin{aligned} \dot{N} &= 2\int_{\Omega'} \frac{d\dot{N}}{d\Omega} d\Omega \\ &= -\frac{12}{\pi}\phi\,\dot{\gamma}\int_{\pi/2}^{\pi} \sin^2\theta_0 \cos\theta_0\, d\theta_0 \int_{-\pi/2}^{\pi/2} \cos\varphi_0\, d\varphi_0 \\ &= \frac{8}{\pi}\phi\,\dot{\gamma} \end{aligned} \tag{6.10}$$

where the integral is taken over the space angle Ω' bounded by $\pi/2 < \theta < \pi$ and $-\pi/2 < \varphi < \pi/2$, one of the compressive zones of the shear flow ($x < 0$, $y > 0$). The factor 2 in equation 6.10 is needed to account for collisions in the other compressive region ($x > 0$, $y < 0$), symmetrical relative to the center of the tagged particle.

Consequently, the probability that a given collision occurs with orientation θ_0, φ_0 is given by the function $\Phi(\theta_0, \varphi_0)$:

$$\Phi(\theta_0, \varphi_0) = \frac{(d\dot{N}/d\Omega)}{\int_{\Omega'}(d\dot{N}/d\Omega)\,d\Omega} = -\frac{3}{2}\cos\varphi_0 \cos\theta_0 \sin\theta_0; \tag{6.11}$$

where the probability has been normalized over only one compressional quadrant, since our calculations in the remainder of this chapter will be carried out on this basis as well, so that the factor 2 as applied in equation 6.10 can left out.

The mean time between two collisions, τ, follows directly from equation 6.10:

$$\tau = \frac{1}{\dot{N}} = \frac{\pi}{8\,\phi\,\dot{\gamma}} \tag{6.12}$$

6.4 Particle trajectory

To obtain the particle displacement during a collision we describe the motion with respect to the center of mass of the two colliding particles. The initial position of the incoming particle relative to the center of mass is then given by (equation 6.6)

$$\mathbf{r}_1 = a\,(\cos\theta_0\ \mathbf{e}_x + \sin\theta_0\ \mathbf{e}_s(\varphi)) \tag{6.13}$$

Applying equation 6.5 the following expression can now be derived for the velocity during the collision phase:

$$\begin{aligned} \mathbf{v} &= \mathbf{v}_\infty \cdot (\mathbf{I} - \mathbf{e}_r\mathbf{e}_r) \\ &= a\,\dot\gamma \cos\varphi_0\ \sin^2\theta(\sin\theta\ \mathbf{e}_x - \cos\theta\ \mathbf{e}_s) \end{aligned} \tag{6.14}$$

while the undisturbed velocity without interaction would have been given by:

$$\mathbf{v}_\infty = a\,\dot\gamma \cos\varphi_0\ \sin\theta\ \mathbf{e}_x \tag{6.15}$$

With reference to section 6.2 we then introduce the angle θ_1 that is defined in such a way that the average time between subsequent collisions equals the average duration of the collisions. Each collision then continues while $\theta_0 \geq \theta \geq \theta_1$. The cut-off angle θ_1 can be estimated from the influx of particles and depends on the particle volume fraction ϕ. The angular speed $\dot\theta$ is given by $\dot\theta = -\dot\gamma \cos\varphi_0\ \sin^2\theta$, so the duration of a collision is given by

$$\Delta t = \frac{-1}{\dot\gamma\cos\varphi_0}\int_{\theta_0}^{\theta_1}\frac{d\theta}{\sin^2\theta} = \frac{1}{\dot\gamma\cos\varphi_0}(\cot\theta_1 - \cot\theta_0) \tag{6.16}$$

We obtain a value for θ_1 from the following consideration: if all collisions would stop at a fixed value for θ_1, the average value of Δt can be calculated:

$$\langle\Delta t\rangle = \int_{-\pi/2}^{\pi/2}\int_{\pi/2}^{\pi}\Delta t\ \Phi(\theta_0,\varphi_0)\ \sin\theta_0\ d\theta_0\,d\varphi_0 = \frac{\pi}{2\dot\gamma}(1+\cot\theta_1) \tag{6.17}$$

This time $\langle\Delta t\rangle$ must be smaller than or equal to τ, i.e.

$$\cot\theta_1 = \begin{cases} \frac{1}{4\phi} - 1 & \text{for } \phi > \frac{1}{4} \\ 0 & \text{for } \phi \leq \frac{1}{4} \end{cases} \tag{6.18}$$

The displacement **s** can be obtained by integration of the velocity (eq. 6.14) minus the undisturbed velocity (eq. 6.15) at that position:

$$\begin{aligned} \mathbf{s} &= \int_0^{\Delta t}(\mathbf{v}-\mathbf{v}_\infty)\,dt = -\int_0^{\Delta t}\mathbf{v}_\infty\cdot\mathbf{e}_r\mathbf{e}_r\,dt \\ &= a\int_{\theta_0}^{\theta_1}\left[\sin\theta\ \cos^2\theta\ \mathbf{e}_x + \sin^2\theta\ \cos\theta\ \mathbf{e}_s\right]\ \frac{d\theta}{\sin^2\theta} \\ &= a\ (\sin\theta_1 - \sin\theta_0)\ \mathbf{e}_s + a\ (\mathrm{f}(\theta_1) - \mathrm{f}(\theta_0))\ \mathbf{e}_x \end{aligned} \tag{6.19}$$

with

$$f(\theta) = \cos\theta + \tfrac{1}{2}\ln\left(\frac{1-\cos\theta}{1+\cos\theta}\right) \tag{6.20}$$

6.5 The diffusion tensor

The relevant components of the diffusion tensor **D** can be calculated by means of the following equations:

$$\begin{aligned} D_{xx} &= \frac{\langle s_x\, s_x\rangle}{2\,\tau} = \frac{4}{\pi}\phi\,\dot{\gamma}\,a^2\langle\tilde{s}_x\,\tilde{s}_x\rangle \\ D_{yy} &= \frac{\langle s_y\, s_y\rangle}{2\,\tau} = \frac{4}{\pi}\phi\,\dot{\gamma}\,a^2\langle\tilde{s}_y\,\tilde{s}_y\rangle \\ D_{zz} &= \frac{\langle s_z\, s_z\rangle}{2\,\tau} = \frac{4}{\pi}\phi\,\dot{\gamma}\,a^2\langle\tilde{s}_z\,\tilde{s}_z\rangle \\ D_{xy} &= \frac{\langle s_x\, s_y\rangle}{2\,\tau} = \frac{4}{\pi}\phi\,\dot{\gamma}\,a^2\langle\tilde{s}_x\,\tilde{s}_y\rangle \end{aligned} \tag{6.21}$$

where $\tilde{\mathbf{s}} = \mathbf{s}/a$ is scaled on the particle radius. The averaging over the particle steps must be performed using Φ (eq. 6.11) as weight function:

$$\langle\cdot\rangle = \int_{-\pi/2}^{\pi/2}\int_{\pi/2}^{\pi}(\cdot)\;\Phi(\theta_0,\varphi_0)\;\sin\theta_0\;d\theta_0\;d\varphi_0 \tag{6.22}$$

The dyad $\langle\tilde{\mathbf{s}}\,\tilde{\mathbf{s}}\rangle$ can be split into its components along the $\mathbf{e}_s$ and $\mathbf{e}_x$ axes in the following way:

$$\begin{aligned} \tilde{\mathbf{s}}\,\tilde{\mathbf{s}} &= (\sin\theta_1 - \sin\theta_0)^2\,\mathbf{e}_s\mathbf{e}_s + (f(\theta_1) - f(\theta_0))^2\,\mathbf{e}_x\mathbf{e}_x + \\ &\quad (\sin\theta_1 - \sin\theta_0)\,(f(\theta_1) - f(\theta_0))\,(\mathbf{e}_x\mathbf{e}_s + \mathbf{e}_s\mathbf{e}_x) \end{aligned} \tag{6.23}$$

Since the unit dyads $\mathbf{e}_s\,\mathbf{e}_s$ and $\mathbf{e}_x\,\mathbf{e}_s$ depend on $\varphi = \varphi_0$ and the coefficients are only functions of θ_0, the averaging integrals over θ_0 and φ can be separated, leading to:

$$\begin{aligned} \langle\tilde{\mathbf{s}}\,\tilde{\mathbf{s}}\rangle &= \langle(\sin\theta_1 - \sin\theta_0)^2\rangle_{\theta_0}\,\langle\mathbf{e}_s\mathbf{e}_s\rangle_\varphi + \langle(f(\theta_1) - f(\theta_0))^2\rangle_{\theta_0}\,\mathbf{e}_x\mathbf{e}_x \\ &\quad + \langle(\sin\theta_1 - \sin\theta_0)\;(f(\theta_1) - f(\theta_0))\rangle_{\theta_0}\left(\langle\mathbf{e}_x\mathbf{e}_s\rangle_\varphi + \langle\mathbf{e}_s\mathbf{e}_x\rangle_\varphi\right) \\ &= \left[\sin^2\theta_1\;\langle 1\rangle_{\theta_0} + \langle\sin^2\theta_0\rangle_{\theta_0} - 2\sin\theta_1\;\langle\sin\theta_0\rangle_{\theta_0}\right]\langle\mathbf{e}_s\mathbf{e}_s\rangle_\varphi \\ &\quad + \left[f^2(\theta_1)\;\langle 1\rangle_{\theta_0} + \langle f^2(\theta_0)\rangle_{\theta_0} - 2\,f(\theta_1)\,\langle f(\theta_0)\rangle_{\theta_0}\right]\,\mathbf{e}_x\mathbf{e}_x \\ &\quad + [\sin\theta_1\,f(\theta_1)\;\langle 1\rangle_{\theta_0} + \langle\sin\theta_0\,f(\theta_0)\rangle_{\theta_0} - \sin\theta_1\;\langle f(\theta_0)\rangle_{\theta_0} - \langle\sin\theta_0\rangle_{\theta_0}\,f(\theta_1)]\times \\ &\quad \left(\langle\mathbf{e}_x\mathbf{e}_s\rangle_\varphi + \langle\mathbf{e}_s\mathbf{e}_x\rangle_\varphi\right) \end{aligned} \tag{6.24}$$

The $\varphi-$averages over the unit dyads can now be calculated by expressing $\mathbf{e}_s$ in Carthesian coordinates:

$$\begin{aligned}
\langle \mathbf{e}_s \mathbf{e}_s \rangle_\varphi &= \tfrac{1}{2} \int_{-\pi/2}^{\pi/2} (\cos\varphi\, \mathbf{e}_y + \sin\varphi\, \mathbf{e}_z)(\cos\varphi\, \mathbf{e}_y + \sin\varphi\, \mathbf{e}_z)\, \cos\varphi\, d\varphi \\
&= \tfrac{2}{3}\, \mathbf{e}_y \mathbf{e}_y + \tfrac{1}{3}\, \mathbf{e}_z \mathbf{e}_z \\
\langle \mathbf{e}_x \mathbf{e}_s \rangle_\varphi &= \langle \mathbf{e}_s \mathbf{e}_x \rangle_\varphi = \tfrac{1}{2} \int_{-\pi/2}^{\pi/2} \mathbf{e}_x\, (\cos\varphi\, \mathbf{e}_y + \sin\varphi\, \mathbf{e}_z)\, \cos\varphi\, d\varphi \\
&= \tfrac{\pi}{4}\, \mathbf{e}_x \mathbf{e}_y
\end{aligned} \tag{6.25}$$

and the θ_0-averaging of the remaining terms results in:

$$\begin{aligned}
\langle \sin\theta_0 \rangle_{\theta_0} &= 0.750000 \\
\langle \sin^2\theta_0 \rangle_{\theta_0} &= 0.600000 \\
\langle \mathrm{f}(\theta_0) \rangle_{\theta_0} &= 0.196350 \\
\langle \mathrm{f}^2(\theta_0) \rangle_{\theta_0} &= 0.107983 \\
\langle \sin\theta_0\, \mathrm{f}(\theta_0) \rangle_{\theta_0} &= 0.100000
\end{aligned} \tag{6.26}$$

Combining these results the components of $\langle \mathbf{s}\, \mathbf{s} \rangle$ in the Carthesian coordinate system finally become:

$$\begin{aligned}
\langle \tilde{s}_x \tilde{s}_x \rangle &= 0.107983 + \mathrm{f}^2(\theta_1) - 0.392700\, \mathrm{f}(\theta_1) \\
\langle \tilde{s}_y \tilde{s}_y \rangle &= 0.4 + \tfrac{2}{3} \sin^2\theta_1 - 1.0\, \sin\theta_1 \\
\langle \tilde{s}_z \tilde{s}_z \rangle &= 0.2 + \tfrac{1}{3} \sin^2\theta_1 - 0.50\, \sin\theta_1 \\
\langle \tilde{s}_x \tilde{s}_y \rangle &= \tfrac{\pi}{4} (0.1 - 0.75\, \mathrm{f}(\theta_1) + \sin\theta_1\, \mathrm{f}(\theta_1) - 0.196350\, \sin\theta_1) \\
\langle \tilde{s}_y \tilde{s}_x \rangle &= \tfrac{\pi}{4} (0.1 - 0.75\, \mathrm{f}(\theta_1) + \sin\theta_1\, \mathrm{f}(\theta_1) - 0.196350\, \sin\theta_1)
\end{aligned} \tag{6.27}$$

where $\theta_1 = \frac{\pi}{2}$ if $\phi \leq 0.25$ and $\theta_1 = \pi + \arctan\left(\frac{4\phi}{1-4\phi}\right)$ if $\phi > 0.25$.

Equations 6.21 and 6.27 reveal a number of characteristic results. In the first place it should be noticed that the collision model correctly predicts the scaling of shear-induced self-diffusion with $\dot{\gamma} a^2$. Although this might not be very surprising regarding the ease with which the scaling effects can be predicted (see 5.2.1), any model of physical relevance should be in agreement with this fundamental property.

Secondly, the anisotropy D_{yy}/D_{zz} between the velocity gradient and vorticity direction is equal to 2 in our model. This is directly the result of our model assumption that particle pairs move within the plane of constant angle φ during their encounter. Averaging over all possible initial angles θ_0 and φ_0 leads to the geometrically determined anisotropy of 2.

Using equation 6.21 all the relevant components of the diffusion tensor have been calculated and plotted in fig. 6.2 in dimensionless form.

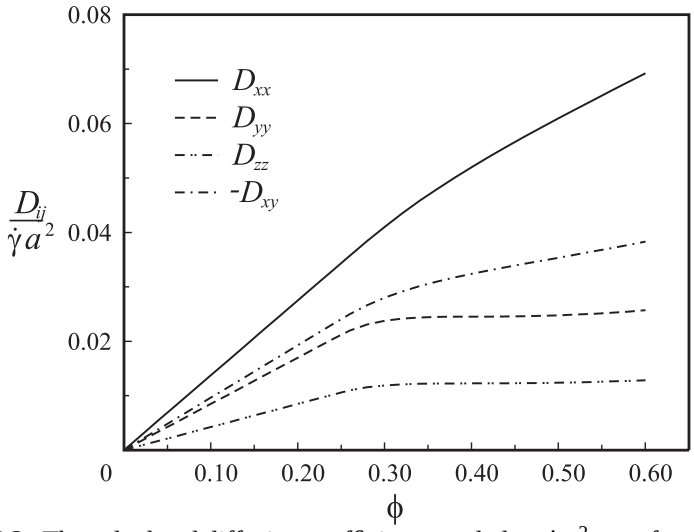

Figure 6.2: The calculated diffusion coefficients, scaled on $\dot{\gamma} a^2$, as a function of ϕ.

6.6 Discussion

Considering its simplicity, the results of the simple collision model are quite interesting when compared to numerical and experimental observations.

Quantitatively the collision model predicts diffusion coefficients that are of the proper order of magnitude. For D_{yy} and D_{zz} the values are almost a factor 4 lower than experimental data. However, most numerical data that have been calculated with Stokesian Dynamics techniques are lower than experimental results as well, roughly by a factor 2. Only the recent data of Marchioro & Acrivos (2000), who extrapolate their results to infinite system size, approach the experimental values. For a simple model without adjustable parameters, the quantitative agreement is remarkable.

Another remarkable feature is the volume fraction dependence. For volume fractions above 25% the curves level off significantly, in particular D_{yy} and D_{zz}. In terms of our model it is the result of the fact that above this critical concentration the average duration of an interaction is shorter than the time that is needed to complete the trajectory to $\theta = \pi/2$. Therefore an increase in collision frequency automatically leads to smaller displacement steps. The two effects apparently cancel out in the $y-$ and $z-$direction, while the diffusion in the velocity direction and thus the coupling term D_{xy} remain ascending functions of the particle volume fraction ϕ. This behaviour differ from theoretical scaling predictions of Brady & Morris (1997), who predict the step size to remains of $O(a)$ even at high concentrations, so that diffusion grows when the frequency of interaction becomes higher. Experiments have shown a plateau at high volume fractions (see chapter 2 and 3). Although the transition in experiments occurs at a somewhat higher volume fraction, around $\phi = 0.35$, the effect

is noteworthy.

As noted in the preceding section, the observed anisotropy is purely geometrical and a result of the model assumption that particles move in the plane spanned by the velocity direction and their initial separation vector. The assumption seems reasonable if central forces are dominating the particle collision, which would be the case if excluded volume effects play an important role. Thus we can account for the experimentally observed ratio $D_{yy}/D_{zz} \approx 2$.

Although the collision model correctly predicts the negative sign of D_{xy}, there seem to be important discrepancies with our experimental results as reported in chapter 5 for the diffusion components D_{xx} and D_{xy}, in particular considering the volume fraction dependence of these parameters. It must be noted however that our experimental results are the first attempts to measure these diffusive quantities. The adequacy of the collision model can hardly be assessed on the basis of those results, but the issue definitely deserves attention.

All in all the collision model described in this chapter, shows that characteristic features of shear-induced self-diffusion can be captured by means of a simple mechanistic picture. Key elements have been the assumptions of effective two-particle encounters, the direction of particle trajectories during the interaction phase and the cessation of collisions due to the influx of third particles.

References

BRADY, J.F. & MORRIS, J.F. 1997 Microstructure of strongly sheared suspensions and its impact on rheology and diffusion. *J. Fluid Mech.* **348**, 103–139.

DA CUNHA, F.R. & HINCH, E.J. 1996 Shear-induced dispersion in a dilute suspension of rough spheres. *J. Fluid Mech.* **309**, 211–223.

FOSS, D.R. & BRADY, J.F. 1999 Self-diffusion in sheared suspensions by dynamic simulation. *J. Fluid Mech.* **401**, 243–274.

LEIGHTON, D. & ACRIVOS, A. 1987 The shear-induced migration of particles in concentrated suspensions. *J. Fluid Mech.* **181**, 415–439.

MARCHIORO, M. & ACRIVOS, A. 2000 Shear-induced particle diffusivities from numerical simulations. *J. Fluid Mech.* **submitted**.

PHAN, S.E. & LEIGHTON, D.T. 1993 Measurement of the shear-induced tracer diffusivity in concentrated suspensions. *J. Fluid Mech.* **submitted**.

PHILLIPS, R.J. , ARMSTRONG, R.C. & BROWN, R.A. 1992 A constitutive equation for concentrated suspensions that accounts for shear-induced particle migration. *Phys. Fluids* **4** (1), 30–40.

Summary

Suspensions consist of solid particles dispersed in a liquid. In practice they are for example used for large-scale transport of particulate materials like sand. During oil and gas drilling suspensions are utilized for the transport of rock cuttings. Furthermore they can be found in industry in the production of foods, paint and paper. Knowledge of the flow properties of suspensions is therefore of practical interest and forms an important research area in rheology.

This thesis contains the results of an experimental investigation of 'shear-induced diffusion'. It is by now well-known that individual particles in concentrated suspensions of non-colloidal particles ($> 10\ \mu$m) exhibit a fluctuating motion under influence of an externally applied flow field. The process can be characterized as diffusion and is caused by the fact that particles on neighbouring streamlines are forced to pass each other. The interactions are asymmetrical and lead to particle displacements.

In geometries with an inhomogeneous shear rate or in case of inhomogeneities in the particle distribution, the process leads to transport of particles, referred to as gradient diffusion. In pipe flow, for example, particles migrate towards the center of the pipe. In practice this is a potential source of trouble, since it can influence mixing and heat transfer. In homogeneous systems migration is absent, but individual particles still display diffusive motion, the so-called self-diffusion. In understanding the flow properties of suspensions, shear-induced self-diffusion is therefore an important physical quantity.

A novel method has been developed to measure shear-induced self-diffusion in concentrated suspensions of non-colloidal hard spheres. The technique is based on optical tracing. In order to have optical access to a concentrated suspension, the suspending liquid was refractive index matched with the spheres. To this transparent suspension a small fraction of coloured particles was added. These tracers are visible with a CCD camera. The camera is used to collect images of a flowing suspension. The images are then subjected to image analysis to determine the positions of tracer particles in every image. The tracer positions in subsequent images are compared. By collecting information for a large number of image combinations, which have been obtained under identical circumstances, a statistical analysis can be made of the particle motion. The nature of the motion can be investigated through the evolution of displacement statistics and in case of diffusion the diffusion coefficient can be determined.

The most powerful advantage of the technique over existing methods is the pos-

sibility to study particle motion over a time interval (the relevant dimensionless time being the strain, the product of shear rate and time). Thus the nature of the particle motion can be checked before diffusion coefficients are extracted. In addition, the transition from non-diffusive to diffusive motion can be examined in detail.

The first part of the thesis describes the development of the experimental technique and the application to concentrated hard sphere suspensions with particle volume fractions ranging from 20 to 50%. The first measurements on diffusion in the velocity gradient and vorticity direction were carried out in a set-up with non-ideal flow conditions. For large time steps too many particles left the observation window of the camera to obtain reliable statistical information. In chapter 3 this problem has been solved by using an advanced 'counter-rotating' geometry. In this apparatus particles were kept within view much longer and diffusion and measurements could be performed over a sufficiently large range of time to accurately determine diffusion coefficients. The results were in good agreement with literature data which have been obtained by means of other methods.

The second part reports on more detailed analysis of the data. In chapter 4 different approaches are presented to investigate the motion of particles in concentrated suspensions: the paths of individual tracer particles, the self-diffusion as measured with the newly developed statistical method and rheological measurements, which show the macroscopical relation between stress and deformation. Both diffusion and rheology are the result of the underlying microstructure and must therefore be correlated.

It is demonstrated in chapter 5 how the results of the diffusion measurements can be utilized to obtain values for all components of the diffusion tensor. In addition to the diffusion coefficients in the velocity gradient and vorticity directions, the two remaining components can be determined: the diffusion in the velocity direction and the off-diagonal component. The off-diagonal component contains the coupling between motion in the velocity and velocity gradient direction. The first known experimental values for these quantities are presented.

Finally, chapter 6 contains a simple collision model. The dynamics of concentrated suspensions are quite complicated and a full solution of the problem is virtually impossible. The collision model, which is essentially based on two-particle interactions, has been developed to investigate if simple mechanical concepts can be used to model shear-induced self-diffusion. The model is based on some simple assumptions that are directly related to characteristic behaviour which was also observed in our experiments.

Samenvatting

Vaste deeltjes gedispergeerd in een vloeistof vormen een suspensie. In de praktijk worden suspensies bijvoorbeeld toegepast voor grootschalig transport van materialen als zand. Tijdens het boren naar olie en gas worden ze gebruikt om boorgruis af te voeren. Bovendien komt men suspensies in de industrie tegen bij de produktie van bijv. voedingsmiddelen, verf en papier. Kennis van de stromingseigenschappen van suspensies is daarom van praktisch belang en vormt een belangrijk aandachtsgebied binnen de reologie.

Dit proefschrift beschrijft de resultaten van een experimenteel onderzoek naar 'hydrodynamische diffusie'. Het is bekend dat in geconcentreerde suspensies van niet-colloïdale deeltjes ($> 10\ \mu$m) onder invloed van een opgelegd stromingsveld de individuele deeltjes een chaotisch bewegingspatroon vertonen dat gekarakteriseerd kan worden als diffusie. Deze diffusie wordt veroorzaakt doordat deeltjes op verschillende stroomlijnen elkaar willen passeren. In een geconcentreerd systeem zijn deze interacties niet-symmetrisch, zodat de deeltjes een verplaatsing ondervinden.

In een stromingsgeometrie met een inhomogene afschuifsnelheid of in geval van inhomogeniteiten in deeltjesconcentratie kan dit diffusieproces leiden tot een transport van deeltjes, ook wel gradiënt diffusie genoemd. In een pijpstroming zullen de deeltjes bijvoorbeeld naar het centrum van de pijp migreren. Als er geen rekening mee wordt gehouden kan dit in de praktijk voor problemen zorgen. In een homogeen systeem treedt het transport niet op, maar individuele deeltjes vertonen nog altijd een diffusief bewegingspatroon, de zogenaamde zelf-diffusie. Om de eigenschappen van suspensies te kunnen begrijpen is zelf-diffusie dus een belangrijke fysische grootheid.

Er is een nieuwe methode ontwikkeld om hydrodynamische zelf-diffusie te meten in geconcentreerde suspensies van niet-colloidale harde bollen. De techniek is gebaseerd op optische waarneming. Om in een geconcentreerde suspensie optisch iets te kunnen onderscheiden is de vloeistof zo gekozen dat de brekingsindex gelijk is aan die van de deeltjes. De suspensie is dan transparant. Een kleine fractie van de bollen is vervolgens gekleurd en deze deeltjes zijn zichtbaar. Met behulp van een videocamera worden opnamen gemaakt van de suspensie in een stroming. Op deze beelden wordt vervolgens beeldanalyse toegepast om in elk videobeeldje de posities van de gekleurde deeltjes te bepalen. De posities van deeltjes in opeenvolgende videobeelden worden vergeleken. Door informatie te verzamelen voor een groot aantal combinaties van beeldjes, die onder identieke omstandigheden zijn verzameld, wordt de basis gelegd voor statistische analyse van de deeltjesbeweging. Als het

statistisch gedrag zich op een zekere manier ontwikkelt is sprake van diffusie en wordt de diffusiecoëfficiënt bepaald.

Het belangrijkste voordeel van de methode boven reeds bestaande technieken is de mogelijkheid om de deeltjesbeweging te bestuderen over een tijdsinterval (de relevante dimensieloze tijd is eigenlijk de *vervorming*, het produkt van tijd en afschuifsnelheid). Op deze manier kan beter worden gecontroleerd of inderdaad sprake is van een diffusief proces, alvorens de diffusiecoëfficiënt te bepalen. Tevens kan zo het overgangsgebied van niet-diffusief naar diffusief gedrag worden onderzocht.

Het eerste deel van dit proefschrift beschrijft de ontwikkeling van de nieuwe meetmethode en de toepassing voor geconcentreerde suspensies van harde bollen met een deeltjesconcentratie tussen de 20 en 50%. De eerste metingen met deze techniek voor diffusie in de snelheidsgradiënt- en vorticiteitsrichting (hoofdstuk 2) zijn uitgevoerd in een experimentele opstelling, waarin het stromingsveld niet optimaal was. Naarmate de tijdstappen tussen beelden groot werden, stroomden teveel deeltjes uit het blikveld van de videocamera om voldoende informatie over te houden voor betrouwbare statistiek. In hoofdstuk 3 is dit ondervangen door een geavanceerde ”counter-rotating” geometrie te gebruiken. Hierdoor blijven deeltjes langer in beeld en onder deze omstandigheden konden metingen worden verricht over een voldoende groot bereik om nauwkeurig diffusie te meten. De resultaten bleken goed overeen te komen met data in de literatuur, die langs andere weg zijn verkregen.

Het tweede deel bevat een nadere analyse van de meetresultaten. In hoofdstuk 4 wordt op verschillende wijzen gekeken naar de beweging van deeltjes in geconcentreerde suspensies: de beweging van individuele deeltjes, diffusiecoëfficiënt zoals bepaald via bovenstaande statistische methode en reologische experimenten, die de macroscopische relatie tussen krachten en vervormingen weergeven. Zowel diffusie als reologie zijn het gevolg van de onderliggende microstructuur en moeten daarom gecorreleerd zijn.

In hoofdstuk 5 wordt getoond hoe de resultaten gebruikt kunnen worden om alle componenten van de diffusietensor te bepalen. Door uitbreiding van de analyse kan met onze meettechniek naast de al eerder bepaalde diffusiecoëfficiënten tevens de component in de snelheidsrichting worden gemeten. De kruisterm bevat de koppeling tussen beweging in de snelheidsgradient- en snelheidsrichting. De hier beschreven metingen zijn de eerste experimentele bepalingen van deze diffusiecoëfficiënten.

Hoofdstuk 6 bevat een eenvoudig botsingsmodel. De dynamica van geconcentreerde suspensies is zeer ingewikkeld en een volledige oplossing van het probleem is nagenoeg onmogelijk. Het botsingsmodel is ontwikkeld om te onderzoeken of op basis van eenvoudige mechanische concepten de hydrodynamische zelf-diffusie kan worden gemodelleerd. Het model is gebaseerd op enkele eenvoudige aannames. Deze aannames zijn rechtstreeks gerelateerd aan karakteristiek gedrag dat ook in onze experimenten wordt gevonden.

Acknowledgements

This thesis marks the completion of my PhD-project and although I have been at the centre of the process, many people have made valuable contributions.

First of all, I want to thank the foundation for Fundamental Research on Matter (FOM) and my promotor Jorrit Mellema for the opportunity to work on 'shear-induced diffusion'. I have never regretted taking this challenge. Jorrit has also offered me the chances to experience the international nature of science and build contacts with other researchers in the field.

My advisors Dirk van den Ende and Rob Jongschaap have played a prominent role. Thanks to Dirk's talent to thoroughly analyze experimental results and Rob's fundamental questions, we have accomplished the results presented in this thesis. I have learnt a lot from them that will be most valuable in my future career as a scientist. During the final months of my PhD project, Maarten Bosscher has made an important contribution as an undergraduate student. Without his dedication we would never have reached the point were we are today, although it required the sacrifice of many evenings and weekends for the benefit of science.

The success of any experimentally oriented project strongly depends on the quality of practical support. I am grateful to Egbert Altena, Gerrit Beukema and Jacob Lopulissa for their indispensable assistance in the realization of my experimental set-up. In the final months a few unexpected problems threatened the progress of the project. Fortunately, these could be solved with the professional skills of Klaas Smit and Michael Foley.

Furthermore I gratefully acknowledge the hospitality of professor Acrivos at the Levich Institute of the City College in New York. The discussions during my three months working visit to his lab were most inspiring and have strongly propelled my experimental work. The daily cooperation with Anubhav Tripathi was both pleasant and extremely fruitful. I enjoyed it a lot and often remember those days!

Within the Rheology Group I have had a great time. In particular I want to express my appreciation to Berend-Jan, Roland and Paul. As colleagues and office mates we have shared the good and bad times of PhD research. In cooperation with Paul many computer problems have been mastered: the lay-out of this thesis is an

excellent example. Outside the group, I want to thank Maarten Biesheuvel. Together we have carried out many simple experiments which revealed the beauty of nature. His enthusiasm is highly infectious and has led to a number of joint papers.

It was not all about science these last years. With my friends from Euros I have enjoyed many pleasant weekends on the water. And there were, of course, the weekly meetings of the movie club: Susan, Marieke, Joris, Laïla, Michiel, Henno en Linda, thanks for all the culinary highlights and relaxing evenings. Henno deserves extra credits for the lunch runs we completed together: the social discipline was very healthy and contributed to my mental an physical shape.

Finally I want to express my gratitude towards my parents, Itske and Fulco: their lifelong support has been the fundament for this thesis.

Victor Breedveld Enschede, September 2000.

Curriculum vitae

Victor Breedveld was born on April 15 1973 in Domburg (Netherlands). In May 1991 he completed his pre-university education by qualifying for his gymnasium diploma at the Willem Lodewijk Gymnasium in Groningen. He started his academic career by studying Applied Physics at the University of Twente. As part of the course he fulfilled a practical assignment with Schlumberger Cambridge Research, where he first encountered the phenomenon of 'shear-induced diffusion' which a couple of years later would serve as the starting point of this PhD thesis. The final project of his MSc was carried out in the Rheology Group of prof.dr. J. Mellema and concerned an experimental investigation of the rheological properties of weakly aggregated colloidal suspensions.

After obtaining his MSc he decided to stay at the Rheology Group as a PhD-student in order to investigate the already mentioned 'shear-induced diffusion', the diffusion-like motion of non-colloidal particles in concentrated suspensions driven by an externally applied flow field. The most important result of the project has been the development of a novel experimental method to characterize the diffusion process.

He has continued his research career as a postdoctoral researcher in the group of professor Pine at the University of California at Santa Barbara.